FACULTY
OF MATHEMATICS
AND PHYSICS
Charles University

DOCTORAL THESIS

Bedřich Roskovec

Detailed Investigation of Electron Antineutrino Oscillations in the Daya Bay Experiment

Institute of Particle and Nuclear Physics

Supervisor of the doctoral thesis:	Prof. RNDr. Rupert Leitner, DrSc.
Study programme:	Physics
Study branch:	Subnuclear Physics

Prague 2016

I declare that I carried out this doctoral thesis independently, and only with the cited sources, literature and other professional sources.

I understand that my work relates to the rights and obligations under the Act No. 121/2000 Sb., the Copyright Act, as amended, in particular the fact that the Charles University has the right to conclude a license agreement on the use of this work as a school work pursuant to Section 60 subsection 1 of the Copyright Act.

In .... date .... signature of the author

Title: Detailed Investigation of Electron Antineutrino Oscillations in the Daya Bay Experiment

Author: Bedřich Roskovec

Institute: Institute of Particle and Nuclear Physics

Supervisor: Prof. RNDr. Rupert Leitner, DrSc., Institute of Particle and Nuclear Physics

Abstract: Observed disappearance of reactor antineutrinos in the short baseline in Daya Bay can be explained by the phenomenon of neutrino flavour oscillations. The analysis in standard three-neutrino framework provide the best measurement of mixing angle of θ_{13} and the value of effective mass squared difference Δm^2_{ee} with comparable precision with other experiments. The unprecedented precision of Daya Bay motivates us to extend our search beyond standard three-neutrino oscillation scheme. It this thesis, we have explored two scenarios of possible physics Beyond Standard Model (BSM).

We have tested the fundamental symmetry of the nature by searching for the Lorentz Invariance violation effect within the framework of the Standard-Model Extension (SME). Such an effect could be observed as a deviation from three-neutrino oscillation prediction in the oscillated antineutrino spectrum. Since we have not observed any significant deviation, we have been able to set the limits on the SME parameters. Some of the limits were measured for the first time while some turned out not to be competitive with the measurement of other experiments.

We have also performed search for Non-standard Interactions (NSIs) in the Daya Bay. Being forbidden in the Standard Model, these interactions are predicted by BSM theories for which Standard Model is considered to be a low energy limit. Such NSIs effects could take place in the process of production and detection of the reactor antineutrinos and effectively modify the oscillation probability. In order to perform this analysis we have developed our own phenomenological approach to include the NSIs effect in the neutrino oscillations. No significant deviation from standard three-neutrino framework oscillation was found. We obtained limits on the NSIs parameter.

Keywords: Daya Bay, Reactor Antineutrinos, Neutrino Oscillations, Lorentz Invariance, Non-standard Interactions

Contents

1 Introduction 5

2 Neutrino Oscillations 9

2.1 Neutrino Properties 9

2.1.1 History of Neutrino 9

2.1.2 Neutrinos in the Standard Model 10

2.2 Neutrino Flavour Oscillations - Compelling Evidence for Neutrino Mass 10

2.2.1 Neutrino Mixing in Three-neutrino Framework 11

2.2.2 Neutrino Oscillation Probability in Vacuum 12

2.2.3 Relation between Neutrino and Antineutrino Oscillation Probability 13

2.3 Brief History of the Measurement of the Oscillation Parameters . 13

2.3.1 Solar Neutrinos 14

2.3.2 Atmospheric Neutrinos 15

2.3.3 Accelerator Neutrinos and CP-violation in Lepton Sector . 16

2.3.4 Reactor Antineutrino Measurement 17

2.3.5 Entering the Era of Precision Measurement of Oscillation Parameters 18

2.3.6 Road to Mixing Angle θ_{13} 18

2.3.7 Neutrino Flavour Oscillation Parameter Values and Open Questions in Neutrino Oscillations 19

2.3.8 Other Questions in Neutrino Physics 21

3 Test of the Lorentz Invariance in the Antineutrino Oscillations in Daya Bay 23

3.1 Motivation 23

3.2 The Effects of Lorentz Invariance Violation in the Perturbative Standard-Model Extension in Daya Bay 24

3.3 Isotropic Lorentz Invariance Violation vs. Sidereal Modulation . . 25

3.4 Hamiltonian for the Isotropic Lorentz Invariance Violation 26

3.5 Explicit Form of the Survival Probability with LIV Effect 27

3.5.1 Case-by-case Survival Probability Formulae 27

3.5.2 Full Formula Survival Probability 29

4 Non-standard Interactions in the Antineutrino Oscillations in Daya Bay 33

4.1 Common Non-unitary Approach to Non-standard Interactions 34

4.2 Our Own Non-unitary Approach to Non-standard Interactions . . 36

4.3 Specific Cases of the Mixing Matrices 38

4.3.1 Unitary Mixing with the Non-standard Interactions 38

4.3.2 Inverse Processes in the Source and the Detector 39

4.4 General Survival Probability to Use in Daya Bay 39

4.5 Discussion about Approaches to Include the Effects of Non-standard Interactions 41

5 The Daya Bay Experiment **43**
5.1 Introduction of the Daya Bay Experiment 43
5.2 Principle of the θ_{13} Measurement by Reactor Antineutrino Disappearance in Short Baselines 43
5.3 Overview of the Experimental Layout and Setup 44
5.4 The Detection Method 46
5.5 Antineutrino Detector 47
  5.5.1 Antineutrino Detector Structure 47
  5.5.2 The Calibration Instruments 49
5.6 Muon Tagging System 50
  5.6.1 Muons in Antineutrino Detector 51
  5.6.2 Water Pool 52
  5.6.3 Resistive Plate Chamber Detectors 52
5.7 Inverse Beta Decay Candidate Selection 53
5.8 Backgrounds 56
  5.8.1 Accidental Background 57
  5.8.2 Fast Neutron Background 57
  5.8.3 ^{9}Li/^{8}He Background 57
  5.8.4 α-n Background 58
  5.8.5 ^{241}Am-^{13}C Calibration Source Background 59
5.9 Data Set For the Analysis 59

6 Analysis Methods **63**
6.1 The LBNL Fitter 63
  6.1.1 Prediction of the Far Hall Spectrum from the Near Hall Measurements 63
  6.1.2 χ^2 Definition 65
  6.1.3 Covariance Matrix 66
  6.1.4 Correlations between Predictions 68
6.2 Statistical Methods 68
  6.2.1 Statistical Significance of New Physics: p-value 69
  6.2.2 Parameter Estimation - Confidence Intervals 70
  6.2.3 Exclusion Limits for the Lorentz Invariance Violation - Gaussian $\mathrm{CL_S}$ Method 71

7 Results **75**
7.1 Neutrino Oscillations in Three-neutrino Framework 75
  7.1.1 Oscillation Probability Formula and Introduction of Δm^2_{ee} 75
  7.1.2 Precise Measurement of $\sin^2 2\theta_{13}$ and Δm^2_{ee} 77
7.2 Search for Isotropic Lorentz Invariance Violation 78
  7.2.1 Significance of Lorentz Invariance Signal 78
  7.2.2 Exclusion Limits for the Standard-Model Extension Parameters using Case-by-case Formulae 80
  7.2.3 Revision of the Validity of the Assumptions for the Perturbative Expansion 84

7.2.4 Limits on the Standard-Model Extension Parameters using Case-by-case Formulae using Gaussian CL_S Method 85
7.2.5 Exclusion Limits for the X_i's using Full Formula Survival Probability 86
7.2.6 Results in the Case of Inverted Hierarchy 89
7.3 Search for Non-standard Interactions 90
7.3.1 Parameters to Constrain 91
7.3.2 Limits on $\Delta\phi$ with Unconstrained Δm^2_{ee} 93
7.3.3 Limits on $\Delta\phi$ with constrained Δm^2_{ee} 94
7.3.4 Results for Inverted Mass Hierarchy 96
7.3.5 Summary of Limits on Non-standard Interactions Parameter $\Delta\phi$ 97
7.3.6 Discussion about Constrained Absolute Antineutrino Flux 98

8 Conclusions **101**

Bibliography **103**

List of Figures **111**

List of Tables **113**

List of Abbreviations **115**

1. Introduction

Neutrinos are indeed very interesting particles. Since their postulation by W. Pauli in 1930, there have been many puzzles connected with neutrinos. Although, they are the second most abundant particle in the universe, the first challenge was even to detect them. Interacting only via weak force, their cross-section for possible detection process is very small. Nevertheless, C. Cowan and F. Reines accomplished in the first neutrino measurement [1] in Savanah River experiment in 1956 using inverse beta decay reaction. They have proved the neutrino existence by detecting the coincidence of positron annihilation and delayed neutron capture. More precisely, it was reactor electron antineutrino, which was discovered. Later, two additional neutrino flavours were discovered which makes it in total three: ν_e, ν_μ, ν_τ. They are named after leptons along with they are produced in the weak interactions.

One of the neutrino puzzles was observed in electron neutrinos coming from the Sun in the late 60s by R. Davis in the Homestake experiment [2]. The measured neutrino flux exhibited deficit in comparison with the prediction. This so-called "Solar Neutrino Problem" was in fact the first observed effect of neutrino flavour oscillations, which later served as its explanation. Today well-established phenomenon of neutrino oscillations showed us that neutrinos, at least two of them, have tiny but non-zero mass. This is in the contradiction with the Standard Model (SM) where neutrinos are massless. Neutrinos oscillations as a demonstration of non-zero neutrino mass are together with the cosmological measurement of Dark Matter [3] the only solid evidences for physics beyond the Standard Model (BSM).

Neutrino oscillations were proposed by B. Pontecorvo in 1957 [4] first as neutrino-antineutrino oscillations. Later, the theory of neutrino flavour oscillations was developed by Z. Maki, M. Nakagawa and S. Sakata [5] and since then many experiments helped to establish this mechanism to explain the flavour changes during neutrino propagation. In the beginning, the experiments observed only hints for oscillations, which can still be explained by other scenarios of flavour changing. It is usually considered that the first compelling evidence for the neutrino oscillations was provided by the Super-Kamiokande experiment, which measured the atmospheric neutrinos [6]. Later, experiment SNO finally resolved the "Solar Neutrino Problem" by measurement of total neutrino flux from the Sun being consistent with the prediction [7]. The outstanding contribution of these experiments was recognized in 2015 by the Nobel Prize committee which awarded T. Kajita and A. McDonald "for the discovery of neutrino oscillations, which shows that neutrinos have mass" [8].

After establishing the phenomenon of neutrino oscillations, we have entered the era of precision measurement of oscillation parameters. Designated experiments were built, among other the Daya Bay experiment in Southern China. Daya Bay was designed to measure at that time unknown mixing angle θ_{13}. Before 2012, there were only indications of non-zero value of this parameter. In 2012, Daya Bay with only 56 days reported the non-zero value of θ_{13} on more than 5σ significance [9]. Since then, it provides the most precise measurement up to date. The result was promptly confirmed by the RENO experiment [10], and later by the T2K [11] and Double CHOOZ [12] experiments. Precise knowledge of the mixing angle θ_{13} is crucial for current and future experiments, which aim to measure CP-violation in the lepton sector such as NOvA, T2K and Hyper-Kamiokande. The critical role of Daya Bay is more profound because there is no proper successor currently planed and the measurement of θ_{13} done by Daya Bay will remain the most precise for at least near future.

Daya Bay experiment investigates the reactor antineutrino disappearance in the short baseline ∼2 km. This is an optimal distance where the disappearance effect of reactor antineutrinos proportional to $\sin^2 2\theta_{13}$ is maximal. Daya Bay uses revolutionary technique of the relative near-far measurement first proposed by L. Mikaelyan and V. Sinev [13], which largely suppress the correlated systematic uncertainties and leave usually smaller uncorrelated uncertainties play the leading role of the uncertainty of the measurement. On the top of that, Daya Bay has what in general every neutrino experiment needs: large neutrino flux provided by are six commercial nuclear reactors with total thermal power of 17.4 GW and large target mass achieved by having 8 detector located in the underground experimental halls with total 160 tons of liquid scintillator. Moreover, Daya Bay was designed as a low background experiment having background to signal ratio better than 2.5%.

All of these factors make the experiment exceptionally sensitive to the oscillation parameters, namely mixing angle θ_{13} and effective mass squared difference Δm^2_{ee}. That allows us to go beyond original three-neutrino framework and explore scenarios of physics BSM. Daya Bay already did that with the search for possible existence of light sterile neutrino. In this thesis we focus on two other scenarios.

We first test the Lorentz Invariance violation (LIV) in the oscillations measured by the Daya Bay experiment within the framework of the Standard-Model Extension (SME). Lorentz Invariance is the fundamental symmetry, which underline the whole SM. Nevertheless, particular models of quantum gravity, the unification of general relativity and quantum field theory, predict deviation from the exact symmetry in the large energy called Planck Scale. Of course, such a scale is not directly accessible by current experiments, however, we can still observe indirect effect of new physics as a deviation from the standard prediction. The idea is similar to searches for new heavy particles. We cannot directly create them but their presence in the loops as virtual particles can be observed as a deviation from SM prediction. We understand that Lorentz Invariance violation is a sensitive topic. Therefore, we offer two ways how to think about this analysis. Either you work on quantum gravity and you can take this study as a test of your theory, or you can conservatively consider this as a test of one of the fundamental symmetries. As we will explain in detail later, we focus only on the so-called Isotropic case where the Lorentz Invariance violation does not depend on the antineutrino propagation direction. This effect would be seen in the oscillated antineutrino energy spectrum, which will have different shape than prediction of standard oscillations.

The second scenario of physics BSM we investigate in this thesis is the effect of the Non-standard Interactions (NSIs). We already consider SM as an effective low energy limit of some more general theory. That is similar for example to the Fermi theory to be low energy limit of the Intermediate Vector Boson theory.

More general theory can allow interactions which are forbidden in the SM or which are highly suppressed by the number of loops needed for their realization. Their effect for typical energies we are dealing with in our experiments will be however small. Nevertheless, powerful interferometric nature of neutrino flavour oscillations can provide an access to the indirect effect of NSIs. In general, the NSIs can appear in the process of antineutrino production, propagation and detection. For Daya Bay, we can neglect them in the propagation phase since for the Earth density and typical reactor antineutrino energy the ordinary matter effect is already negligible and any other sub-leading effect would be even smaller. Therefore for our analysis, we limit ourselves on the NSIs presented in the production and detection processes only. Such interactions will modify the shape of the oscillated antineutrino spectrum in the specific way, which will be different from the standard oscillation pattern. That makes the analysis in general similar to the case of the search for LIV.

The thesis is organized as follows. First, we will introduce the standard neutrino flavour oscillations and their modification due to the presence of LIV, or NSIs. Then we briefly describe the Daya Bay experiment and highlight the key information for the analysis. Next, we present the tool for the oscillation analysis and introduce used statistical methods. Finally, we show the results of our searches and end with conclusion remarks.

2. Neutrino Oscillations

2.1 Neutrino Properties

2.1.1 History of Neutrino

In 1930, W. Pauli postulated existence of "neutron", light neutral particle, in order to save the energy, momentum and angular momentum conservation in beta decays where continuous energy spectrum of electron was observed. It is well known that for two-body decay the energy spectrum of the products is monoenergetic therefore we need to add at least one particle to obtain continuous spectrum. Since the change of the charge of nucleus is compensated by emitted electron this additional particle has to be neutral. Pauli himself was not very happy about this new particle.

It was few years later, in 1932, when J. Chadwick proven the existence of particle we know today as neutron. The terminology was resolved by E. Fermi who came up with name "neutrino" along with his contact theory of beta decays [14]. This was big leap forward and very important contribution from E. Fermi who incorporated the at that time hypothetical particle to his theory. Shortly after, H. Bethe and R. Peierls estimated the cross-section of the interaction between neutrino and nuclei. It turned to be extremely small, $\sigma < 10^{-44}\,\mathrm{cm}^2$, which made neutrino practically undetectable [15].

It took more than two decades since the neutrino was finally discovered. In 1956, C. Cowan and F. Reines published the paper about first detection of neutrino [1]. They perform the experiment in Savannah River where they used local nuclear reactor as a powerful source of antineutrinos. They have been detected via inverse beta decay reaction on free protons:

$$\bar{\nu}_e + p \rightarrow e^+ + n \tag{2.1}$$

forming a coincidence of two signals: two gammas from positron annihilation and delayed neutron capture. This characteristic pattern is very powerful in background suppression and gives a clean antineutrino detection signal. This very method is still used up to this day in experiments such as Daya Bay, RENO and Double CHOOZ.

In 1962, L. Lederman, M. Schwetz and J. Steinberger proved that another neutrino flavour exists showing the neutrinos produced in pion decays together with muons are detected by creating muons only [16]. Therefore they posses different flavour from at that time known electron neutrino.

When third lepton τ was discovered in 1975 natural idea was to consider its neutrino partner with the same flavour. The existence of third neutrino flavour was confirmed in 2000 when experiment DONUT discovered ν_τ [17].

The budget of light active neutrinos was finalized by the experiments ALEPH, DELPHI, L3 and OPAL at the LEP accelerator at CERN. They measured the total decay width of the Z boson as well as partial visible decay widths. From these measurements and from the SM calculation of the width of invisible decay modes $Z \rightarrow \nu_\alpha \bar{\nu}_\alpha$ they concluded that the total number of active flavour neutrinos is [18]:

$$N_\nu = 2.984 \pm 0.008 \tag{2.2}$$

Let us note that this measurement does not rule out the existence of light sterile neutrinos. By sterile, we mean those, which do not interact via weak interactions. Thus even though, they are light enough that kinematics does not forbid Z boson to decay to them, there is no interaction, which can mediate it.

2.1.2 Neutrinos in the Standard Model

The Standard Model (SM) describes properties of particles and their interactions mediated by gauge bosons and their mass generation via interactions with Higgs field. There are three fundamental forces included: strong, weak and electromagnetic interaction. However, gravitational force is still not incorporated in the SM.

Neutrinos in SM are massless particles with spin $\frac{1}{2}$. They are neutral so they do not interact via electromagnetic force. Neutrinos also do not interact strongly because they do not posses any strong charge. Their only interaction with gauge bosons is weak interactions.

Neutrinos with flavour α are present is SM in so called $SU(2)_L$ doublets, where they are present together with their charge lepton partners:

$$L_\alpha = \begin{pmatrix} \nu_{\alpha L} \\ l_{\alpha L} \end{pmatrix} \quad \alpha = e,\ \mu,\ \tau \tag{2.3}$$

Relevant parts of SM Lagrangian for the neutrino interactions are charge current and neutral current:

$$\mathcal{L} = \mathcal{L}^{CC} + \mathcal{L}^{NC} = \frac{g}{\sqrt{2}} \bar{l_\alpha} \gamma_\mu \nu_\alpha W^{+\mu} + \frac{g}{2\cos\theta_W} \bar{\nu_\alpha} \gamma_\mu \nu_\alpha Z^\mu \tag{2.4}$$

Let us notice that both interactions do conserve total lepton number, moreover family lepton number. Another important fact is that there are only left-handed neutrinos in SM. Since we are missing right-handed component we cannot construct typical Dirac particle mass term and neutrino remain massless within SM. For decades, this was not an issue since direct neutrino mass measurements always results in the value compatible with zero. We were not able to measure the absolute neutrino mass directly so far.

However nowadays, we know that this is not the picture of nature. In the next section, we discuss the phenomenon of neutrino flavour oscillations, which undoubtedly proves that at least two neutrino states are massive. Being in the contradiction with SM, this is one of the few solid evidences for physics BSM. There are several BSM scenarios how to accompany massive neutrinos and explain their much smaller mass compare to other SM particles.

2.2 Neutrino Flavour Oscillations - Compelling Evidence for Neutrino Mass

The idea of neutrino oscillations was originally proposed by B. Pontecorvo in 1957 [4]. He presented neutrino oscillations $\nu \rightleftarrows \bar{\nu}$ as an analogy with oscillations of neutral kaons $K^0 \rightleftarrows \bar{K}^0$. Of course, this is not what we understand by neutrino flavour oscillations today. But at that time there was known only one neutrino flavour. After the discovery of muon neutrino, B. Pontecorvo's thoughts helped Z. Maki, M. Nakagawa and S. Sakata in the proposition of neutrino flavour oscillations $\nu_e \rightleftarrows \nu_\mu$ as we know it today [5].

Let us note that neutrino flavour oscillations as well as neutral kaon oscillations are based on the exceptional sensitivity of interferometry, which allows us to measure mass differences of kaons and neutrinos with unprecedented precision.

Neutrino flavour oscillations, described in detail below, emerge from two key ingredients:

- Neutrinos are produced or detected in weak interaction eigenstates which are not mass eigenstates
- We cannot measure which mass eigenstate is born and propagates to the detector

Neutrinos interact only via weak force therefore we can produce and detect only the neutrino flavour states which are not mass eigenstates but their linear superposition. Each mass eigenstate is produced or detected with certain amplitude. However, we cannot determine which mass state was propagating. In the language of quantum mechanics, we sum the contribution of all possible realizations on the level of amplitudes. That is where the interference occurs and neutrino oscillations arise. In this manner, neutrino oscillations are quantum mechanics phenomenon.

2.2.1 Neutrino Mixing in Three-neutrino Framework

Based on the SM let us assume that there are three neutrino flavour eigenstates ν_e, ν_μ and ν_τ. These states are weak interaction eigenstates and similar to kaons K^0 and $\bar{K}^0$ they have not definite mass rather they are linear superposition of mass eigenstates. We can express the transformation as

$$|\nu_\alpha\rangle = \sum_{i=1,2,3} U^*_{\alpha i} |\nu_i\rangle \qquad (\alpha = e, \mu, \tau) \tag{2.5}$$

where $|\nu_\alpha\rangle$ stands for neutrino eigenstate with flavour α and $|\nu_i\rangle$ stands for mass eigenstate with mass m_i.

The mixing matrix U is called after the pioneers of neutrino flavour oscillation theory Pontecorvo-Maki-Nakagawa-Sakta matrix [5]. It is commonly parametrized as:

$$U = \begin{pmatrix} 1 & 0 & 0 \\ 0 & c_{23} & s_{23} \\ 0 & -s_{23} & c_{23} \end{pmatrix} \begin{pmatrix} c_{13} & 0 & s_{13}e^{-i\delta_{CP}} \\ 0 & 1 & 0 \\ -s_{13}e^{i\delta_{CP}} & 0 & c_{13} \end{pmatrix} \begin{pmatrix} c_{12} & s_{12} & 0 \\ -s_{12} & c_{12} & 0 \\ 0 & 0 & 1 \end{pmatrix} \begin{pmatrix} 1 & 0 & 0 \\ 0 & e^{i\frac{\alpha_1}{2}} & 0 \\ 0 & 0 & e^{i\frac{\alpha_2}{2}} \end{pmatrix} \tag{2.6}$$

where $c_{ij} \equiv \cos\theta_{ij}$ and $s_{ij} \equiv \sin\theta_{ij}$. It contains six parameters. There are three mixing angles θ_{12}, θ_{23}, θ_{13}; one CP-violation phase δ_{CP} which is responsible for different oscillations of neutrinos and antineutrinos and two so-called Majorana phases α_1 and α_2, which would eventually emerge from Majorana properties of the neutrino. However, these phases do not have any effect in the neutrino oscillations and we cannot determine from the measurement of neutrino oscillations whether neutrino is Dirac or Majorana particle (i.e. if it is different from or equal to its own antiparticle).

2.2.2 Neutrino Oscillation Probability in Vacuum

According to quantum mechanics the time evolution of the quantum state is governed by equation:

$$i\frac{\partial|\psi(t)\rangle}{\partial t} = \hat{H}|\psi(t)\rangle \tag{2.7}$$

The Hamiltonian in vacuum is just kinetic term. Then the evolution of mass eigenstate is simple plane wave travelling in the direction of the neutrino momentum:

$$|\nu_i(t)\rangle = e^{-i(E_i t - p_i L)}|\nu_i\rangle \tag{2.8}$$

where E_i and p_i are the neutrino mass eigenstate energy and momentum respectively. In the ultrarelativistic limit, we can assume $t \approx L$ and write

$$E_i t - p_i L \approx E_i L - \sqrt{E_i^2 - m_i^2} L \simeq \frac{m_i^2}{2E} L + \mathcal{O}\left(m_i^4\right) \tag{2.9}$$

where in the last step we have introduced the common energy for all of the mass eigenstates. The evolution of mass eigenstate can be written as:

$$|\nu_i(L)\rangle = e^{-i\frac{m_i^2}{2E}L}|\nu_i\rangle \tag{2.10}$$

We derive Eq.(2.10) based on the ultrarelativistic limit. This is completely justified for reactor antineutrinos which typical energy is ∼4 MeV and mass of the neutrinos $\lesssim$1 eV. Thus the gamma factor is $\gamma \gtrsim 10^6$, which makes reactor antineutrinos indeed ultrarelativistic.

In our experiments, we produce flavour eigenstates rather than mass eigenstates. The time evolution of such a flavour state can be written as

$$|\nu_\alpha(L)\rangle = \sum_i e^{-i\frac{m_i^2}{2E}L} U_{\alpha i}^* |\nu_i\rangle \tag{2.11}$$

Then we can write the amplitude, and consequently probability, that we measure neutrino with flavour β while flavour α was produced. The probability is a function of propagation distance as

$$\mathcal{A}_{\nu_\alpha \to \nu_\beta}(L) = \sum_i U_{\beta i} e^{-i\frac{m_i^2}{2E}L} U_{\alpha i}^* \tag{2.12}$$

$$\mathcal{P}_{\nu_\alpha \to \nu_\beta}(L) = \left|\sum_i U_{\beta i} e^{-i\frac{m_i^2}{2E}L} U_{\alpha i}^*\right|^2 \tag{2.13}$$

Using the unitarity of mixing matrix U

$$\sum_i U_{\alpha i}^* U_{\beta i} = \delta_{\alpha\beta} \tag{2.14}$$

in the Eq.(2.13) and with little bit of mathematics we get commonly used expression for oscillation probability:

$$\begin{aligned}\mathcal{P}_{\nu_\alpha \to \nu_\beta}(L) =& \delta_{\alpha\beta} - 4\sum_{i>j} \mathrm{Re}\left(U_{\beta i} U_{\alpha i}^* U_{\beta j}^* U_{\alpha j}\right) \sin^2\left[\frac{\Delta m_{ij}^2 L}{4E}\right] \\ &+ 2\sum_{i>j} \mathrm{Im}\left(U_{\beta i} U_{\alpha i}^* U_{\beta j}^* U_{\alpha j}\right) \sin\left[\frac{\Delta m_{ij}^2 L}{2E}\right]\end{aligned} \tag{2.15}$$

where we have introduced mass squared differences $\Delta m^2_{ij} \equiv m^2_i - m^2_j$. For three combinations of $i > j$, we have only two independent mass squared differences since $\Delta m^2_{31} - \Delta m^2_{32} = \Delta m^2_{21}$.

For the terminology used in what follows, if experiment measures $\mathcal{P}_{\nu_\alpha \to \nu_\alpha}$ we call it disappearance experiment since some of the neutrinos oscillate (disappear) to other flavours. Therefore we refer to the oscillation probability also as a survival probability. If experiment searches for $\mathcal{P}_{\nu_\alpha \to \nu_\beta}$, where $\alpha \neq \beta$, we call it appearance experiment where neutrinos with flavour β appear when neutrinos with flavour α oscillate into them.

The oscillation probability in Eq.(2.15) contains all the key information about neutrino oscillation phenomenon. Observation of the typical periodically changing probability (that is why we call it oscillations) indicates that mass squared differences are non-zero hence at least some of the neutrino mass eigenstates have non-zero mass. This argument is used as a proof of massive neutrinos.

2.2.3 Relation between Neutrino and Antineutrino Oscillation Probability

Assuming CPT invariance, we can write the relation between neutrino and antineutrino oscillation probability as

$$P_{\nu_\alpha \to \nu_\beta} = P_{\overline{\nu}_\beta \to \overline{\nu}_\alpha}. \tag{2.16}$$

From Eq.(2.13) we can see that using complex conjugated elements of the matrix U, we get the oscillation probability, which corresponds to the oscillation process inverted in time. We can express this result as

$$P_{\nu_\alpha \to \nu_\beta}(U) = P_{\nu_\beta \to \nu_\alpha}(U^*). \tag{2.17}$$

Combining Eq.(2.17) and Eq.(2.16) we get

$$P_{\nu_\alpha \to \nu_\beta}(U) = P_{\overline{\nu}_\alpha \to \overline{\nu}_\beta}(U^*). \tag{2.18}$$

which expresses the relation between oscillation probability for neutrinos and antineutrinos by using complex conjugated mixing matrix U.

If the mixing matrix U is real the oscillation probability is same for neutrinos and antineutrinos. If the CP-violation phase δ_{CP} is not zero or π the probabilities are different. Anyway, if $\alpha = \beta$ it holds

$$P_{\nu_\alpha \to \nu_\alpha} = P_{\overline{\nu}_\alpha \to \overline{\nu}_\alpha}. \tag{2.19}$$

The probability that neutrino with flavour α is detected with the same flavour α is equal for neutrinos and antineutrinos.

2.3 Brief History of the Measurement of the Oscillation Parameters

The oscillation probability in Eq.(2.15) depends on six parameters. There are three mixing angles θ_{12}, θ_{23}, θ_{13}, CP-violation phase δ_{CP} and two independent mass squared differences Δm^2_{21} and Δm^2_{32} (or Δm^2_{31}). Depending on the neutrino flavour, energy and baseline, experiments are sensitive to their particular set rather than to all of them. Very different oscillation lengths governed by mass squared differences Δm^2_{21} and Δm^2_{32} and the small value of mixing angle θ_{13} allow particular experiments to perform analysis in the simplified two-neutrino approximation, where only two flavour and two mass states are assumed.

There are various neutrino sources. The typical natural sources are for example solar neutrinos, atmospheric neutrinos, geoneutrinos and supernova neutrinos. We have also artificial neutrinos sources e.g. accelerator neutrinos and reactor antineutrinos. Experiments use both natural and artificial sources.

There are various detection methods, which are used for neutrino oscillation measurements. Thee methods depends mainly on the neutrino energy, which is usually given by the properties of the neutrino source.

2.3.1 Solar Neutrinos

First observation of flavour oscillation effect was done in the famous Homestake experiment. R. Davis designed the experiment to measure neutrino flux from the Sun. The Sun should produce electron neutrinos in the thermonuclear reactions in the core. The experiment itself consists of tank with 380 m^3 of tetrachloroethylene buried 1478 m underground in the Homestake Gold Mine. The neutrino detection was performed by its capture on chlorine atoms resulting in the production of argon:

$$^{37}Cl + \nu_e \rightarrow ^{37} Ar + e^- \tag{2.20}$$

Argon atoms were then extracted and counted via its decays. We should mention that this method was first proposed by B. Pontecorvo.

R. Davis measured in average 0.437 ± 0.042 Ar atoms per day [2]. Based on the calculations of J. Bahcall [19], this was only about 30% of the theoretical prediction. This deficit in the flux of the neutrinos from the Sun was called the Solar Neutrino Problem because at that time no explanation existed. The reaction in Eq.(2.20) is sensitive to electron neutrinos only. If neutrino oscillations were true, part of the neutrinos could oscillate to different flavour and cause the deficit in the measurement. However, this result cannot be even explained by neutrino oscillations in vacuum since they could provide at maximum 50% deficit. The final solution was proposed by S. Mikheyev, A. Smirnov [20] and L. Wolfenstein [21] who included the effect of matter of the Sun. The confirmation of their hypothesis as well as J. Bahcall's calculations was presented in 2001 when the SNO experiment reported the measurement of absolute neutrino flux from the Sun regardless on the neutrino flavour [7]. This was one of the evidences for solar neutrino flavour oscillation, which brought A. McDonald the Nobel Prize in Physics in 2015 [8].

Meanwhile several other experiments measured solar neutrino flux and continuously improving our knowledge. Let us mention the SAGE experiment [22] and the GALLEX experiment [23], which used different radiochemical detection method. They used neutrino capture on atoms of Gallium converting them into Germanium

$$^{71}Ga + \nu_e \rightarrow ^{71} Ge + e^- \tag{2.21}$$

The solar neutrino experiments are sensitive to the parameters θ_{12} and Δm^2_{21}. There are therefore called solar mixing angle and solar mass squared difference. We point out that matter effect in the Sun provided us the opportunity to determine that $\Delta m^2_{21} > 0$, i.e. $m_2 > m_1$.

2.3.2 Atmospheric Neutrinos

It is widely recognized that the compelling evidence for phenomenon of neutrino flavour oscillations did not come from the solar neutrino measurement but from the different neutrino source. In 1998 the Super-Kamiokande (SK) announced results from atmospheric neutrino measurement favouring the neutrino oscillation hypothesis over other candidates of neutrino flavour changing theories [6].

SK was originally designed to measure proton lifetime. It consists of cylindrical steel tank 39.3 m in diameter and 41.4 m high with the overburden of 1000 m of the rock. There is 50 ktons of ultra-pure water. The tank itself is optically divided into inner part, 33.8 m in diameter and 36.2 m high, and outer part. There are photomultiplier tubes (PMTs) attached to the structure facing both to the inner part and outer part. SK measured atmospheric neutrino flux as a source of background for possible proton decays. Atmospheric neutrino with energy ∼GeV interacts in target volume producing charged lepton. Its energy is high enough to produce Čerenkov light cone, which imprint in the wall with PMTs as a circle. Using time information and the pattern of the ring the SK is able to reconstruct the direction of the particle and its type, electron or muon. The Čerenkov detector cannot however distinguish between neutrinos and antineutrinos.

Atmospheric neutrinos are created in the atmosphere where cosmic rays interact with the atoms of the air creating charged pions. Pions consequently decay as

$$\begin{aligned} \pi^+ &\to \mu^+\nu_\mu \to e^+ + \nu_e + \bar{\nu}_\mu + \nu_\mu \\ \pi^- &\to \mu^-\bar{\nu}_\mu \to e^- + \bar{\nu}_e + \nu_\mu + \bar{\nu}_\mu \end{aligned} \tag{2.22}$$

producing electron and muon neutrinos and antineutrinos. The flux of the atmospheric neutrinos is assumed to be almost isotropic.

SK analyzed the measured flux of atmospheric neutrinos as a function of the zenith angle (distance) and energy. The result was not like what we would expect from the isotropic flux prediction. The down-going muon neutrino flux agreed with the expectation but the deficit in up-going muon neutrino flux was observed. This was explained by the neutrino flavour oscillations when down-going muon neutrinos have to travel short distance to the Earth surface and do not have enough time to oscillate. On the contrary, up-going muon neutrinos have to travel all the way though the Earth which provides them enough time to oscillate to other flavour. Since there was no increase in the electron neutrino flux it was concluded that muon neutrinos oscillate dominantly to tau neutrinos.

Later with higher statistics, SK reported dependence of the measured muon neutrino flux over prediction as a function of parameter $\frac{L}{E}$. Traveled distance L has been determined from the zenith angle and energy E from measurement of Čerenkov light [24]. The shape of the dependence ruled out other scenarios, which tried to explain neutrino flavour changing, such as neutrino decays or decoherence. On the contrary, it favoured neutrino oscillation as a mechanism for flavour changing.

The discovery of neutrino oscillations in SK brought T. Kajita the Nobel Prize in Physics in 2015 [8].

Atmospheric neutrino experiments are sensitive mainly to the oscillation parameters θ_{23} and $|\Delta m^2_{32}|$ (or $|\Delta m^2_{31}|$). They are therefore sometimes called atmospheric parameters. These experiments as well as accelerator experiments discussed in the next section can not determine the sign of Δm^2_{32}.

2.3.3 Accelerator Neutrinos and CP-violation in Lepton Sector

The long-baseline accelerator neutrino experiments are using high-energy neutrino beams to study the neutrino oscillations. The proton beam from the accelerator hits the target producing mainly pions but also kaons. They decay producing mostly muon neutrinos. The ideal scenario is to tune the energy of the highest neutrino flux intensity in order to have the far detector in the oscillation minimum to improve the sensitivity to neutrino oscillation parameters.

The MINOS experiment was designed to measure precisely the atmospheric neutrino parameters. It uses neutrinos from Fermilab NuMI beam which spectrum has maximum around 3 GeV. The actual beam composition is measured in the Near Detector to suppress systematic uncertainties. The neutrinos travel 735 km to the Soudan Laboratory where the Far Detector is installed. On the way to Far Detector, some of ν_μ neutrinos change their flavour to another and the deficit in energy spectrum is observed. The experiment detects neutrinos through charge current reaction

$$\nu_\mu/\bar{\nu_\mu} + X \rightarrow \mu^-/\mu^+ + X' \tag{2.23}$$

The oscillation probability depends on the $\frac{L}{E}$, i.e. on energy E at fixed distance L. Precise measurement of the spectral distortion in the Far Detector gives the MINOS experiment ability to measure more precisely mass squared splitting Δm^2_{32} than the atmospheric neutrino experiments [25].

The long-baseline accelerator experiments have unique opportunity to measure the CP-violation phase δ_{CP} due the possibility of production both neutrino and antineutrino beam. The difference between oscillation probabilities $\mathcal{P}_{\nu_\mu \rightarrow \nu_e}$ and $\mathcal{P}_{\bar{\nu}_\mu \rightarrow \bar{\nu}_e}$ is a function of δ_{CP} and it is non-zero for $\delta_{CP} \neq 0$ and $\delta_{CP} \neq \pi$. The oscillation probabilities $\mathcal{P}_{\nu_\mu \rightarrow \nu_e}$ and $\mathcal{P}_{\bar{\nu}_\mu \rightarrow \bar{\nu}_e}$ are also proportional to the mixing angle θ_{13}. Before its measurement by Daya Bay experiment, there was a possibility that θ_{13} is too small that we would not be able to investigate the value of δ_{CP}. However, large value of θ_{13} with precision achieved by Daya Bay allows the measurement of CP-violation in the lepton sector.

There are currently two running experiments designed for the measurement of CP-violation phase: T2K and NOvA. They are sensitive to other oscillation parameters as well, namely θ_{23}, $|\Delta m^2_{32}|$ and θ_{13}. The NOVA experiment is using the same NuMI beam as the MINOS experiment. The Far Detector is placed 810 km far in the Ash River. The neutrino energy spectrum peaks around 2 GeV. Due to off-axis concept, the spectrum is relatively narrow which helps to reduce the background and there is higher flux in the energy range important for oscillations.

Both experiments, T2K [26] and NOvA [27], announced their first analysis of the possible CP-violation in the lepton sector at the NEUTRINO 2016 conference.

Their results combined with the Daya Bay measurement of θ_{13} suggests non-zero CP-violation in the lepton sector. This is more than welcomed by cosmologists because such a violation can help to create matter-antimatter asymmetry in the early universe via process called leptogenesis [28]. CP-violation in the quark sector itself is not powerful enough to create the size of asymmetry we observe nowadays.

2.3.4 Reactor Antineutrino Measurement

As we discussed above, reactor antineutrinos were the first detected neutrinos. Since then, they are used in various experiments. Reactor antineutrinos are produced in the radioactive β^- decays of the neutron rich fission products in the nuclear reactors. The reactors are ideal source of purely electron antineutrinos.

The Kamioka Liquid Scintillator Antineutrino Detector (KamLAND) was the first experiment that measured neutrino oscillations of reactor antineutrinos. It detected antineutrinos from Japanese commercial nuclear reactors with weighted average distance of ∼180 km. The detector itself is a stainless steel sphere 18 m in diameter with PMTs mounted on the inner surface. The sphere contains nylon ballon of 13 m in diameter filled with liquid scintillator. Between the ballon and the stainless vessel there is a mineral oil to shield from natural radioactivity. The whole sphere is put into the water pool used as a muon detector.

The detection method of the neutrinos uses the coincidence of prompt and delayed signals of particles produced in the inverse beta decay reaction:

$$\bar{\nu_e} + p \rightarrow n + e^+ \tag{2.24}$$

Prompt signal was created by the scintillation light from the positron energy losses and the following $2 \times 511\,\mathrm{keV}$ positron annihilation gammas. Delayed signal came from the neutron capture on hydrogen in average ∼180 μs after prompt signal emitting single 2.23 MeV gamma.

The KamLAND experiment, like solar neutrino experiments, confirmed antineutrino disappearance on the medium baselines being sensitive to oscillation parameters Δm^2_{21} and θ_{12}. The precision of the Δm^2_{21} is better in KamLAND, however, it can not compete with solar neutrino experiments in precision of θ_{12}. KamLAND and solar neutrino experiments are in this sense complementary. The KamLAND experiment is the first experiment, which observed oscillatory behaviour of the oscillation probability. It first directly measured the increase of the survival probability after it initially decreases moving far from the source.

The other experiment, which used reactor antineutrinos for the measurement of the neutrino oscillations, was the CHOOZ experiment. Having the detector placed 1050 m from the nuclear core the experiment aimed to investigate the electron antineutrino oscillations in the short baselines. This could give an access to at that time unknown mixing angle θ_{13}.

The detector was placed underground with the overburden of about 300 m.w.e. in order to shield against the cosmic rays. Detector itself was a stainless steel tank 5.5 m high and 5.5 m in diameter. There were two nested vessels inside dividing the detector into three zones. The inner vessel was made from highly transparent Plexiglas while the outer vessel was opaque in order to prevent gammas go in or out. The innermost region was filled with liquid scintillator doped with gadolinium. The middle region was filled with pure liquid scintillator to capture escaping gammas from the inner zone. There were PMTs mounted on the outer vessel facing inwards. The outer part contained PMTs and was filled liquid scintillator. This zone was used for muon veto.

The antineutrinos were measured using inverse beta decay reaction. Unlike KamLAND, the CHOOZ experiment used gadolinium-doped liquid scintillator to capture delayed neutrons. Gadolinium has large cross-section for thermal neutron capture. More importantly, there is released gamma cascade after the neutron capture with total energy about 8 MeV. For this energy the background rate is significantly lower since the energy spectrum of natural radioactivity basically vanishes above 3 MeV.

The CHOOZ experiment was able to set the upper limit on $\sin^2(2\theta_{13}) < 0.17$ at 90% confidence level [29]. The largest systematic uncertainty came from the uncertainty of antineutrino flux despite the effort to reduce it by detailed simulation of the reactor core and application of previous flux measurements done by the Bugey-3 experiment [30].

2.3.5 Entering the Era of Precision Measurement of Oscillation Parameters

When the phenomenon of neutrino oscillations was established we entered to the era of precision measurement of oscillation parameters. Designated experiments were built either to measure parameters more accurate or measure those still unknown. We have already mentioned accelerator neutrino experiments NOvA and T2K which aim to measure CP-violation phase δ_{CP}, neutrino mass hierarchy etc.

In order to measure the CP-violation phase δ_{CP}, we have to know the value of θ_{13} because there is an ambiguity between these parameters. In extreme case, when $\theta_{13} = 0$ or $\theta_{13} = \pi$ there is no room for CP-violation in the lepton sector. Therefore, there was a strong campaign in last decade to measure θ_{13} in order to set future strategy to the CP-violation measurement. Several experiments were proposed and built: Daya Bay, RENO, Double CHOOZ, NOvA and T2K.

There are future experiments under construction or proposed which perform even more precise measurement of oscillation parameters and resolve still unanswered questions in neutrino oscillations. The JUNO experiment [31] aims to measure reactor antineutrinos. There will be DUNE [32] and Hyper-Kamiokande [33] experiments with accelerator and atmospheric neutrinos. All these experiments are rather complementary and they will provide us deep insight into neutrino properties.

2.3.6 Road to Mixing Angle θ_{13}

In 2011, more than a decade after the CHOOZ experiment reported the upper limit on mixing angle θ_{13}, T2K experiment presented indication of non-zero mixing angle θ_{13} [34]. The T2K experiment is long-baseline accelerator neutrino experiment. It uses neutrino beam produced at J-PARC, which is sent to 295 km far Super-Kamikande detector mentioned before. The peak of the energy spectrum is tuned to be in the first oscillation maximum, i.e. $E_\nu = 0.6$ GeV.

With 1.43×10^{20} proton on target T2K has observed 6 electron neutrino candidates while 1.5 ± 0.3 were expected. Under the neutrino flavour oscillation framework this rules out $\theta_{13} = 0$ hypothesis with 2.5σ significance [34]. Recent results from T2K support the electron neutrino appearance hypothesis with significance of 7.3σ [11].

Later, in the end of 2011, the experiment Double CHOOZ presented their measurement and confirmed with what we already knew from T2K. Their result disfavoured $\theta_{13} = 0$ hypothesis at 1.9σ significance [35].

The Double CHOOZ experiment was designed to have two detectors, near detector located close to nuclear reactor, which is used as a source of antineutrinos and far detector sensitive to the oscillation effects. The experiment actually uses formal CHOOZ experimental site for the deployment of its far detector in the distance $L = 1050$ m from the reactors. For the 2011 result, the near detector was not installed therefore single Double CHOOZ was conceptually same as the CHOOZ experiment only with more advanced detector. The main sources of systematical uncertainties, e.g. uncertainty in antineutrino flux, were still present and limited the capabilities of the experiment. The near detector started data taking in 2015.

Finally in March 2012, the experiment Daya Bay was the first, which beyond all doubts observed reactor antineutrinos disappearance consistent with neutrino flavour oscillations. Experiment measured non-zero mixing angle θ_{13} with the significance of 5.2σ. Based on the rate-only analysis the deficit was consistent with the value $\sin^2(2\theta_{13}) = 0.092 \pm 0.016(\text{stat}) \pm 0.005(\text{syst})$ [9].

The non-zero θ_{13} was promptly confirmed by the RENO experiment. We should mention that RENO was the first neutrino oscillation experiment which ran with the near-far detector configuration used also in Daya Bay (see Sec.5.1 for more details about the configuration advantages). Nowadays, we have already several measurements of mixing angle θ_{13}. The most precise measurement of mixing angle θ_{13} was reported recently by Daya Bay experiment with the value of $\sin^2(2\theta_{13}) = 0.0841 \pm 0.0027(\text{stat}) \pm 0.0019(\text{syst})$ [36].

2.3.7 Neutrino Flavour Oscillation Parameter Values and Open Questions in Neutrino Oscillations

In the end of this chapter, we would like to summarize the measurement of neutrino oscillation parameters in three-neutrino framework. There are three mixing angles θ_{12}, θ_{23}, θ_{13} and two independent mass squared differences Δm^2_{21} and Δm^2_{32} all measured with certain precision.

However, there are still three major questions unanswered in neutrino oscillations. First of course is the value of CP-violation phase δ_{CP}, which remain unknown. Nevertheless, there have been recently some promising results by NOvA and T2K in this regard. Second, as we have discussed before, we do not know the sign of Δm^2_{32}. This gives rise to two potential neutrino mass hierarchies. Normal hierarchy is called the case when $\Delta m^2_{32} > 0$ and inverted hierarchy is the case $\Delta m^2_{32} < 0$. The illustration of two possible hierarchies is shown in Fig.2.1.

Resolving neutrino mass hierarchy is one of the current goals of neutrino oscillation physics. Future experiments JUNO, DUNE and HyperKamiokande will likely answer this question. DUNE and HyperKamiokande will also aim to

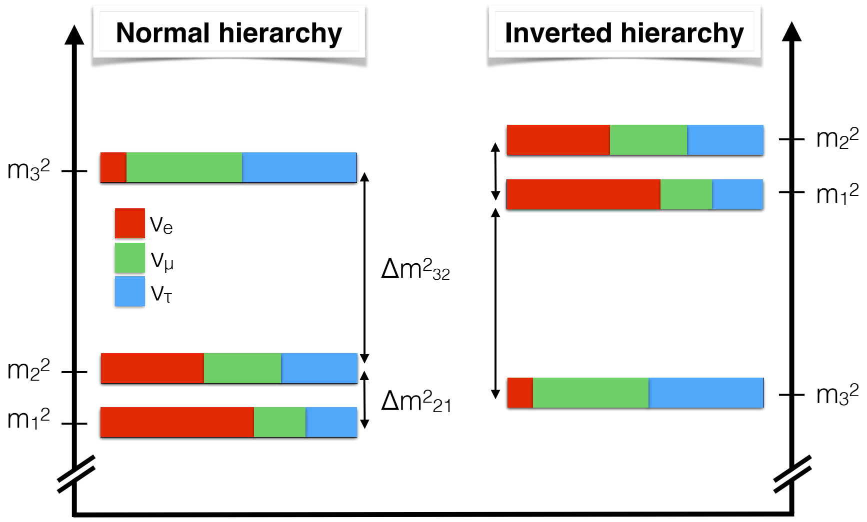

Figure 2.1: Illustration of the normal and inverted mass hierarchies. The colours represent the amount of flavour state in the particular mass state.

resolve third questions of neutrino physics and that is the quadrant of mixing angle θ_{23}, i.e. $\theta_{23} \lesseqgtr 45°$. Octant ambiguity cannot be addressed by JUNO since the electron antineutrino disappearance probability does not depend on θ_{23}. Currently, data favours two values, one slightly below 45° and one slightly above but still indistinguishable at 3σ confidence level, see Tab.2.1.

Tab.2.1 summarizes current the combined global best-fit oscillation parameters for both normal and inverted neutrino mass hierarchy.

Parameter	Best fit $\pm 1\sigma$	3σ range
$\sin^2\theta_{12}$	$0.302^{+0.013}_{-0.012}$	$0.267 - 0.344$
$\sin^2\theta_{23}$	$0.413^{+0.037}_{-0.025}$ or $0.594^{+0.021}_{-0.022}$	$0.342 - 0.667$
$\sin^2\theta_{13}$	$0.0227^{+0.0023}_{-0.0024}$	$0.0156 - 0.0299$
Δm^2_{21}	$7.50^{+0.18}_{-0.19} \times 10^{-5}$ eV^2	$(7.00 - 8.09) \times 10^{-5}$ eV^2
Δm^2_{31} for NH	$2.473^{+0.070}_{-0.067} \times 10^{-3}$ eV^2	$(2.276 - 2.695) \times 10^{-3}$ eV^2
Δm^2_{32} for IH	$-2.427^{+0.042}_{-0.065} \times 10^{-3}$ eV^2	$(-2.649 - -2.242) \times 10^{-3}$eV^2
δ_{CP}	$300^{+66}_{-138}\,^{\circ}$	$0 - 360°$

Table 2.1: Global best fit of neutrino flavour oscillation parameters. We show best-fit value with $\pm 1\sigma$ deviation and 3σ range. More details in [37]

Part of the oscillation parameters will be improved in near future by the JUNO experiment. The experiment will measure the disappearance of reactor antineutrino in the medium baseline exploring mixing parameters θ_{12} and Δm^2_{21}. On top of that, due to its excellent precision, the JUNO experiment aims to observe sub-leading oscillation pattern governed by the mass squared difference Δm^2_{32} (Δm^2_{31}). It will be the first experiment to measure simultaneously both types of oscillations. JUNO measurement will lead to significant reduction of the uncertainty of oscillation parameters, see Tab.2.2.

Parameter	Current rel. uncertainty	Improved uncertainty by JUNO
$\sin^2\theta_{12}$	4.1%	0.67%
Δm^2_{21}	2.6%	0.59%
Δm^2_{ee}	~2.8%	0.44%

Table 2.2: Parameters which can JUNO improve and their expected relative uncertainty after 6 years of running [38]. Δm^2_{ee} is effective mass square splitting, linear combination of the factors depending on Δm^2_{32} and Δm^2_{31}. The current global uncertainty is approximately the uncertainty of Δm^2_{32}.

2.3.8 Other Questions in Neutrino Physics

We would like to briefly discuss two other question in neutrino physics which are not accessible in the oscillation measurements. First is the absolute scale of neutrino masses. We do not now the mass of the lightest neutrino, which is illustrated on Fig.2.1 by the broken y-axis. We are not able to anchor three mass states knowing only the mass differences between them. The closest experiment to provide the answer or set the better upper limit on the neutrino mass is the KATRIN experiment. It aims to measure the high energy end of the electron spectrum in the decay of tritium:

$$^3H \rightarrow ^3 He + \bar{\nu}_e + e \tag{2.25}$$

The KATRIN sensitivity can set the upper limit on effective $\bar{\nu}_e$ mass $m_e < 0.2$ eV [39].

Another question we already briefly mentioned above is the Dirac of Majorana nature of neutrino. Majorana neutrinos are suggested by most of the theories trying to explain generation of neutrino mass. The current effort in this regard is focused on the measurement of neutrinoless double beta decay and similar reactions like double electron capture. While neutrino flavour oscillations violate the family lepton number but still conserved the total lepton number, Majorana neutrinos would violate the total lepton number by two in the neutrinoless double beta decay. Various experiments are currently under operation, however, no experimental evidence of Majorana neutrinos was obtained yet.

3. Test of the Lorentz Invariance in the Antineutrino Oscillations in Daya Bay

3.1 Motivation

The main goal of the Daya Bay experiment was the discovery of non-zero value of mixing angle θ_{13}. This goal was successfully accomplished in 2012 [9]. Due to the relatively large value of θ_{13} and high precision achieved in the experiment we are able to go beyond the standard three-neutrino framework of massive neutrinos and extend out search for the effects of new physics.

One of such scenarios is the potential breaking of the Lorentz Invariance. It is considered to be fundamental symmetry of the nature. Nevertheless, certain candidates for description of the quantum gravity [40] suggest its violation at high energy scale known as the Planck mass ($M_P \simeq 10^{-19}$ GeV). Lorentz Invariance corresponds to the independence of the laws of physics on the orientation or the boost of the laboratory frame. This symmetry underlies Special Relativity, which makes it one of the basics components of both General Relativity (GR) and the Standard Model (SM), our most successful descriptions of nature to date. Despite the success of our current theories, it can be expected that GR and the SM unify at an energy scale at which quantum and gravitational effects are comparable in magnitude. Here is where we could expect Lorentz Invariance violation (LIV).

Further motivation is that every search for the potential LIV works as a test of one of the fundamental symmetries of the nature. That is always beneficial since it can make us more confident in our description of laws of physics.

Even though the Planck mass is out of direct experimental reach with our current technology, indirect effects could be observable in sensitive experimental setups. The interferometric properties of neutrino oscillations offers us useful probe to these effects. The hint of presence of LIV could be observed as a deviation from the prediction of the standard oscillations.

A systematic study of Lorentz Invariance violation can be performed using the so-called Standard-Model Extension (SME) [41, 42, 43], a general framework based on effective quantum field theory that parametrizes any potential deviation from exact Lorentz Invariance. In addition to the SM Lagrangian, SME may contain other terms, which are not by construction Lorentz invariant. Each term has its own in general independent coupling constant. Many experiments performed search for Lorentz Invariance violation using SME framework. They use various probes include photons, electrons, protons, neutrons, neutrinos, muons, quarks, neutral mesons, gluons, and gravity [44]. To date, no hint of Lorentz Invariance violation was observed resulting in the limits on SME parameters. Nevertheless, only small part of SME parameters was explored.

In the neutrino sector [45, 46], LIV effects have been already studied by several experiments including Double Chooz [47, 48], IceCube [49], LSND [50], MiniBooNE [51, 52], MINOS [53, 54, 55, 56], and Super-Kamiokande [57]. Daya Bay experiment with its ability to perform very precise measurement can join this effort.

3.2 The Effects of Lorentz Invariance Violation in the Perturbative Standard-Model Extension in Daya Bay

Like other experiments, we will use SME to describe the potential Lorentz Invariance violation in neutrino oscillations in Daya Bay. We will follow the procedure described in [58] to derive the survival probability $P_{\bar{\nu}_e \to \bar{\nu}_e}$, which contain such effects.

In SME, the effect of LIV can be introduced by effective Hamiltonian schematically written as:

$$h_{eff} = h_0 + \delta h \tag{3.1}$$

where h_0 is the Lorentz invariant part of the SM and δh represents the LIV effects. For more details, see [58]. Since no hint of the violation was observed so far we can assume that $\delta h << h_0$ and write the oscillation amplitude schematically as a perturbative expansion in the powers of δh:

$$S_{\bar{e}\bar{e}} = S^{(0)}_{\bar{e}\bar{e}} + S^{(1)}_{\bar{e}\bar{e}} + S^{(2)}_{\bar{e}\bar{e}} + ... \tag{3.2}$$

and consequently the oscillation probability as:

$$P_{\bar{\nu}_e \to \bar{\nu}_e} = \left| S^{(0)}_{\bar{e}\bar{e}} + S^{(1)}_{\bar{e}\bar{e}} + S^{(2)}_{\bar{e}\bar{e}} + ... \right|^2 = P^{(0)}_{\bar{\nu}_e \to \bar{\nu}_e} + P^{(1)}_{\bar{\nu}_e \to \bar{\nu}_e} + P^{(2)}_{\bar{\nu}_e \to \bar{\nu}_e} + ... \tag{3.3}$$

Since we assume that $\delta h << h_0$, then $P^{(0)}_{\bar{\nu}_e \to \bar{\nu}_e} >> P^{(1)}_{\bar{\nu}_e \to \bar{\nu}_e} >> P^{(2)}_{\bar{\nu}_e \to \bar{\nu}_e} ...$ and we can consider only leading order of the LIV effect, i.e. 1st perturbative order:

$$P_{\bar{\nu}_e \to \bar{\nu}_e} = P^{(0)}_{\bar{\nu}_e \to \bar{\nu}_e} + P^{(1)}_{\bar{\nu}_e \to \bar{\nu}_e}. \tag{3.4}$$

The zeroth order of the survival probability $P^{(0)}_{\bar{\nu}_e \to \bar{\nu}_e} = \left| S^{(0)}_{\bar{e}\bar{e}} \right|^2$ represents the the standard mass-driven oscillation probability, where the zeroth order amplitude is:

$$S^{(0)}_{\bar{e}\bar{e}} = S^{(0)}_{ee} = \sum_{i=1,2,3} |U_{ei}|^2 \, e^{-iE_i L}, \tag{3.5}$$

Here we use notation

$$E_1 L = 0, \qquad E_2 L = \frac{2.53 \Delta m^2_{21} [\mathrm{eV}^2] L[\mathrm{m}]}{E[\mathrm{MeV}]}, \qquad E_3 L = \frac{2.53 \Delta m^2_{31} [\mathrm{eV}^2] L[\mathrm{m}]}{E[\mathrm{MeV}]}. \tag{3.6}$$

We keep bared indexes to identify, that we are calculating the probability for antineutrinos. However, it is not important for the Lorentz Invariance conserving part, it is crucial for the LIV part of the probability

Specifically, the zeroth order probability takes the expected form:

$$\begin{aligned} P^{(0)}_{\bar{\nu}_e \to \bar{\nu}_e} = 1 &- \sin^2 2\theta_{12} \cos^4 \theta_{13} \sin^2 \left(\frac{\Delta m^2_{21} L}{4E} \right) \\ &- \sin^2 2\theta_{13} \sin^2 \theta_{12} \sin^2 \left(\frac{\Delta m^2_{32} L}{4E} \right) \\ &- \sin^2 2\theta_{13} \cos^2 \theta_{12} \sin^2 \left(\frac{\Delta m^2_{31} L}{4E} \right) \end{aligned} \tag{3.7}$$

where E is the antineutrino energy and L is the baseline.

The Lorentz Invariance violating part of the probability for antineutrinos in Eq. (3.4) is given by

$$P^{(1)}_{\bar{\nu}_e\to\bar{\nu}_e} = 2L\,\mathrm{Im}\Big[S^{(0)*}_{\bar{e}\bar{e}}\,\mathcal{H}^{(1)}_{\bar{e}\bar{e}}\Big]. \tag{3.8}$$

The factor $\mathcal{H}^{(1)}_{\bar{e}\bar{e}}$, which depends on energy and baseline, takes the form of

$$\mathcal{H}^{(1)}_{\bar{e}\bar{e}} = \sum_{\bar{\alpha},\bar{\beta}=\bar{e},\bar{\mu},\bar{\tau}} (\mathcal{M}^{(1)}_{\bar{e}\bar{e}})_{\bar{\alpha}\bar{\beta}}\;\delta h_{\bar{\alpha}\bar{\beta}}. \tag{3.9}$$

In this expression, the oscillation channel dependent factors $(\mathcal{M}^{(1)}_{\bar{e}\bar{e}})_{\bar{\alpha}\bar{\beta}}$ are given by:

$$\begin{aligned}(\mathcal{M}^{(1)}_{\bar{e}\bar{e}})_{\bar{\alpha}\bar{\beta}} &= \sum_{\bar{i},\bar{j}=1,2,3} \tau^{(1)}_{\bar{i}\bar{j}}\;U_{\bar{e}\bar{i}}U^*_{\bar{\alpha}\bar{i}}U_{\bar{\beta}\bar{j}}U^*_{\bar{e}\bar{j}} \\ &= \sum_{i,j=1,2,3} \tau^{(1)}_{ij}\;U^*_{ei}U_{\alpha i}U^*_{\beta j}U_{ej},\end{aligned} \tag{3.10}$$

where we use the complex conjugate mixing matrix transforming from antineutrinos (bared indexes) to neutrinos (non-bared indexes). The $\delta h_{\bar{\alpha}\bar{\beta}}$ is the LIV Hamiltonian, which contains the effective coupling constants of the LIV term of SME. The functions $\tau^{(1)}_{ij}$ are defined as:

$$\tau^{(1)}_{ij}(E,L) = \begin{cases} e^{-iE_jL}, & E_i = E_j, \\ \dfrac{e^{-iE_iL} - e^{-iE_jL}}{-i\Delta_{ij}L}, & E_i \neq E_j. \end{cases} \tag{3.11}$$

where $\Delta_{ij} \equiv E_i - E_j$. We remind that here we use the notation for E_iL shown in Eq.(3.6).

Using Eq.(3.9) and Eq.(3.8) in Eq.(3.4), we can write the survival probability as:

$$P_{\bar{\nu}_e\to\bar{\nu}_e} = P^{(0)}_{\bar{\nu}_e\to\bar{\nu}_e} + 2L\,\mathrm{Im}\Big[S^{(0)*}_{\bar{e}\bar{e}} \sum_{\bar{\alpha},\bar{\beta}=\bar{e},\bar{\mu}\bar{\tau}} (\mathcal{M}^{(1)}_{\bar{e}\bar{e}})_{\bar{\alpha}\bar{\beta}}\;\delta h_{\bar{\alpha}\bar{\beta}}\Big]. \tag{3.12}$$

3.3 Isotropic Lorentz Invariance Violation vs. Sidereal Modulation

The violation of Lorentz Invariance breaks the idea of the independence of laws of physics on the boost and the orientation on the frame. This suggests existence of the preferred global orientation (preferred frame). It is reflected in the Lorentz Invariance violating Hamiltonian $\delta h_{\bar{\alpha}\bar{\beta}}$, which can be decomposed to the form of:

$$\begin{aligned}\delta h_{\bar{\alpha}\bar{\beta}} = (\mathcal{C})_{\bar{\alpha}\bar{\beta}} &+ (\mathcal{A}_s)_{\bar{\alpha}\bar{\beta}}\,\sin\omega_\oplus T_\oplus + (\mathcal{A}_c)_{\bar{\alpha}\bar{\beta}}\,\cos\omega_\oplus T_\oplus \\ &+ (\mathcal{B}_s)_{\bar{\alpha}\bar{\beta}}\,\sin 2\omega_\oplus T_\oplus + (\mathcal{B}_c)_{\bar{\alpha}\bar{\beta}}\,\cos 2\omega_\oplus T_\oplus\end{aligned} \tag{3.13}$$

where the amplitudes are given explicitly in [58]. The $T_\oplus$ is the sidereal time and $\omega_\oplus \equiv 2\pi/(23\text{ h }56\text{ min})$ is the sidereal frequency, i.e. the frequency of the Earth rotation with respect to the fixed stars. The Hamiltonian is now the function of the sidereal time $T_\oplus$ which express the changing orientation with respect to the preferred global orientation frame. While the Earth is rotating, this time-dependence would result in periodical time-changing oscillations. There is also term $(\mathcal{C})_{\bar{\alpha}\bar{\beta}}$ which is not a function of the sidereal time but still contain the LIV effects. We refer to this case as the Isotropic Lorentz Invariance violation, more simply Isotropic case, since it does not depend on the orientation.

Searches for both cases, sidereal-time dependent oscillations and Isotropic Lorentz Invariance violation, are rather complementary and can be easily separated at Daya Bay. If we investigate the time-dependent oscillations, the isotropic term $(\mathcal{C})_{\bar{\alpha}\bar{\beta}}$ will result just in the increase or decrease of the standard oscillation effect due to the mixing angle θ_{13}. On the other hand, in the search for the Isotropic Lorentz Invariance violation the time-dependent LIV will average out if our data acquisition period spans over large number of sidereal days. In case of Daya Bay data, it is hundreds of periods.

In this thesis we will limit our focus on the Isotropic Lorentz Invariance violation case only. Such effects could be observed in the shape of the oscillated antineutrino energy spectrum, which is modified from the standard oscillation prediction by the presence of LIV.

3.4 Hamiltonian for the Isotropic Lorentz Invariance Violation

For the isotropic case the Hamiltonian takes form:

$$\delta h_{\bar{\alpha}\bar{\beta}} = (\mathcal{C})_{\bar{\alpha}\bar{\beta}} = (a_R)^T_{\bar{\alpha}\bar{\beta}} - \frac{1}{2}(c_R)^{TT}_{\bar{\alpha}\bar{\beta}}\big(3-\hat{N}^Z\hat{N}^Z\big)E + \frac{1}{2}(c_R)^{ZZ}_{\bar{\alpha}\bar{\beta}}\big(1-3\hat{N}^Z\hat{N}^Z\big)E \tag{3.14}$$

where the indexes T, X, Y, Z stands for four spacetime coordinates and $\hat{N}^i$ is component of vector $(\hat{N}^X, \hat{N}^Y, \hat{N}^Z)$ which represents the neutrino propagation direction in the Sun-centered frame at $T_\oplus = 0$.

The label R indicates that the coefficients refer to right-handed antineutrinos. It is important to notice that the spacetime trace of the tensor $(c_R)^{\alpha\beta}_{\bar{\alpha}\bar{\beta}}$ is Lorentz invariant, so the Lorentz Invariance violating part can be taken as traceless. In other words, $(c_R)^{ZZ}_{\bar{\alpha}\bar{\beta}} = \frac{1}{3}\,(c_R)^{TT}_{\bar{\alpha}\bar{\beta}}$ and the Hamiltonian takes the simple form

$$\delta h_{\bar{\alpha}\bar{\beta}} = (a_R)^T_{\bar{\alpha}\bar{\beta}} - \frac{4}{3}E(c_R)^{TT}_{\bar{\alpha}\bar{\beta}} \tag{3.15}$$

Moreover, in order to compare with the studies from other experiments, we can relate the right-handed coefficients to the left-handed coefficients in the form

$$(a_R)^T_{\bar{\alpha}\bar{\beta}} = -(a_L)^{T*}_{\alpha\beta}, \tag{3.16}$$

$$(c_R)^{TT}_{\bar{\alpha}\bar{\beta}} = (c_L)^{TT*}_{\alpha\beta} \tag{3.17}$$

where minus sign emerges due to the CPT-violating nature of the operator associated with the coefficient $(a_R)^T_{\bar{\alpha}\bar{\beta}}$. The final form of the Hamiltonian is then

$$\delta h_{\bar{\alpha}\bar{\beta}} = -(a_L)^{T*}_{\alpha\beta} - \frac{4}{3}E(c_L)^{TT*}_{\alpha\beta} \tag{3.18}$$

3.5 Explicit Form of the Survival Probability with LIV Effect

There are more SME parameters needed for the most general description of the LIV effect in the Daya Bay than the experiment can constrain. In this section we present two different approaches how to deal with this issue. In the first approach we turn on only some SME parameters keeping the others to zero. We refer to this as the case-by-case approach, see Sec.3.5.1. The advantage is the reduction of free parameters, which allows us to set constraints on actual SME parameters which we turned on. In the second approach, we combine the effect of all relevant SME parameters into effective parameters. This action reduces the number of free parameters to constrain. The advantage is that we keep the most general LIV effects but we can set constraints only on specific combinations of the SME parameters. We refer to this approach as the full formula, see Sec.3.5.2. Let us now derive the survival probabilities for these two approaches.

3.5.1 Case-by-case Survival Probability Formulae

The case-by-case approach assumes only particular set of the SME parameters to be non-zero. This approach is commonly used in the analysis and adopt by other neutrinos experiments as well, e.g. Double Chooz [47, 48] and Super-Kamiokande [57]. The advantage is that we can set limits on the actual SME parameters $(a_L)^T_{\alpha\beta}$ and $(c_L)^{TT}_{\alpha\beta}$ since we reduce the number of fitted parameters. In order to do that we adopt procedure turning on only one particular flavour combination $\alpha\beta$ while keeping the other SME parameters corresponding to different flavour combinations zero. In some cases, we might even turn on only one SME parameter, see results of our analysis in Sec.7.2.4. Obviously, the disadvantage is that we neglect contribution of some of the LIV terms. Although, we relaxed on the most general case of LIV, fortuitous cancellations between different coefficients are unlikely because each coefficient of the Hamiltonian $h_{\bar{\alpha}\bar{\beta}}$ is coupled to a different experimental factor $(\mathcal{M}^{(1)}_{\bar{e}\bar{e}})_{\bar{\alpha}\bar{\beta}}$, which depend on the antineutrino energy. For this reason, any cancellation would occur at a well-defined energy but not for all values of the antineutrino energy spectrum. Therefore, if there would be some LIV, we would observe it anyway.

Let us now take step-by-step only one non-zero component of the Lorentz Invariance violating Hamiltonian $\delta h_{\bar{\alpha}\bar{\beta}}$ at a time. The hermiticity of the Hamiltonian $\delta h^*_{\bar{\alpha}\bar{\beta}} = \delta h_{\bar{\beta}\bar{\alpha}}$ implies that there are six out of nine independent components of $\bar{\alpha}\bar{\beta}$ combinations. These six independent components can be separated into two general groups: $\bar{\alpha} = \bar{\beta}$ and $\bar{\alpha} \neq \bar{\beta}$.

- $\bar{\alpha} = \bar{\beta}$: in this case, the components of the Hamiltonian are real and the probability Eq. (3.12) takes the form

$$P_{\bar{\nu}_e\to\bar{\nu}_e} = P^{(0)}_{\bar{\nu}_e\to\bar{\nu}_e} + 2L\,\mathrm{Im}\Big[S^{(0)*}_{\bar{e}\bar{e}}(\mathcal{M}^{(1)}_{\bar{e}\bar{e}})_{\bar{\alpha}\bar{\alpha}}\Big]\,\delta h_{\bar{\alpha}\bar{\alpha}} \tag{3.19}$$

  Recall that the indexes $\bar{\alpha}\bar{\alpha}$ take the values $\bar{\alpha}\bar{\alpha} = \bar{e}\bar{e}, \bar{\mu}\bar{\mu}, \bar{\tau}\bar{\tau}$.

- $\bar{\alpha} \neq \bar{\beta}$: It can be shown that if conventional CP violation is neglected ($\delta_{CP} = 0$), then the experimental factors satisfy $(\mathcal{M}^{(1)}_{\bar{e}\bar{e}})_{\bar{\beta}\bar{\alpha}} = (\mathcal{M}^{(1)}_{\bar{e}\bar{e}})_{\bar{\alpha}\bar{\beta}}$. We adopt this value of CP violation phase for the convenience. The qualitative result of LIV remain unchanged, however the quantitative result must be corrected when the real value of δ_{CP} will be measured. With this assumption, the probability Eq. (3.12) can be written as

$$\begin{aligned} P_{\bar{\nu}_e\to\bar{\nu}_e} &= P^{(0)}_{\bar{\nu}_e\to\bar{\nu}_e} + 2L\,\mathrm{Im}\Big[S^{(0)*}_{\bar{e}\bar{e}}\Big((\mathcal{M}^{(1)}_{\bar{e}\bar{e}})_{\bar{\alpha}\bar{\beta}}\,\delta h_{\bar{\alpha}\bar{\beta}} + (\mathcal{M}^{(1)}_{\bar{e}\bar{e}})_{\bar{\beta}\bar{\alpha}}\,\delta h_{\bar{\beta}\bar{\alpha}}\Big)\Big] \\ &= P^{(0)}_{\bar{\nu}_e\to\bar{\nu}_e} + 2L\,\mathrm{Im}\Big[S^{(0)*}_{\bar{e}\bar{e}}(\mathcal{M}^{(1)}_{\bar{e}\bar{e}})_{\bar{\alpha}\bar{\beta}}\left(\delta h_{\bar{\alpha}\bar{\beta}} + \delta h_{\bar{\beta}\bar{\alpha}}\right)\Big] \\ &= P^{(0)}_{\bar{\nu}_e\to\bar{\nu}_e} + 4L\,\mathrm{Im}\Big[S^{(0)*}_{\bar{e}\bar{e}}(\mathcal{M}^{(1)}_{\bar{e}\bar{e}})_{\bar{\alpha}\bar{\beta}}\Big]\,\mathrm{Re}(\delta h_{\bar{\alpha}\bar{\beta}}), \end{aligned} \tag{3.20}$$

where the indexes take the values $\bar{\alpha}\bar{\beta} = \bar{e}\bar{\mu}, \bar{e}\bar{\tau}, \bar{\mu}\bar{\tau}$.

We plug Eq.(3.18) in Eqs.(3.19), Eq.(3.20) and change $(\mathcal{M}^{(1)}_{\bar{e}\bar{e}})_{\bar{\alpha}\bar{\beta}} \to (\mathcal{M}^{(1)}_{ee})_{\alpha\beta}$ and $S^{(0)*}_{\bar{e}\bar{e}} \to S^{(0)*}_{ee}$ in order to obtain the survival probabilities for the six independent flavour components $\alpha\beta$, now with non-bared indexes. Then we can finally get the exact form of the six case-by-case survival probability formulae.

$\underline{\alpha = \beta}$

The three relevant probabilities take the form:

- ee

$$P_{\bar{\nu}_e\to\bar{\nu}_e} = P^{(0)}_{\bar{\nu}_e\to\bar{\nu}_e} - 2L\,\mathrm{Im}\Big[S^{(0)*}_{ee}(\mathcal{M}^{(1)}_{ee})_{ee}\Big]\Big[(a_L)^T_{ee} + \frac{4}{3}E(c_L)^{TT}_{ee}\Big] \tag{3.21}$$

- $\mu\mu$

$$P_{\bar{\nu}_e\to\bar{\nu}_e} = P^{(0)}_{\bar{\nu}_e\to\bar{\nu}_e} - 2L\,\mathrm{Im}\Big[S^{(0)*}_{ee}(\mathcal{M}^{(1)}_{ee})_{\mu\mu}\Big]\Big[(a_L)^T_{\mu\mu} + \frac{4}{3}E(c_L)^{TT}_{\mu\mu}\Big] \tag{3.22}$$

- $\tau\tau$

$$P_{\bar{\nu}_e\to\bar{\nu}_e} = P^{(0)}_{\bar{\nu}_e\to\bar{\nu}_e} - 2L\,\mathrm{Im}\Big[S^{(0)*}_{ee}(\mathcal{M}^{(1)}_{ee})_{\tau\tau}\Big]\Big[(a_L)^T_{\tau\tau} + \frac{4}{3}E(c_L)^{TT}_{\tau\tau}\Big] \tag{3.23}$$

$\underline{\alpha \neq \beta}$

The other three probabilities take the form:

- $e\mu$

$$P_{\bar{\nu}_e\to\bar{\nu}_e} = P^{(0)}_{\bar{\nu}_e\to\bar{\nu}_e} - 4L\,\mathrm{Im}\Big[S^{(0)*}_{ee}(\mathcal{M}^{(1)}_{ee})_{e\mu}\Big]\Big[\mathrm{Re}(a_L)^T_{e\mu} + \frac{4}{3}E\,\mathrm{Re}(c_L)^{TT}_{e\mu}\Big] \tag{3.24}$$

- $e\tau$

$$P_{\bar{\nu}_e\to\bar{\nu}_e} = P^{(0)}_{\bar{\nu}_e\to\bar{\nu}_e} - 4L\,\mathrm{Im}\Big[S^{(0)*}_{ee}(\mathcal{M}^{(1)}_{ee})_{e\tau}\Big]\Big[\mathrm{Re}(a_L)^T_{e\tau} + \frac{4}{3}E\,\mathrm{Re}(c_L)^{TT}_{e\tau}\Big] \tag{3.25}$$

- $\mu\tau$

$$P_{\bar{\nu}_e\to\bar{\nu}_e} = P^{(0)}_{\bar{\nu}_e\to\bar{\nu}_e} - 4L\,\mathrm{Im}\Big[S^{(0)*}_{ee}(\mathcal{M}^{(1)}_{ee})_{\mu\tau}\Big]\Big[\mathrm{Re}(a_L)^T_{\mu\tau} + \frac{4}{3}E\,\mathrm{Re}(c_L)^{TT}_{\mu\tau}\Big] \tag{3.26}$$

We are allowed to take off the bars above the indexes since the zeroth order amplitude in Eq.(3.5) is same for neutrinos and antineutrinos as we already discussed before. Since we set $\delta_{\text{CP}} = 0$ the mixing matrix is real. Using definition in Eq.(3.10) we can prove that $(\mathcal{M}^{(1)}_{\bar{e}\bar{e}})_{\bar{\alpha}\bar{\beta}} = (\mathcal{M}^{(1)}_{ee})_{\alpha\beta}$.

The survival probabilities for different cases of the flavour combinations are shown in Fig. 3.1 for Daya Bay near Hall distance 561 m and the Far Hall distance 1579 m. We include the case of Lorentz Invariance conservation. From Fig. 3.1, it is possible to see that presence of LIV deviates the oscillation pattern from the standard oscillation picture. This modification is a function of antineutrino energy.

3.5.2 Full Formula Survival Probability

Let us now investigate the most general survival probability in the first order of perturbative expansion in SME. The cancellation of the LIV effect is improbable, nevertheless, there might still be some suppression, which could not be observed in the case-by-case analysis since only some SME parameters are considered nonzero.

Combining Eqs.(3.21)-(3.26) the most general formula takes following form:

$$\begin{aligned}
P_{\bar{\nu}_e\to\bar{\nu}_e} = P^{(0)}_{\bar{\nu}_e\to\bar{\nu}_e} &- 2L\,\text{Im}\Big[S^{(0)*}_{ee}(\mathcal{M}^{(1)}_{ee})_{ee}\Big]\Big[(a_L)^T_{ee} + \frac{4}{3}E(c_L)^{TT}_{ee}\Big] \\
&- 2L\,\text{Im}\Big[S^{(0)*}_{ee}(\mathcal{M}^{(1)}_{ee})_{\mu\mu}\Big]\Big[(a_L)^T_{\mu\mu} + \frac{4}{3}E(c_L)^{TT}_{\mu\mu}\Big] \\
&- 2L\,\text{Im}\Big[S^{(0)*}_{ee}(\mathcal{M}^{(1)}_{ee})_{\tau\tau}\Big]\Big[(a_L)^T_{\tau\tau} + \frac{4}{3}E(c_L)^{TT}_{\tau\tau}\Big] \\
&- 4L\,\text{Im}\Big[S^{(0)*}_{ee}(\mathcal{M}^{(1)}_{ee})_{e\mu}\Big]\Big[\text{Re}(a_L)^T_{e\mu} + \frac{4}{3}E\,\text{Re}(c_L)^{TT}_{e\mu}\Big] \\
&- 4L\,\text{Im}\Big[S^{(0)*}_{ee}(\mathcal{M}^{(1)}_{ee})_{e\tau}\Big]\Big[\text{Re}(a_L)^T_{e\tau} + \frac{4}{3}E\,\text{Re}(c_L)^{TT}_{e\tau}\Big] \\
&- 4L\,\text{Im}\Big[S^{(0)*}_{ee}(\mathcal{M}^{(1)}_{ee})_{\mu\tau}\Big]\Big[\text{Re}(a_L)^T_{\mu\tau} + \frac{4}{3}E\,\text{Re}(c_L)^{TT}_{\mu\tau}\Big]
\end{aligned} \tag{3.27}$$

This expression contains twelve SME parameters, six $(a_L)^T_{\alpha\beta}$'s and six $(c_L)^{TT}_{\alpha\beta}$'s. We shall use case-by-case approach where we reduce their number. Using particular assumptions we can recast the formula to the simpler form. Let us calculate the exact form for term:

$$\text{Im}\left[S^{(0)*}_{ee}\left((\mathcal{M}^{(1)}_{ee})_{\alpha\beta}\right)\right]. \tag{3.28}$$

In our calculations we neglect terms with Δm^2_{21} for $P^{(1)}_{\bar{\nu}_e\to\bar{\nu}_e}$ term by using formal limit $\Delta m^2_{21} = 0$. The effect of Δm^2_{21}-driven oscillations is in Daya Bay already small for classical case therefore any suppression by SME parameters makes it negligible. This is a follow-up of our assumption that LIV effect is small compare to the standard oscillation effect expressed previously by the assumption $\delta h << h_0$. With $\Delta m^2_{21} = 0$ assumption we have $\Delta m^2_{32} = \Delta m^2_{31} = \Delta m^2$. From Eq. (3.11) we get:

$$\tau^{(1)}_{11}(E,L) = \tau^{(1)}_{22}(E,L) = \tau^{(1)}_{21}(E,L) = 1 \tag{3.29a}$$

$$\tau^{(1)}_{33}(E,L) = exp\left(-i\frac{\Delta m^2 L}{2E}\right) \tag{3.29b}$$

$$\tau_{31}^{(1)}(E,L) = \tau_{31}^{(1)}(E,L) = i\frac{exp\left(-i\frac{\Delta m^2 L}{2E}\right)-1}{\frac{\Delta m^2 L}{2E}} \tag{3.29c}$$

For completeness, let us note that $\tau_{ij}^{(1)}(E,L) = \tau_{ji}^{(1)}(E,L)$. Then the term in Eq. (3.28) gets the form of:

$\underline{\alpha = \beta}$

$$\begin{aligned} Im\left[S_{ee}^{(0)*}\left((\mathcal{M}_{ee}^{(1)})_{\alpha\alpha}\right)\right] =& U_{e3}^2\left[(\delta_{e\alpha} - U_{e3}U_{\alpha3})^2 - U_{\alpha3}^2\left(1-U_{e3}^2\right)\right]\sin\frac{\Delta m^2 L}{2E} \\ &- 2U_{e3}U_{\alpha3}\left(\delta_{e\alpha} - U_{e3}U_{\alpha3}\right)\left(1-2U_{e3}^2\right)\frac{\sin^2\frac{\Delta m^2 L}{4E}}{\frac{\Delta m^2 L}{4E}} \end{aligned} \tag{3.30}$$

$\underline{\alpha \neq \beta}$

$$\begin{aligned} Im\left[S_{ee}^{(0)*}\left((\mathcal{M}_{ee}^{(1)})_{\alpha\beta}\right)\right] &= U_{e3}^2\left[U_{e1}U_{e2}\left(U_{\alpha1}U_{\beta2} + U_{\beta1}U_{\alpha2}\right) - U_{\alpha3}U_{\beta3}\right]\sin\frac{\Delta m^2 L}{2E} \\ - U_{e3}\left(1-2U_{e3}^2\right)&\left[U_{\alpha3}\left(\delta_{e\beta} - U_{e3}U_{\beta3}\right) + U_{\beta3}\left(\delta_{e\alpha} - U_{e3}U_{\alpha3}\right)\right]\frac{\sin^2\frac{\Delta m^2 L}{4E}}{\frac{\Delta m^2 L}{4E}} \end{aligned} \tag{3.31}$$

From Eq. (3.30) and Eq. (3.31), we can see that only two particular combinations of energy E and distance L have emerged for all combinations α and β, namely $\sin\frac{\Delta m^2 L}{2E}$ and $\frac{\sin^2\frac{\Delta m^2 L}{4E}}{\frac{\Delta m^2 L}{4E}}$. That allows us to write the full survival probability in the form of:

$$\begin{aligned} &P_{\bar{\nu}_e\to\bar{\nu}_e} = P_{\bar{\nu}_e\to\bar{\nu}_e}^{(0)} + P_{\bar{\nu}_e\to\bar{\nu}_e}^{(1)} = \\ &P_{\bar{\nu}_e\to\bar{\nu}_e}^{(0)} - 2L\left[(X_1 + X_2 E)\sin\frac{\Delta m_{ee}^2 L}{2E} + (X_3 + X_4 E)\frac{\sin^2(\frac{\Delta m_{ee}^2 L}{4E})}{\frac{\Delta m_{ee}^2 L}{4E}}\right] \end{aligned} \tag{3.32}$$

where we identify effective mass squared difference Δm_{ee}^2 [59] with Δm^2, the only mass squared splitting considered in $P_{\bar{\nu}_e\to\bar{\nu}_e}^{(1)}$ above. The X_i's represent linear combination of $(a_L)_{\alpha\beta}^T$'s and $(c_L)_{\alpha\beta}^T$'s for different flavour combinations weighted by coefficients given in Eq.(3.30) and Eq.(3.31). Definition and use of effective mass squared difference Δm_{ee}^2 is discussed later in Sec.7.1.

In detail, parameters X_1 and X_3 are linear combination of 6 $(a_L)_{\alpha\beta}^T$'s while parameters X_2 and X_4 are linear combination of 6 $(c_L)_{\alpha\beta}^T$'s. Using Daya Bay measurement, we can set constraints on parameters X_i's. Let us note that X_i's parameters themselves contain the effect of LIV. Setting them to zero, we restore standard oscillation probability with Lorentz Invariance conservation.

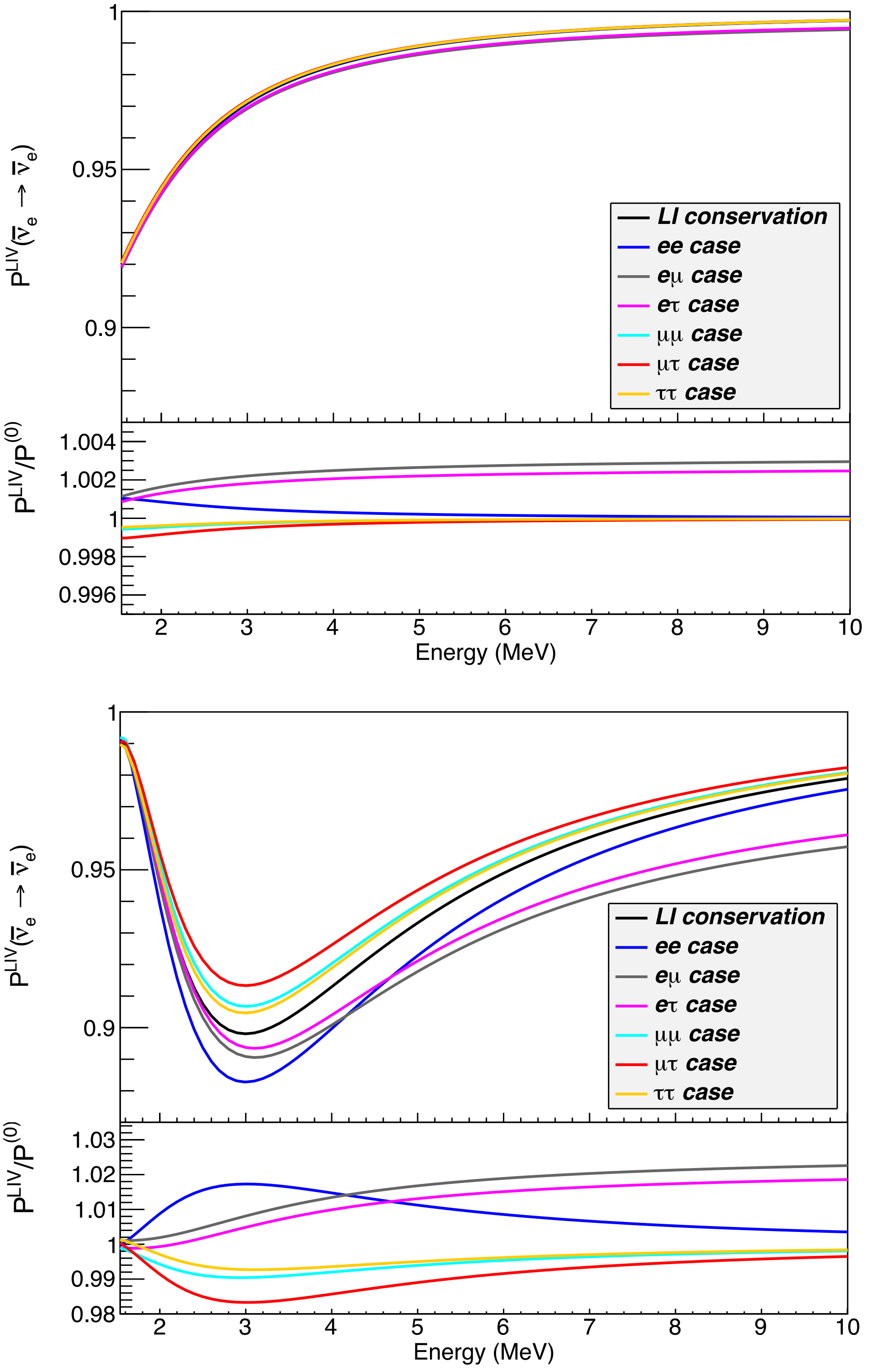

Figure 3.1: Antineutrino survival probability with respect to antineutrino energy for different cases shown in Eqs.(3.21)-(3.26). Top panel: Near hall, L=561 m. Bottom panel: Far Hall, L=1579 m. We used $((a_L)^T_{\alpha\beta}, (c_L)^{TT}_{\alpha\beta})$=($10^{-20}$ GeV, -10^{-18}) for all LIV cases. We included the case of Lorentz Invariance conservation (black line). We have used common values $\sin^2 2\theta_{13} = 0.084$ and $\Delta m^2_{ee} = 2.48 \times 10^{-3}$ eV^2. The lower panel of each figure shows the ratio of each case with LIV over the case of Lorentz Invariance conservation.

4. Non-standard Interactions in the Antineutrino Oscillations in Daya Bay

The observation of neutrino oscillations resulting in non-zero neutrino mass is the ultimate proof for the physics BSM. Theory in which massive neutrinos are incorporated must be in this sense more general than SM. Although, SM remains one of the most successful theories describing the particles and their interactions. We do not reject it rather than think about it as an effective low energy limit of some more general model.

More general theory has to contain massive neutrinos but may introduce new particles and interactions. Even though, the new particles are not in our direct experimental reach, the indirect effects can be observed as a deviation from prediction of SM. The interactions forbidden or highly suppress in SM can be enhanced by the presence of new physics. These so-called Non-standard Interactions (NSIs) could be observed in Daya Bay due to its exceptional sensitivity.

If m_X is the energy scale of new physics, we can expect the deviation from SM due to NSIs in the order of $\sim\left(\frac{m_W}{m_X}\right)^2$ where the m_W is the mass of the W vector boson. Having new physics just at TeV scale the size of new physics is not higher than few percent relative to the SM processes. Similar size of NSI effects can be expected in the neutrino oscillations. Since current limits on NSIs parameters are still quite loose [60] we need very precise experiments such as Daya Bay to further constrain the NSIs.

At energy scales $\mu << m_W$, we can use effective Lagrangian to describe the neutrino interactions. The SM interactions are reduced to:

$$\mathcal{L}_\nu = -\frac{G_F}{\sqrt{2}}\left(\bar{\nu}_\alpha\gamma^\rho(1-\gamma^5)l_\alpha\right)\left(\bar{f}'\gamma_\rho(1-\gamma^5)f\right) \tag{4.1}$$

and

$$\mathcal{L}_{MSW} = -\frac{G_F}{\sqrt{2}}\left(\bar{\nu}_\alpha\gamma^\rho(1-\gamma^5)\nu_\alpha\right)\left(\bar{f}\gamma_\rho(1-\gamma^5)f\right) \tag{4.2}$$

where f, f' are fermionic fields, l_α is the charge lepton field and ν_α is the neutrino field with flavour α. The G_F is famous Fermi constant. Similarly, we can write the effective Lagrangian for NSIs as:

$$\begin{aligned}\mathcal{L}_{NSI} =&\mathcal{L}_{V\pm A} + \mathcal{L}_{S\pm P} + \mathcal{L}_T = \\ =&-\frac{G_F}{\sqrt{2}}\sum_{f,f'}\varepsilon_{\alpha\beta}^{f,f',V\pm A}\left(\bar{\nu}_\beta\gamma^\rho(1-\gamma^5)l_\alpha\right)\left(\bar{f}'\gamma_\rho(1\pm\gamma^5)f\right) + ...\end{aligned} \tag{4.3}$$

where we write in detail only the relevant part for the Daya Bay with relative coupling constants $\varepsilon_{\alpha\beta}^{f,f',V\pm A}$. The $\mathcal{L}_{NSI}$ can be decomposed to the parts according to their Lorentz structure, nevertheless, we can neglect effect of some of the operators in Daya Bay. The scalar and pseudoscalar as well as tensor part is highly suppressed. We can neglect NSIs in the neutrino propagation since for the

Earth density and typical reactor antineutrino energy the ordinary matter effect is already negligible and any other sub-leading effect would be even smaller.

In our analysis, we consider NSIs presented in the production and detection processes only. Together, they will modify the shape of the oscillated antineutrino energy spectrum in the specific way, which will be different from the standard oscillation pattern. Other way round, we can use the possible modification of the shape of the energy spectrum to constrain the NSIs.

4.1 Common Non-unitary Approach to Non-standard Interactions

In the section we present the commonly used phenomenological formalism for the description of NSIs effects. It was used previously for the study of reactor neutrinos e.g. in [61], [62], [63] and for Daya Bay we have explored the potential of the experiment to constrain NSIs parameters in [64]. The approach motivated by the terms in effective Lagrangian introduces combination of neutrino SM flavour states: source flavour state $|\nu^s_\alpha\rangle$ and detector flavour state $\left|\nu^d_\alpha\right\rangle$. Similarly to the SM they are named after the involved lepton. However, they are not pure SM flavour states but mix the effects of SM and NSIs. Neutrinos born in the source can be treated as a superposition of vacuum flavour eigenstates

$$|\nu^s_\alpha\rangle = \frac{1}{N^s_\alpha}\left(|\nu_\alpha\rangle + \sum_{\beta=e,\mu,\tau} \varepsilon^s_{\alpha\beta}\,|\nu_\beta\rangle\right). \tag{4.4}$$

Similarly for detector, we get

$$\left\langle\nu^d_\alpha\right| = \frac{1}{N^d_\alpha}\left(\langle\nu_\alpha| + \sum_{\beta=e,\mu,\tau} \varepsilon^d_{\beta\alpha}\,\langle\nu_\beta|\right). \tag{4.5}$$

Matrices ε^s, ε^d parametrize size of the NSIs in the source and detector respectively. They are in general arbitrary matrices, however, some particular theories of massive neutrinos can impose relations between the matrices elements. The N^s_α and N^d_α which are appropriate normalization factors

$$N^s_\alpha = \sqrt{[(\mathbb{1}+\varepsilon^s)(\mathbb{1}+\varepsilon^{s\dagger})]_{\alpha\alpha}} \tag{4.6}$$

$$N^d_\beta = \sqrt{[(\mathbb{1}+\varepsilon^d)(\mathbb{1}+\varepsilon^{d\dagger})]_{\beta\beta}} \tag{4.7}$$

We should stress that elements of matrices ε^s and ε^d are effective combinations of the coupling constants appearing in effective Lagrangian in Eq.(4.3). Therefore formalism presented in this section is phenomenological description of NSIs and does not offer the opportunity to constrain actual NSIs coupling constants.

The neutrino weak flavour eigenstates are linked to the mass eigenstates by standard Pontecorvo-Maki-Nakagawa-Sakata matrix U described in Eq.(2.6) as:

$$|\nu_\alpha\rangle = U_{\alpha i}|\nu_i\rangle \tag{4.8}$$

For ν_α^s and ν_α^d we can write:

$$\begin{aligned} |\nu_\alpha^s\rangle &= V_{\alpha\beta}^s U_{\beta i}|\nu_i\rangle \\ \left|\nu_\alpha^d\right\rangle &= V_{\alpha\beta}^d U_{\beta i}|\nu_i\rangle \end{aligned} \tag{4.9}$$

where

$$V_{\alpha\beta}^s = \frac{1}{N_\alpha^s}\left(\delta_{\alpha\beta} + \varepsilon_{\alpha\beta}^s\right) \qquad V_{\alpha\beta}^d = \frac{1}{N_\alpha^d}\left(\delta_{\alpha\beta} + \varepsilon_{\alpha\beta}^d\right) \tag{4.10}$$

The transformation between flavour source/detector states and mass states is in general non-unitary. This is a result of the form of $\mathcal{L}_{NSI}$ in Eq.(4.3) where SM neutrino flavour state α does not have to be produced along with lepton with flavour α. This non-unitarity however does not imply that we are loosing neutrinos. The total lepton number in SM+NSIs is conserved. Only the family lepton number can be violated in the process of neutrino production or detection by the presence of NSIs.

In case of NSIs the electron neutrino survival amplitude $\mathcal{A}\left(\nu_e^s \to \nu_e^d, L\right) \equiv \mathcal{A}(L)$ is

$$\begin{aligned} \mathcal{A}(L) = \langle\nu_e^d|\exp -iHL|\nu_e^s\rangle &= \frac{1}{N_e^s N_e^d}(\mathbb{1} + \varepsilon^d)_{\alpha e} A_{\alpha\beta}(\mathbb{1} + \varepsilon^s)_{e\alpha} \\ &= \frac{1}{N_e^s N_e^d}\left[A + \varepsilon^s A + A\varepsilon^d + \varepsilon^s A \varepsilon^d\right]_{ee} \end{aligned} \tag{4.11}$$

where L is the propagation distance and A is the matrix of standard amplitudes without the presence of NSIs:

$$A_{\alpha\beta} = \sum_i U_{\alpha i}^* U_{\beta i} \exp\left(-i\frac{m_i^2 L}{2E}\right) \tag{4.12}$$

Combining Eq.(4.12) and Eq.(4.11) we get

$$\mathcal{A}(L) = \sum_i \mathcal{T}_i \exp\left(-i\frac{m_i^2 L}{2E}\right) \tag{4.13}$$

where

$$\begin{aligned} \mathcal{T}_i = \frac{1}{N_e^s N_e^d}\Bigg(& U_{ei}^* U_{ei} + \sum_{\gamma=e,\mu,\tau} \varepsilon_{e\gamma}^s U_{\gamma i}^* U_{ei} + \sum_{\gamma=e,\mu,\tau} \varepsilon_{e\gamma}^d U_{ei}^* U_{\gamma i} \\ & + \sum_{\gamma=e,\mu,\tau}\sum_{\lambda=e,\mu,\tau} \varepsilon_{e\gamma}^s \varepsilon_{e\lambda}^d U_{\gamma i}^* U_{\lambda i}\Bigg) \end{aligned} \tag{4.14}$$

Then it is straightforward to get the survival probability

$$\begin{aligned} P_{\nu_e^s \to \nu_e^d}(L) = \sum_{i,j} \mathcal{T}_i \mathcal{T}_j^* &- 4\sum_{i>j} \mathrm{Re}\left(\mathcal{T}_i \mathcal{T}_j^*\right) \sin^2\left(\frac{\Delta m_{ij}^2 L}{4E}\right) \\ &+ 2\sum_{i>j} \mathrm{Im}\left(\mathcal{T}_i \mathcal{T}_j^*\right) \sin\left(\frac{\Delta m_{ij}^2 L}{2E}\right) \end{aligned} \tag{4.15}$$

where $\Delta m_{ij}^2 \equiv m_i^2 - m_j^2$.

Since Daya Bay experiment investigate the reactor electron antineutrinos we have to calculate the oscillation probability for those. Like in classical case we obtain the probability for antineutrinos by switching $(U, \varepsilon) \to (U^*, \varepsilon^*)$. That is equivalent to switching $\mathcal{T} \to \mathcal{T}^*$ in Eq.(4.15). Then the survival probability for antineutrinos is

$$\begin{aligned} P_{\bar{\nu}_e^s \to \bar{\nu}_e^d}(L) = \sum_{i,j} \mathcal{T}_i^* \mathcal{T}_j - 4 \sum_{i>j} \mathrm{Re}\,(\mathcal{T}_i^* \mathcal{T}_j) \sin^2 \left(\frac{\Delta m_{ij}^2 L}{4E} \right) \\ + 2 \sum_{i>j} \mathrm{Im}\,(\mathcal{T}_i^* \mathcal{T}_j) \sin \left(\frac{\Delta m_{ij}^2 L}{2E} \right) \end{aligned} \tag{4.16}$$

By definition, the survival probability reduces to the standard case without NSIs in the limit $\varepsilon \to 0$. Another interesting fact is that the term $\sum_{i,j} \mathcal{T}_i^* \mathcal{T}_j$ in Eq.(4.16) which does not depend on antineutrino energy or propagation distance can be in general less than one. This will result in zero-distance deficit of neutrinos where the presence of NSIs can be observed in very short distances. The effect has the same signature as oscillation to sterile neutrinos with $\Delta m_{41}^2 \sim 1$ eV^2. There are in general two sources of this effect. The NSIs processes can be different in the source and in the detector resulting in $\varepsilon^s \neq \varepsilon^{d\dagger}$, i.e. the states with the same flavour in source and in detector are not in general orthogonal. But even if the processes in the source and detector are the same i.e. $\langle \nu_\alpha^d | \nu_\alpha^s \rangle = 1$ the non-unitarity of the mixing matrices in Eq.(4.10) itself is able to generate zero-distance effect. In conclusion, such a zero-distance effect can be source of the so-called reactor anomaly and can serve as its possible explanation. For completeness let us mention that reactor anomaly refers to the phenomenon where reactor experiments including Daya Bay [65] measure lower antineutrino flux than it is expected based on the predictions.

The formalism presented above is illustrative in the introduction of the effect of NSIs. However, we can question whether we can start with description by Lagrangian, which is part of the quantum-field theory domain, and use it for the quantum mechanics description of neutrino oscillations. Also, the final survival probability formula is complicated and rather unintuitive. For these reasons we have decided to develop our own phenomenological approach to the NSIs in the Daya Bay.

4.2 Our Own Non-unitary Approach to Non-standard Interactions

The flavour states are orthogonal in SM, it no longer have to be true if we introduce terms from effective Lagrangian in Eq.(4.3). Let us now present slightly different but completely legitimate derivation of the survival probability in the presence on NSIs. We use the phenomenological approach based purely on the quantum mechanics like it is used for the derivation of the standard neutrino oscillations.

We start from the mixing shown in Eq.(4.9) where we merge two matrices into one getting:

$$
\begin{aligned}
|\nu_\alpha^s\rangle &= \frac{1}{\sqrt{N_\alpha^s}} M_{\alpha i}^s |\nu_i\rangle \\
\left|\nu_\alpha^d\right\rangle &= \frac{1}{\sqrt{N_\alpha^d}} M_{\alpha i}^d |\nu_i\rangle
\end{aligned}
\tag{4.17}
$$

The matrices M^s and M^d are in general non-unitary. Let us from now focus on electron flavour only since this is the relevant one for our search for NSIs in Daya Bay. We can write the electron flavour states in the source and in the detector as:

$$
\begin{aligned}
|\nu_e^s\rangle &= \frac{1}{\sqrt{N_e^s}} \left(M_1^s|\nu_1\rangle + M_2^s|\nu_2\rangle + M_3^s|\nu_3\rangle\right) \\
\left|\nu_e^d\right\rangle &= \frac{1}{\sqrt{N_e^d}} \left(M_1^d|\nu_1\rangle + M_2^d|\nu_2\rangle + M_3^d|\nu_3\rangle\right)
\end{aligned}
\tag{4.18}
$$

where we have omitted to write lower script e for the $M^{s/d}$ elements. The normalization factors are defined to satisfy condition

$$
1 = \langle \nu_e^{s/d} | \nu_e^{s/d} \rangle = \frac{1}{N_e^{s/d}} \left(\sum_i |M_i^{s/d}|^2 \right) \tag{4.19}
$$

The oscillation amplitude is given as

$$
\mathcal{A} = \langle \nu_e^d | \nu_e^s(L,E) \rangle = \frac{1}{\sqrt{N_e^s}} \frac{1}{\sqrt{N_e^d}} \left(\sum_i M_i^s M_i^{d*} e^{i\frac{m_i^2 L}{2E}} \right) \tag{4.20}
$$

and the corresponding oscillation probability is

$$
\begin{aligned}
P_{\nu_e\to\nu_e} = \frac{1}{N_e^s}\frac{1}{N_e^d} \Bigg(& |M_1^s|^2|M_1^d|^2 + |M_2^s|^2|M_2^d|^2 + |M_3^s|^2|M_3^d|^2 \\
& + \sum_{i>j} 2\mathrm{Re}\left(M_i^s M_i^{d*} M_j^{s*} M_j^d e^{i\frac{\Delta m_{ij}^2 L}{2E}} \right) \Bigg)
\end{aligned}
\tag{4.21}
$$

where

$$
\frac{1}{N_e^s}\frac{1}{N_e^d} = \frac{1}{\left(|M_1^s|^2 + |M_2^s|^2 + |M_3^s|^2\right)\left(|M_1^d|^2 + |M_2^d|^2 + |M_3^d|^2\right)} \tag{4.22}
$$

If we parametrize

$$
M_i^{s/d} = |M_i^{s/d}| e^{i\phi_i^{s/d}} \tag{4.23}
$$

we get

$$
\begin{aligned}
P_{\nu_e\to\nu_e} = \frac{1}{N_e^s}\frac{1}{N_e^d} \Bigg[& \left(|M_1^s||M_1^d| + |M_2^s||M_2^d| + |M_3^s||M_3^d|\right)^2 \\
& - 4\sum_{i>j} |M_i^{s*}||M_i^d||M_j^s||M_j^{d*}| \sin^2\left(\frac{\Delta m_{ij}^2 L}{4E} + \frac{\Delta\phi_{ij}}{2} \right) \Bigg]
\end{aligned}
\tag{4.24}
$$

where $\Delta\phi_{ij} \equiv (\phi_i^d - \phi_i^s) - (\phi_j^d - \phi_j^s)$.

In the case of electron antineutrino, we use, similarly to standard oscillations, complex conjugated mixing matrices. That result in the survival probability formula:

$$P_{\bar{\nu}_e \to \bar{\nu}_e} = \frac{1}{N_e^s}\frac{1}{N_e^d}\Bigg[\left(|M_1^s||M_1^d| + |M_2^s||M_2^d| + |M_3^s||M_3^d|\right)^2 \\ - 4\sum_{i>j} |M_i^s||M_i^{d*}||M_j^{s*}||M_j^d| \sin^2\left(\frac{\Delta m_{ij}^2 L}{4E} - \frac{\Delta\phi_{ij}}{2}\right)\Bigg] \tag{4.25}$$

The survival probability is different for neutrinos and antineutrinos even for the disappearance measurement $\bar{\nu}_e \to \bar{\nu}_e$.

We can easily prove that such a probability we have derived above is always lower or equal to one, i.e. it is a legitimate probability. The term in Eq.(4.25) dependent on the energy and distance is at most zero (or lower). Therefore, it is enough to show that

$$\frac{\left(|M_1^s||M_1^d| + |M_2^s||M_2^d| + |M_3^s||M_3^d|\right)^2}{\left(|M_1^s|^2 + |M_2^s|^2 + |M_3^s|^2\right)\left(|M_1^d|^2 + |M_2^d|^2 + |M_3^d|^2\right)} \leq 1 \tag{4.26}$$

which reduce to prove that

$$2|M_1^s||M_1^d||M_2^s||M_2^d| + 2|M_1^s||M_1^d||M_3^s||M_3^d| + 2|M_2^s||M_2^d||M_3^s||M_3^d| \leq \\ |M_1^s|^2|M_2^d|^2 + |M_2^s|^2|M_1^d|^2 + |M_1^s|^2|M_3^d|^2 + |M_3^s|^2|M_1^d|^2 + |M_2^s|^2|M_3^d|^2 + |M_3^s|^2|M_2^d|^2 \tag{4.27}$$

which can be recast as

$$0 \leq (|M_1^s||M_2^d| - |M_2^s||M_1^d|)^2 + (|M_1^s||M_3^d| - |M_3^s||M_1^d|)^2 + (|M_2^s||M_3^d| - |M_3^s||M_2^d|)^2 \tag{4.28}$$

which is always satisfied.

If we look closely to Eq.(4.25), we can see that formula is very similar to the one for classical oscillations. There are however few differences due to NSIs. First, the absolute term does not have to be in general one, thus we can get zero-distance effect, compatible with reactor anomaly. Also, the additional phases, which can be different in the source and in the detector, makes the oscillation start with phase different from zero. This phase can be in general different for different oscillation sectors ij.

4.3 Specific Cases of the Mixing Matrices

As we have discussed, the mixing matrices for the source and for the detector in Eq.(4.17) can be in general non-unitary and independent on each other. However, specific cases motivated by the theory can introduce unitarity or relations between the matrices. We will in brief describe two of them.

4.3.1 Unitary Mixing with the Non-standard Interactions

The neutrino mass states are orthogonal by definition since they are different particles. In the past, orthogonality was assumed for the flavour states too. Mainly due to the fact that flavour states were considered to be particles themselves. Of course, the oscillations were not established at that time to provide the full picture. Actually, the orthogonality of flavour states was assumed by Lederman, Schwartz and Steinberger in their experiment which showed that muon neutrino is different from electron neutrino [16].

The orthogonality of the flavour states can be still conserved in the presence of NSIs picking only part of the terms in the effective Lagrangian in Eq.(4.3). If we assume that the transformation between flavour and mass states has to be done via unitary mixing matrix:

$$|\nu_\alpha^s\rangle = U_{\alpha i}^{s*}|\nu_i\rangle \tag{4.29}$$

$$|\nu_\alpha^d\rangle = U_{\alpha i}^{d*}|\nu_i\rangle \tag{4.30}$$

Nevertheless, the NSIs can still be different in the source and in the detector resulting in two unitary mixing matrices U^s and U^d. The oscillation probability does not change qualitatively from the general case in Eq.4.25. It still contains phases $\Delta\phi_{ij}$ and the absolute term can be lower than one.

4.3.2 Inverse Processes in the Source and the Detector

The effect of NSIs is process dependent. This is generally true since the terms in the effective Lagrangian can contribute only in specific processes within SM. The production process different from the detection process can lead to the different NSIs effects. However, if the processes are same on the level of quantum mechanics (not on the level of quantum field theory) the mixing matrices in Eq. (4.17) are related by:

$$M_{\alpha i}^s = M_{\alpha i}^{d*} \tag{4.31}$$

In this case, the oscillation probability changes, since the phase factor $\Delta\phi_{ij}$ is now zero. All oscillation effects start with same phase now. Nevertheless, the matrices can still be non-unitary and the zero-distance effect can still be present.

4.4 General Survival Probability to Use in Daya Bay

Formula in Eq.(4.25) has too many free parameters to constrain all of them at once in Daya Bay. Therefore, we have to reduce their number using reasonable assumptions. The mixing due to θ_{23} does not have any effect in $\bar{\nu}_e \to \bar{\nu}_e$ oscillations. Therefore it does not matter if we assume NSIs in this mixing sector or not. On the contrary, the mixing due to θ_{12} is present however its effect is suppressed due to small distances with the comparison of oscillation length of typical reactor antineutrinos due to Δm_{21}^2. Since we expect that NSIs effect will be small itself, any other suppression makes it negligible. Therefore we can assume there is no NSIs effect in the solar sector thus we keep mixing angle θ_{12} in place.

The only NSIs effect we consider is in the sector $ij = 13$ of the mixing matrix which can be then schematically expressed as:

$$M_{DB} = \begin{pmatrix} 1 & 0 & 0 \\ 0 & c_{23} & s_{23} \\ 0 & -s_{23} & c_{23} \end{pmatrix} \begin{pmatrix} \mathbf{A} & 0 & \mathbf{B} \\ 0 & 1 & 0 \\ \mathbf{C} & 0 & \mathbf{D} \end{pmatrix} \begin{pmatrix} c_{12} & s_{12} & 0 \\ -s_{12} & c_{12} & 0 \\ 0 & 0 & 1 \end{pmatrix} = \begin{pmatrix} c_{12}\mathbf{A} & s_{12}\mathbf{A} & \mathbf{B} \\ . & . & . \\ . & . & . \end{pmatrix} \tag{4.32}$$

where matrix mixing $ij = 13$ sector is no longer unitary, therefore we used $\mathbf{A}$,$\mathbf{B}$,$\mathbf{C}$,$\mathbf{D}$ to express general complex numbers. In Eq.(4.32), we have calculated relevant terms of the mixing matrix M_{DB} for Daya Bay's oscillation channel $\bar{\nu}_e \to \bar{\nu}_e$ which we can directly plug it in into the Eq.(4.25) taking into consideration that we have actually two mixing matrices, one for the source and one for the detector, marked with indexes s and d respectively. The survival probability is then:

$$\begin{aligned} P^{DB}_{\bar{\nu}_e \to \bar{\nu}_e} = \frac{1}{A^{s2} + B^{s2}} \frac{1}{A^{d2} + B^{d2}} \Bigg[& (A^s A^d + B^s B^d)^2 - \sin^2 2\theta_{12} (A^s A^d)^2 \sin^2 \frac{\Delta m^2_{21} L}{4E} \\ & - 4\cos^2\theta_{12} A^s A^d B^s B^d \sin^2 \left(\frac{\Delta m^2_{31} L}{4E} - \frac{\Delta\phi}{2} \right) \\ & - 4\sin^2\theta_{12} A^s A^d B^s B^d \sin^2 \left(\frac{\Delta m^2_{32} L}{4E} - \frac{\Delta\phi}{2} \right) \Bigg] \end{aligned} \tag{4.33}$$

where we used parametrization $\mathbf{A}^{s/d} \equiv A^{s/d} e^{i\phi_A^{s/d}}$, $\mathbf{B}^{s/d} \equiv B^{s/d} e^{i\phi_B^{s/d}}$ and introduce $\Delta\phi = (\phi^d_B - \phi^s_B) - (\phi^d_A - \phi^s_A)$. We can furthermore introduce

$$\begin{aligned} a &= \frac{A^s A^d}{\sqrt{(A^{s2} + B^{s2})(A^{d2} + B^{d2}))}} \\ b &= \frac{B^s B^d}{\sqrt{(A^{s2} + B^{s2})(A^{d2} + B^{d2}))}} \end{aligned} \tag{4.34}$$

and the probability takes the form of

$$\begin{aligned} P^{DB}_{\bar{\nu}_e \to \bar{\nu}_e} = (a+b)^2 & - \sin^2 2\theta_{12} a^2 \sin^2 \frac{\Delta m^2_{21} L}{4E} \\ & - 4\cos^2\theta_{12} ab \sin^2 \left(\frac{\Delta m^2_{31} L}{4E} - \frac{\Delta\phi}{2} \right) \\ & - 4\sin^2\theta_{12} ab \sin^2 \left(\frac{\Delta m^2_{32} L}{4E} - \frac{\Delta\phi}{2} \right) \end{aligned} \tag{4.35}$$

where $1 \geq a, b \geq 0$ and $a + b \leq 1$.

The general survival probability formula with NSIs effects in Eq.(4.35) is very similar in structure to the standard oscillation probability in Eq.(5.2). General NSIs probability can be actually reduced to the standard oscillation probability. First the mixing matrix has to be unitary which is briefly discussed in section Sec.4.3.1. Then the size of the matrix elements can be parametrized by mixing angles and it holds that

$$A^s = \cos\theta_{13}^s \qquad A^d = \cos\theta_{13}^d \tag{4.36}$$

$$B^s = \sin\theta_{13}^s \qquad B^d = \sin\theta_{13}^d \tag{4.37}$$

$$a = \cos\theta_{13}^s \cos\theta_{13}^d \tag{4.38}$$

$$b = \sin\theta_{13}^s \sin\theta_{13}^d \tag{4.39}$$

Second, the processes in the source and in the detector have to be the same what is discussed in section Sec.4.3.2. That means $\Delta\phi = 0$. Together with the first condition we get $\theta^s = \theta^d$. Plugging all these conditions in Eq.(4.35) we get the standard oscillation survival probability in three-neutrino framework.

4.5 Discussion about Approaches to Include the Effects of Non-standard Interactions

Both approaches of introduction of NSIs effects into the neutrino oscillations presented above are based on the effective Lagrangian of the physics Beyond Standard Model. They both use phenomenological description and their parameters are not exactly the parameters of the Lagrangian. Although, the common approach is widely used in the literature we prefer our formalism to be more illustrative at the end in the form of the survival probability formula. It is later used to quantify the possible effects in the NSIs in the antineutrino oscillations in Daya Bay.

5. The Daya Bay Experiment

5.1 Introduction of the Daya Bay Experiment

The Daya Bay experiment was designed for discovery of non-zero mixing angle θ_{13} using relative measurement of disappearance of nuclear reactor $\bar{\nu}_e$ in the functionally identical detectors placed in the underground experimental halls.

The Daya Bay experiment is using concept of near-far detector which was proposed by L. Mikaelyan and V. Sinev [13]. The detector placed close to the antineutrino source works as a benchmark measurement for the flux expected in the far detector. The relative near-far measurement does depend on the neutrino flux prediction. We can write:

$$\frac{N_f}{N_n} = \left(\frac{N_{p,f}}{N_{p,n}}\right)\left(\frac{L_n}{L_f}\right)^2\left(\frac{\varepsilon_f}{\varepsilon_n}\right)\left(\frac{P(E_\nu, L_f)}{P(E_\nu, L_n)}\right) \tag{5.1}$$

where the ratio of detected antineutrinos in the far to near detector $\frac{N_f}{N_n}$ depends only on the relative number of targets (protons) $\frac{N_{p,f}}{N_{p,n}}$ in detectors, distances ratio $\frac{L_n}{L_f}$ from the source, ratio of detection efficiencies $\frac{\varepsilon_f}{\varepsilon_n}$ and the survival probability $P(E_\nu, L)$ where index f stands for far detector and n stands for near detector. Since all variables enter as a relative ones only uncorrelated uncertainty matters. Having these uncertainties well known is essential for precise measurement.

The second major source of the uncertainties is the absolute detection efficiency. For Daya Bay, we already get rid of the part of the problem by introducing relative near-far measurement where basically only relative uncertainties matters. In order further suppress the relative detector uncertainties, Daya Bay uses eight functionally identical detectors where at least two are placed side-by-side in one experimental hall.

Besides the relative measurement, Daya Bay uses other advanced techniques and designs, which are described below. The Daya Bay precision led in 2012 to the first observation of non-zero mixing angle θ_{13} [9].

5.2 Principle of the θ_{13} Measurement by Reactor Antineutrino Disappearance in Short Baselines

Using Eq.(2.15) and Eq.(2.18) we can derive the oscillation probability $P_{\bar{\nu}_e \to \bar{\nu}_e}$ relevant for the Daya Bay experiment:

$$\begin{aligned} P_{\bar{\nu}_e \to \bar{\nu}_e} = 1 &- \sin^2 2\theta_{12} \sin^2 \frac{\Delta m^2_{21} L}{4E} \\ &- \sin^2 2\theta_{13} \left(\cos^2\theta_{12} \sin^2 \frac{\Delta m^2_{31} L}{4E} + \sin^2\theta_{12} \sin^2 \frac{\Delta m^2_{32} L}{4E}\right) \end{aligned} \tag{5.2}$$

For illustration the probability as function of distance is shown in Fig.5.1 for typical reactor antineutrino energy $E_\nu = 3.5$ MeV. The curve with $\sin^2 2\theta_{13} = 0$

shows the large amplitude medium baseline oscillation governed by the term proportional to $\sin^2 \frac{\Delta m^2_{21} L}{4E}$ in Eq.(5.2). For non-zero value of mixing angle θ_{13} we get additional oscillation on the top of those with the large amplitude, see Fig.5.1. These oscillations have shorter oscillation length since mass squared splitting $\Delta m^2_{32} \simeq \Delta m^2_{31}$ which governs them are 30-times larger than the mass square splitting Δm^2_{21}. We can clearly observe new local oscillation minimum in the short baseline ~2 km which dip is almost equal to the value of $\sin^2 2\theta_{13}$. Placing the detector to this ideal distance we will see the largest effect of the reactor antineutrino disappearance, which leads to the measurement of the mixing angle θ_{13}. In addition, we can determine parameter Δm^2_{32} (or Δm^2_{31}) linked to the oscillation frequency from the position of the oscillation minimum in the antineutrino energy spectrum.

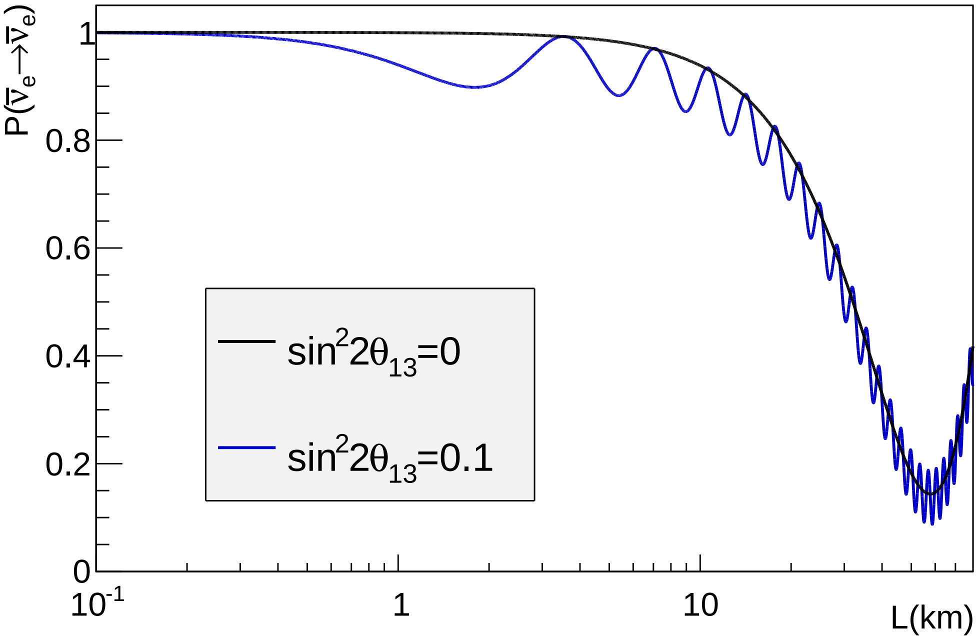

Figure 5.1: Oscillation probability $P(\bar{\nu}_e \rightarrow \bar{\nu}_e)$ as a function of distance for typical reactor antineutrino energy $E_\nu = 3.5$ MeV. The black curve with $\sin^2 2\theta_{13} = 0$ express the medium baseline oscillation governed by Δm^2_{21}. The blue curve with $\sin^2 2\theta_{13} = 0.1$ posses additional short baseline oscillations governed by $\Delta m^2_{32} \simeq \Delta m^2_{31}$. Daya Bay Far Hall detectors are placed in the distance ~2 km sitting right at the first short baseline oscillation minimum, where the amplitude of the dip is almost equal to the $\sin^2 2\theta_{13}$.

5.3 Overview of the Experimental Layout and Setup

The Daya Bay experimental site is located about 60 km from Hong Kong on the Chinese coast. The location was chosen due to the presence of powerful nuclear power plant complex. There are 3 pairs of functionally identical commercial pressurized water nuclear reactor cores, Daya Bay, Ling Ao and Ling Ao II, see Fig.5.2. Each core has 2.9 GW_{th} of thermal power which sums up to 17.4 GW_{th} in total [36].

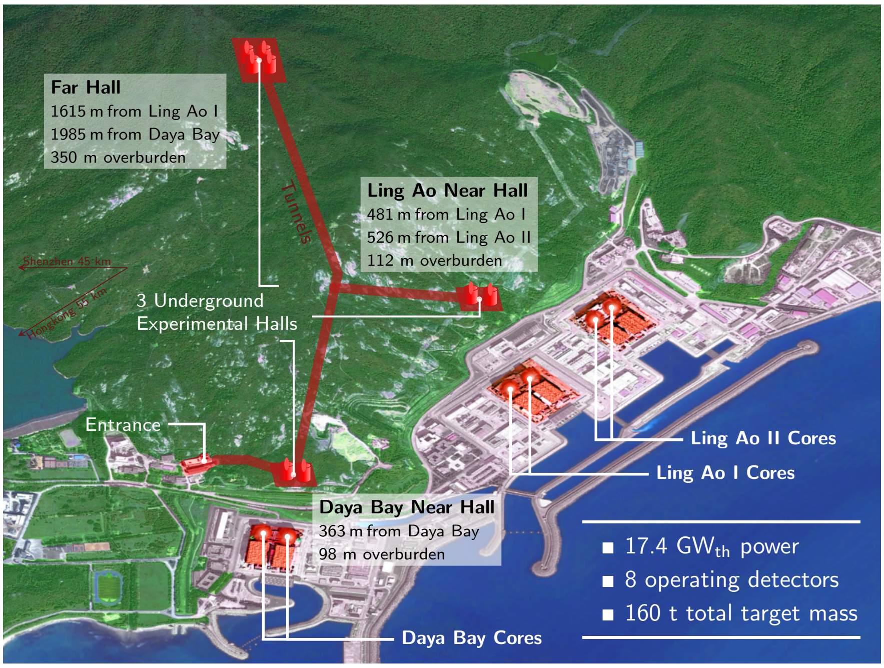

Figure 5.2: Layout of the Daya Bay experiment. There are 3 pairs of functionally identical comercial pressurized water nuclear reactor cores, Daya Bay, Ling Ao and Ling Ao II. There are 8 Antineutrino Detectors in the three underground experimental halls, Daya Bay Near Hall, Ling Ao Near Hall and Far Hall, connected with tunnels.

There are two underground near experimental halls one close to Daya Bay reactor cores, Daya Bay Near Hall, the other close to Ling Ao and Ling Ao II reactor cores, Ling Ao Near Hall. The Far Hall is located about 2 km far from reactors, see Fig.5.2.

Cosmic muons are main source of background for antineutrino detection. In order to be able to perform precise measurement it is necessary to have low-background experiment. Therefore detectors in Daya Bay are placed underground under adjacent mountains. The layer of rock provides few hundreds meters of water equivalent shielding, which results in the cosmic muon flux reduction. The overburden of each experimental hall is summarized in Tab.5.1.

	Experimental hall		
	Daya Bay Hall	Ling Ao Hall	Far Hall
Overburden [m (mwe)]	93 (250)	100 (265)	324 (860)

Table 5.1: Overburden of three Daya Bay underground experimental halls in meters and in meters of water equivalent [36].

There are two functionally identical Antineutrino Detectors (ADs) placed in

Detector	Reactors					
	D1	D2	L1	L2	L3	L4
AD1	362.38	371.76	903.47	817.16	1353.62	1265.32
AD2	357.94	368.41	903.35	816.90	1354.23	1265.89
AD3	1332.48	1358.15	467.57	489.58	557.58	499.21
AD8	1337.43	1362.88	472.97	495.35	558.71	501.07
AD4	1894.34	1533.18	1533.63	1551.38	1524.94	1524.94
AD5	1917.52	1891.98	1534.92	1535.03	1554.77	1528.05
AD6	1925.26	1899.86	1538.93	1539.47	1556.34	1530.08
AD7	1923.15	1897.51	1540.67	1540.87	1559.72	1533.18

Table 5.2: Distances in meters between reactor cores: Daya Bay cores (D1, D2) and Ling Ao and Ling Ao II cores (L1, L2, L3, L4) and Antineutrino Detectors placed in Daya Bay Near Hall (AD1, AD2), in Ling Ao Near Hall (AD3, AD8) and in Far Hall (AD4, AD5, AD6, AD7) [36].

each near hall and four ADs in the Far Hall. There are at least two detector modules at each hall for the comparison of the performance. This is key point for reduction of the uncorrelated uncertainties while the correlated uncertainties cancel out by the relative near-far measurement. Tab.5.2 summarizes distances between the reactors and the experimental halls.

In each hall, ADs are submerged in the pool of purified water. The layer of water provided at least 2.5 m thick shields from natural radioactivity from the surrounding rock. Moreover, the water pool is used as an active detector for cosmic muons. Muon passing through produces Čerenkov light which is subsequently collected in PMTs mounted on the walls and bottom of the pool. The information about passing muon is used in the data analysis for muon veto to improve signal to background ratio.

In order to identify muons more effectively the water pool, thus ADs, are covered by four layers of Resistive Plate Chamber detectors.

The muon tagging efficiency is practically 100% for muons passing through AD. The muon related background is suppressed well below 1% of background to signal ratio [36].

5.4 The Detection Method

In the Daya Bay experiment the detection of the reactor antineutrinos is performed by already several times mentioned inverse beta decay reaction (IBD):

$$\bar{\nu}_e + p \to e^+ + n \tag{5.3}$$

Antineutrinos interact with free protons in liquid scintillator producing positron and neutron. The antineutrino energy threshold for IBD is $E_{\bar{\nu}_e} = 1.804$ MeV. Both created particles are detected forming the coincidence between the so-called prompt and delayed signal. Prompt signal is given by the energy losses of positron and its following 2×0.511 MeV annihilation γ's. It happens practically immediately after the IBD reaction. The released energy can be directly linked to the initial antineutrino energy via formula:

$$E_\nu \simeq E_{prompt} + 0.78 \text{ MeV} \tag{5.4}$$

The neutron carries away only small amount of kinetic energy, 10-40 keV, which is neglected in Eq.(5.4).

The delayed signal is produced by the neutron capture mainly on the atoms of gadolinium, which are for this purpose added to the liquid scintillator. The liquid scintillator is loaded with 0.1% by weight of natural gadolinium. Natural gadolinium contains isotopes ^{155}Gd with 14.80% abundance and ^{157}Gd with 15.65% abundance. These isotopes have enormous cross-section for thermal neutron capture 60900 b, 254000 b respectively [66]. Such a large cross-section results in short neutron capture time that has positive impact on the reduction of accidental background. It takes in average ~30 μs for neutron to thermalize and being captured in the Daya Bay doped liquid scintillator with low gadolinium concentration of 0.1%. Another advantage of gadolinium is that new isotope created by neutron capture is in excited state and immediately release gamma cascade with total energy ~8 MeV. There is not basically any natural source of such a energetic events therefore neutron capture on gadolinium provides very clean signal. For the completeness, let us mention that neutron can be also captured by the atoms of hydrogen. Such events are also analyzed in the Daya Bay but our primary focus in this thesis is the sample of IBD events with neutron capture on gadolinium.

The cross-section for IBD reaction is increasing while the reactor antineutrino flux is dropping with the energy. Resulting detected unoscillated antineutrino energy spectrum is shown in Fig.5.3 for illustration. The detected spectrum starts at the IBD threshold 1.8 MeV, peaks around ~3.8 MeV and falls to very low rates above 8 MeV.

5.5 Antineutrino Detector

The Antineutrino Detector (AD) is a liquid scintillator detector. The energy deposited by physical events in the volume of the scintillator is converted to the scintillation light, which can be seen by Photomultiplier Tubes (PMTs) mounted on the walls of the AD. The combination of scintillation efficiency and PMT coverage results in detection of 168 photoelectron per MeV.

5.5.1 Antineutrino Detector Structure

The section through the AD is shown in Fig.5.4. AD is cylindrical stainless steel vessel 5 m high and 5 m in diameter. It is divided into three zones by two nested cylindrical acrylic vessels, Inner Acrylic Vessel (IAV) and Outer Acrylic Vessel (OAV).

The most inner zone, so-called GdLS region, is filled with organic liquid scintillator with total mass about 20 tons. Liquid scintillator is based on LAB, linear alkyl benzene, with additional wavelength shifters. Furthermore, the scintillator is doped by 0.1% by weight with natural gadolinium for the purposes we discussed in previous section.

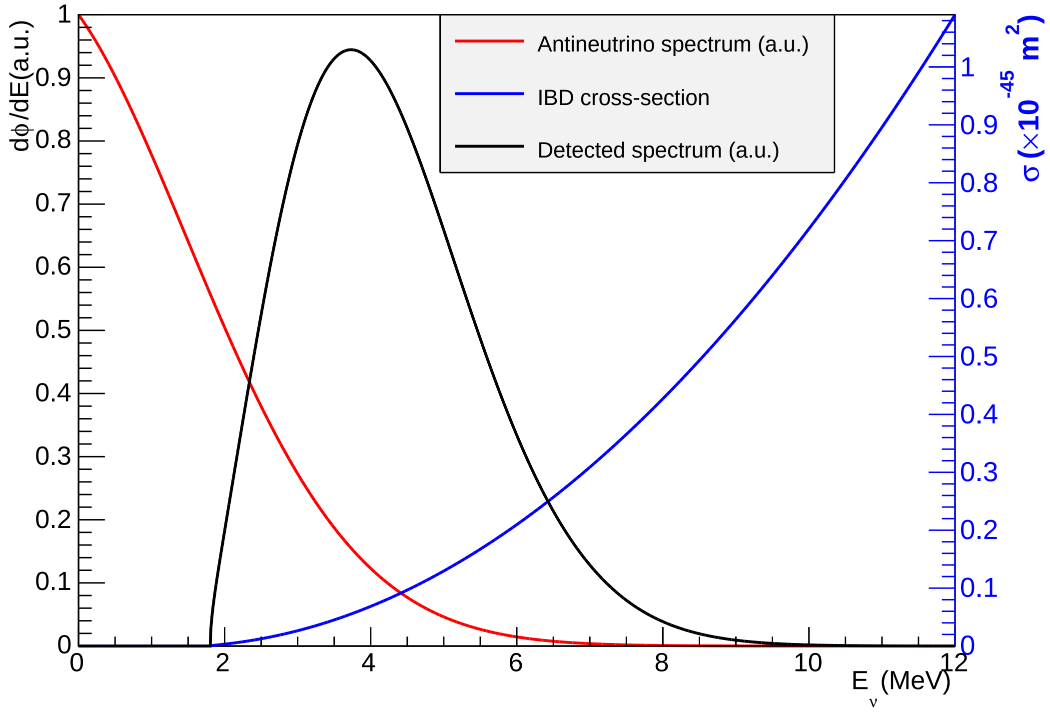

Figure 5.3: Inverse beta decay cross-section (blue), nuclear reactor antineutrino energy spectrum in arbitrary units (red) and resulting detected unoscillated antineutrino energy spectrum in arbitrary units (black). The detected spectrum spans from the IBD threshold 1.8 MeV up to more than 8 MeV where it vanishes.

The middle zone is so-called LS gamma catcher region. It is filled with 20 tons of the pure liquid scintillator. The main purpose of this region is to catch gammas escaping from the center of the detector and convert them into light visible for PMTs. More collected light improves the neutron detection efficiency and makes it more uniform through the GdLS target volume. In addition, it decreases the uncertainty in the detection efficiency. Also more converted gammas to the scintillation light results in better energy resolution, which is key point in the analysis of the antineutrino energy spectrum shape.

The most outer zone is buffer region filled with 37 tons of transparent low-scintillating mineral oil. There are 192 8-inch PMTs (Hamamatsu R5912) in total mounted on 8 stainless steel ladders. On each leader the PMTs are arranged in three columns with 8 PMTs per column. The main purpose of mineral oil buffer layer is to shield from natural radioactivity mostly from the PMT glass and stainless steel tank. Therefore the oil is low-scintillating just to absorb the radioactivity products, mostly gammas, but do not convert them to light visible by PMTs.

The acrylic vessels are made from UV-transparent acrylic. Their shape is cylindrical with the cone-shaped lid with 3 degrees tilt angle. There are three calibration pipes for lowering the calibration sources. The IAV has both height and diameter of 3.1 m and 10 mm thick walls. The OAV is 4 m in diameter and

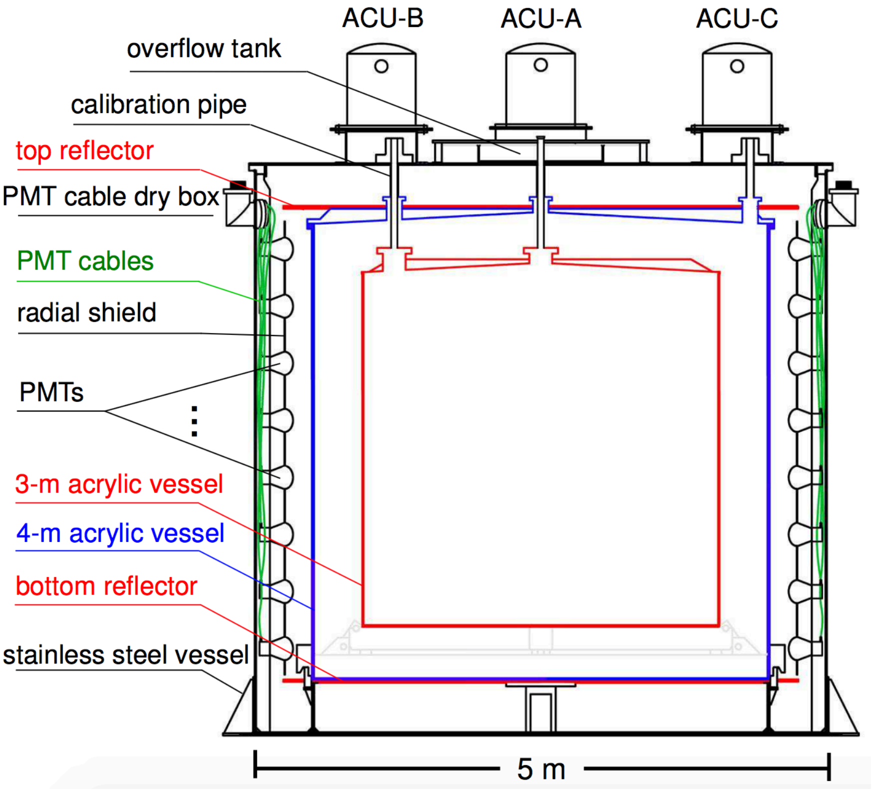

Figure 5.4: The section of the Antineutrino Detectors [67]. There are two acrylic vessels, Inner Acrylic Vessel and Outer Acrylic Vessel, separating the volume into three zones. There are 192 PMTs mounted on the walls if the stainless steel tank. There are two reflectors on the top and bottom to improve the light collection. On the top of AD, there are three ACUs, which contains system for deploying the radioactive calibration sources and LEDs inside the detector through three calibration pipes.

height. The walls are 18 mm thick.

In order to improve the light collection there are bottom and top reflectors mounted right outside of the OAV.

The IAV, OAV and ladders with PMTs are nested in the stainless steel tank 5 m in diameter and height with 12 mm thick walls. It provides the overall support for inside structures. The stainless steel does not have to be low-radioactive since the natural radioactivity mostly from U, Th, and K decays is shielded by mineral oil buffer zone.

5.5.2 The Calibration Instruments

For precision measurement, it is crucial to know accurately the energy response of AD. Therefore the special calibration system was developed.

Three Automated Calibration Units (ACUs) are mounted on the top of each AD, see Fig.5.4. They contain mechanism for deploying encapsulated radioactive sources and low intensity light-emitting diodes (LEDs) to the GdLS and LS region. The ACU-A is located on the central axis of AD, ACU-B lowers the capsule

Sources	Energy
^{241}Am-^{13}C neutron source	nH capture - 2.223 MeV nGd capture ~8 MeV
^{68}Ge positron source	2×0.511 aninihaliton gammas
^{60}Co gamma source	1.173 + 1.333 MeV gammas
LED	light for PMT gain

Table 5.3: List od sources mounted in each Automated Calibration Unit and corresponding released energy.

to the edge of GdLS region, 1.35 m from the center and ACU-C deploying the source 1.77 m from center into the LS region.

The ACUs are used for several purposes. LEDs are used for time calibration of the PMTs and for the calibration of the individual PMT gain. The radioactive sources are used primarily for the calibration of the absolute energy scale. Knowing the released energy and measuring the response of the detector in number of photoelectrons (PE) we can find the conversion factor PE-to-MeV. The sources are lowered to AD during special calibration runs on a weekly basis. Daya Bay also uses independent determination of the conversion factor based on the spallation neutrons. Spallation neutrons are emitted in the reactions of cosmic muons passing through the detector. They provides continuous source of calibration data distributed uniformly in AD volume.

The other use of the source is the study of detector non-uniform response and for special purposes e.g. study the spill-in and spill-out effect when neutron can drift in or out from the GdLS region during the process of thermalization. The list of the sources and appropriate released energy are shown in Tab.5.3.

The ACUs however introduce additional background for the IBD reaction, especially ^{241}Am-^{13}C neutron source, which is discussed in detail in the Sec.5.8. The impact is small for ADs located in the near halls, since the statistics from the reactor antineutrinos is high. However, it become important for ADs located in the Far Hall where the statistics from the reactor antineutrinos is limited due to distance factor. In order to reduce this backrgound, the ^{241}Am-^{13}C neutron sources were removed from ACU-B and ACU-C in all ADs in Far Hall during the 2012 summer shutdown.

5.6 Muon Tagging System

Cosmic muons induce the most important sources of background for the IBD reaction, see Sec.5.8. Daya Bay developed extensive muon tagging system, which provides the information about passing muons. This information can be later used offline in the analysis for the muon veto. The system consists of several independent detectors. The scheme is shown in Fig.5.5. AD itself can be used for the muon tagging. But not only muons passing directly though the AD can induce IBD background. Therefore the ADs are submerged in the water pool, which works as a passive shielding but more importantly as an active Čerenkov detector. In order to further improve information about passing muons the whole water pool is covered by the array of 4 layers of Resistive Plate Chambers (RPCs).

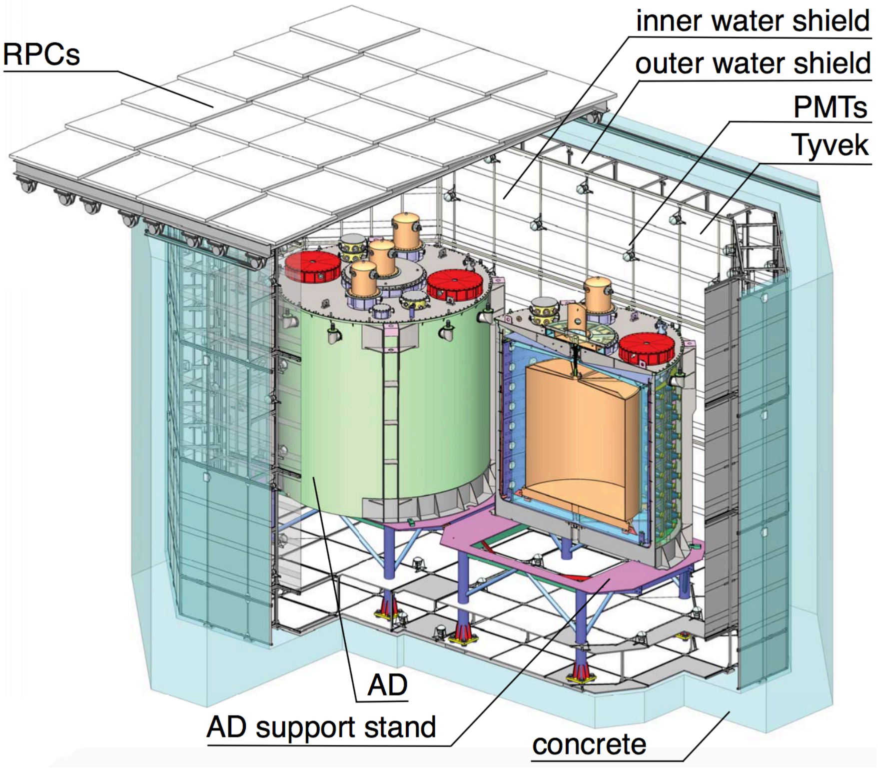

Figure 5.5: The scheme of Daya Bay muon tagging system, near hall as an example [67]. ADs in each hall are submerged into the water pool, which is optically separated to the two zones. Both of them are mounted with PMTs and work both as a passive shield and active muon Čerenkov light detector. Water pool is covered with array of RPC detectors providing additional information about passing muons.

5.6.1 Muons in Antineutrino Detector

Muons passing through the Daya Bay detectors lose its energy primarily by ionizitaion. The loss is roughly 2 MeV/cm at the ionization minimum in the liquid scintillator. Therefore muon passing through the whole AD deposits about 800 MeV energy. In minority of cases, the muon deposits large amount of energy, which is accompanied with higher number of released neutrons and production of unstable isotopes from the spallation of stable liquid scintillator atoms. These events are assumed to be muon-induced particle showers. The so-called AD showers are responsible for the production of particular radioactive isotopes ^{8}He and ^{9}Li, which are significant background for the IBD reactions, see Sec.5.8.

In our analysis, every event in AD with reconstructed energy $E > 20$ MeV is considered to be a muon. The higher energy is, the longer path muon traveled through AD. The lowest energy is for the clipping muon. There are not basically any other natural sources of such energetic events than muons.

ADs provide practically 100% efficiency for cosmic muons [36].

Halls	IWS	OWS (inward/outward)	Total
Daya Bay Hall	121	167 (103/64)	288
Ling Ao Hall	121	167 (103/64)	288
Far Hall	160	224 (128/96)	384

Table 5.4: The number of 8" PMTs instrumented in IWS and OWS in the three experimental halls. The PMTs in OWS are in addition divided into those facing towards the ADs (inward) and those facing from ADs (outward).

5.6.2 Water Pool

Not all muons are passing though AD. But still they can produce fast neutrons around AD, which can travel to the target volume and mimic IBD signal. Therefore, ADs are submerged in the water pool to shield these neutrons. In the near halls the size of water pool is 16 × 10 m and 10 m deep while in Far Hall the size is 16 × 16 m and depth is again 10 m. Water pool provides always at least 2.5 m layer of pure water for shielding from neutrons.

The water pool does not provide only passive shielding but it works also as an active water Čerenkov light detector. As an enhancement the water pool is optically separated around the walls and floor by Tyvek sheets into two zones Inner Water System (IWS) and Outer Water System (OWS). They work as two independent active systems to tag the muons. There are 8-inch PMTs mounted on the support structure in both IWS and OWS. The exact numbers of PMTs are summarized in Tab.5.4.

Using the muons tagged by AD we can estimate the muon detection efficiency of IWS to be basically 100% while the OWS provides itself ∼97.3% efficiency for the near halls and 98.7% efficiency in the Far Hall [36]. These values were confirmed by Monte Carlo simulation, which gives consistent results.

5.6.3 Resistive Plate Chamber Detectors

On the top of the water pool there is an array of four-layer Resistive Plate Chamber (RPC) detectors modules with size of 2 × 2 m.

Resistive Plate Chamber detector consist of layer of ionizable gas mixture in between two highly resistive bakelite plates, see Fig.5.6.3. The graphite layer is applied on the bakelite plates working as electrodes where high voltage of thousands of volts is applied. Passing muon ionizes the gas forming streamer. Limited charged is transported from one bakelite plate to the other. The resistive nature of the bakelite ensure the only small area of induced charge is depleted and the streamer stops automatically when it runs out of accumulated electrons. Transported charge induces due to its movement signal on the read-out copper electrodes. The advantage of such a setup is that the induced signal is large enough that it does not need to be amplified and can be directly processed by read-out electronics.

The signal electrode is not in one piece but it is divided into stripes with an width of 26 cm with additional structure providing spatial resolution ∼8 cm perpendicular to the stripes, see Fig.5.6.3. There are four layers of RPC detectors

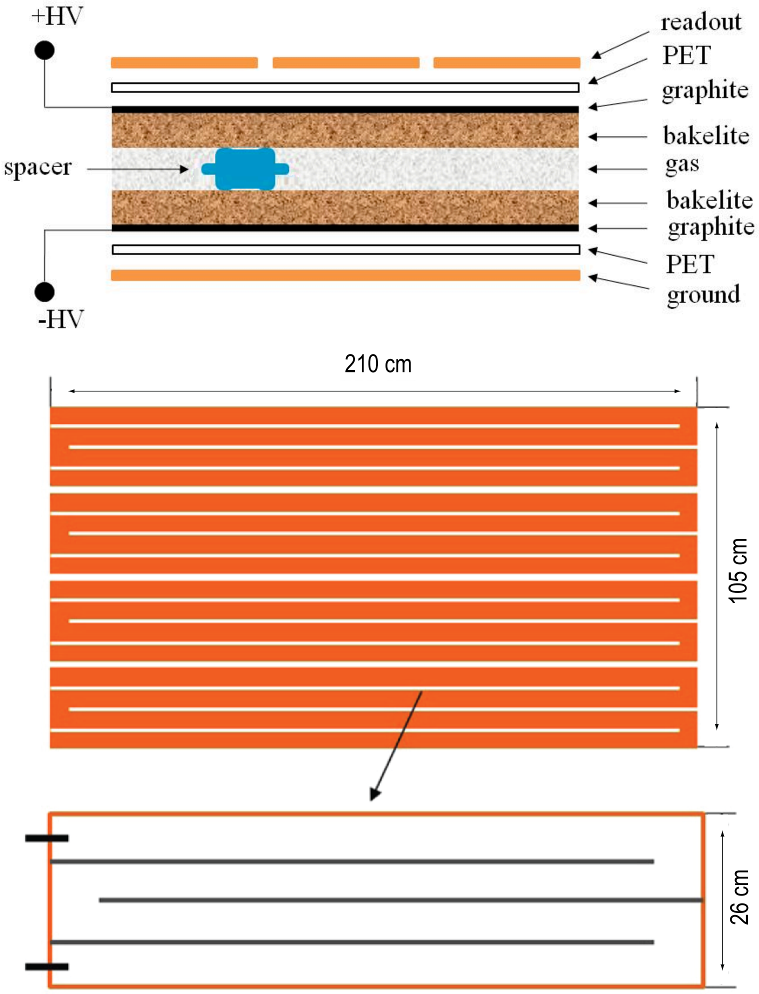

Figure 5.6: (Upper panel) The basic section through one RPC detector layer [68]. There are two bakelite plates separated with the layer filled with ionizable gas. The uniform space is ensured by spacers. There are graphite electrodes and copper read-out strips separated by plastic film. (Lower panel) The RPC readout pattern showing for illustration four of eight readout strips [68]. There is a zoom to the single readout strip showing its additional structure. The readout contacts are marked. The separation between readout strips is 0.25 cm. The folds of a single readout strip are 6.25 cm wide and separated by again 0.25 cm.

in one module. Combining stripes alignment along x-y axis we can get very precise spatial information about passing muon.

We should note that RPC detectors are not use for muon tagging in the process of inverse beta decay candidate selection presented in the next section.

5.7 Inverse Beta Decay Candidate Selection

Inverse beta decay reaction provides unique pattern of prompt and delayed signal. The cuts are designed in order to select such a coincidence. The cuts are summarized in Tab.5.5 and described in detail in what follows.

Name	Definition	Purpose
Flasher Cut	see below	Remove ligt emitted by PMTs
WP Muon Veto	Veto (-2,600) μs after NHIT> 12 in OWS or IWS	Reduce muon induce background
AD Muon Veto	Veto (0,1) ms after > 20 MeV signal	
AD Shower Muon Veto	Veto (0,1) s after > 2.5 GeV signal	
Multiplicity Cut	No signal > 0.7 MeV 200 μs before prompt No signal > 0.7 MeV 200 μs after delayed	Cleaner IBD signal
Prompt Energy Cut	$0.7\,\mathrm{MeV} < E_{prompt} < 12\,\mathrm{MeV}$	Prompt signal energy range
Delayed Energy Cut	$6\,\mathrm{MeV} < E_{prompt} < 12\,\mathrm{MeV}$	Delayed signal energy range
Time Cut	$1\,\mu\mathrm{s} < t_c < 200\,\mu\mathrm{s}$	Coincidence time

Table 5.5: Inverse Beta Decay Candidate Selection Cuts (Selection A in [36]).

Here is a simple explanation of the individual cuts and their motivation:

- **Flasher cut:** The Flasher Cut is introduced in order to reject events when light was spontaneously emitted by PMT bases. The events has specific pattern in the PMT hits, which is used for their identification, for more details see [36].

- **Prompt energy cut:** The energy range for the prompt signal is selected based on the shape of the predicted IBD positron spectrum. It goes from threshold energy 1.022 MeV up to 12 MeV where the rate of IBD events is negligible.

- **Delayed energy cut:** The energy range for the delayed signal is chosen to contain 8 MeV peak from neutron capture on gadolinium. The lower bound is set to 6 MeV, which is above natural radioactivity background hence we get clean signal. Nevertheless, part of the gammas from the 8 MeV gamma cascade is not stopped in liquid scintillator and converted to the scintillation light. They escape from the detector, which results in lower reconstructed energy. Therefore delayed energy cut results in about 93% detection efficiency.

- **AD shower muon veto:** The events reconstructed in AD with energy $E > 2.5$ GeV are considered to be particle showers induced by passing muon. They are likely to produce relatively long-lived unstable isotopes, which can mimic the IBD signal. Therefore we introduce 1 second veto for the delayed signal after these events.

- **AD muon veto:** The events reconstructed in AD with energy in the interval of 2.5 GeV $> E >$ 20 MeV are considered to be muons which does not produce particle showers but they can still kick out neutron from nuclei of the surrounding matter. These neutrons can be captured on gadolinium and together with the natural radioactivity events falling into the prompt energy window mimic the IBD signal. In order to reduce this background, 1 ms veto after the muon for the delayed signal was chosen. Since the average time of the neutron capture is $\sim$30 μs, the probability of muon-induced neutron to survive this time without being captured is negligible.

- **Water Pool muon veto:** The muons which does not pass directly through the AD can still produce neutrons which can travel all the way to the detector and introduce the background for IBD events. Therefore 600 μs veto is used after IWS or OWS tagged muon for the delayed signal. The event is labeled as muon in the IWS or OWS when the number of hit PMTs in one of the sub-detectors is higher than 12.

- **Multiplicity cut:** In order to select clean IBD signal we do not want any other event happen near the coincidence of prompt and delayed signal. Therefore we demand no other signal with $E > 0.7$ MeV to be 200 μs before prompt and after delayed signal.
- **Time coincidence:** It takes ~30 μs for neutron to thermalize and capture on gadolinium. Therefore appropriate coincidence time from 1 μs to 200 μs was chosen. The lower bound is due to the dead time after trigger.

The energy distribution of pairs of prompt and delayed signal within time window $(1, 200)$ μs after multiplicity cut and muon veto is shown Fig.5.7. Furthermore, the energy region of prompt and delayed signal for neutron capture on gadolinium is marked. In this region, we can see the contamination from the various backgrounds, e.g. delayed events above 8.5 MeV within the marked area. The background estimation is discussed in the next section.

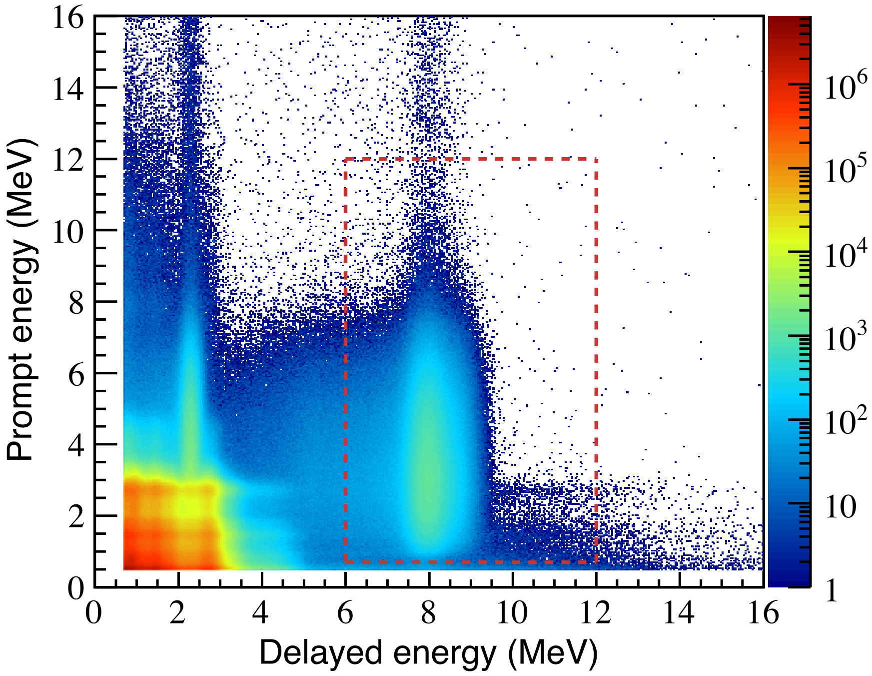

Figure 5.7: The distribution of prompt and delayed signal energy within time window $(1, 200)\,\mu$s after multiplicity cut and muon veto [36]. The red dashed line marked the energy cuts used for the selection of neutron capture on gadolinium as it is listed on in Tab.5.5.

The selection cuts as well as other phenomena introduce IBD efficiency and related uncertainty. The efficiencies for the IBD selection with neutron capture on gadolinium for single AD are summarized in Tab.5.6.

Let us go through other phenomena, which contribute to the IBD detection efficiency or/and to its uncertainty. The first example is the number of target protons in the liquid scintillator. We have an uncertainty on the total mass of the liquid scintillator and also on the content of hydrogen in it. Most of these uncertainties are correlated among ADs.

There is an efficiency related to the fraction of the captures on gadolinium. As we have mentioned before, neutron can capture instead on gadolinium on the other elements in the liquid scintillator. Therefore, the IBD events take place in the GdLS region end up with neutron captured on gadolinium in only ~84% cases while the rest results in the capture on hydrogen or other elements.

The number of detected IBD events with neutron capture on gadolinium is improved by so-called spill-in effect. Actually, it is the combination of the spill-in and spill-out of the neutron to or from the GdLS region during the process of thermalization. Effectively, we get higher target mass than mere GdLS mass what is expressed in Tab.5.6 as the efficiency being higher than 100%. The spill-in and spill-out effect is determined by Monte Carlo simulations and confirmed by measurement of the neutron sources from ACU-B and ACU-C.

There is livetime calculation, which has negligible but non-zero uncertainty.

Taking into consideration all of these effects, the overall detection efficiency is 80.6% with uncorrelated uncertainty of 0.13% among ADs.

	Efficiency	Correlated	Uncorrelated
Target protons	-	0.92%	0.03%
Flasher Cut	99.98%	0.01%	0.01%
Prompt Energy Cut	99.8%	0.10%	0.01%
Delayed Energy Cut	92.7%	0.97%	0.08%
Multiplicity Cut	-	0.02%	0.01%
Coincidence Time Cut	98.7%	0.12%	0.01%
Gd Capture Fraction	84.2%	0.95%	0.10%
Spill-in	104.9%	1.00%	0.02%
Livetime	-	0.002%	0.01%
Combined	80.6%	1.93%	0.13%

Table 5.6: Efficiencies for the IBD selection with neutron capture on gadolinium and their correlated and uncorrelated uncertainties among ADs [36]. We remind that for the relative near-far measurement performed by Daya Bay only uncorrelated uncertainties matter.

5.8 Backgrounds

The Daya Bay experiment was designed and constructed as low-background experiment. As we discussed previously, various features were employed to suppress different kinds of background. Of course, it is impossible to get rid of it completely. Let us present the major sources of background and how do we estimate it.

In general, the background events should exhibit similar properties as IBD events in order to pass energy cuts and the coincidence time cut. Such backgrounds can be divided into two major groups. The first group is uncorrelated background where two independent events happen to pass the selection cut. The second group is the correlated background where prompt and delayed signal have origin in the same physical process as it is in IBD. The main sources are fast neutrons and decays of unstable isotopes produced in spallation by cosmic muons. There is also an α-n natural radioactivity background. Finally there is an correlated background we introduced ourselves which is related to the ^{241}Am-^{13}C calibration source mounted in ACUs.

The proper estimate of these backgrounds and their following subtraction is key for precise measurement of neutrino oscillation parameters.

5.8.1 Accidental Background

The accidentals are two uncorrelated signals, which happen to pass the IBD selection criteria listed in Tab.5.5. For the prompt energy there are plenty of natural radioactivity events especially in the low energy region. The lower bound of delayed energy cut is high enough that the natural radioactivity spectrum is practically zero. Therefore the singles rate passing delayed energy cut from 6 MeV up to 12 MeV is very suppressed compare to the prompt-like singles. The delayed-like singles are mainly caused by neutrons from surrounding rock which travel all the way to the AD and capture on gadolinium. These neutrons are produced by muons, which are not tagged by the Muon Tagging System.

The accidentals have the biggest absolute contribution to the overall background. Nevertheless, we know it with very high precision resulting in a small uncertainty. The estimation of its rate is based on the measurement of isolated single prompt-like and delayed-like signals and combining them into the IBD-like events.

5.8.2 Fast Neutron Background

Fast neutrons are produced by cosmic muons passing through the detector and most importantly through surrounding rock. We can veto against those caused by tagged muons. Unlike in the case of accidental background, fast neutron can itself produce correlated signal with IBD signature. Neutron with high energy can elastically scatter on the protons in the liquid scintillator producing prompt-like signal. That is correlated with the following thermalized neutron captured on gadolinium produced delayed signal.

The energy spectrum of recoiled protons ranges from small energies up to few hundreds of MeV. Therefore if we loose the prompt energy cut to $0.7\,\text{MeV} < E_{prompt} < 100\,\text{MeV}$ we observe rather flat fast neutron prompt energy spectrum above the real IBD events. The fast neutron background can be estimated by extrapolating the distribution from 12 MeV to 100 MeV down to 0.7 MeV.

5.8.3 ^{9}Li/^{8}He Background

Another correlated background induced also by cosmic muons is production of unstable long-lived spallation isotopes. The most relevant isotopes are ^{9}Li and

^{8}He. They decay via beta decay sometimes emitting daughter neutron

$$\begin{aligned} {}^9Li &\rightarrow {}^8Be + e^- + n \quad \text{(BR 50.8\%)} \\ {}^8He &\rightarrow {}^7Li + e^- + n \quad \text{(BR 16\%)} \end{aligned} \tag{5.5}$$

Energy loss by electron and subsequent neutron capture on gadolinium can mimic IBD signal. The main problem of these isotopes is that they have quite long lifetime. The half-life of ^{9}Li is 178.3 ms and for ^{8}He it is 118.5 ms. If we would like to veto against all of their decays we would have to have long shower muon veto. Production of the isotopes is accompanied with the particle shower with high reconstructed energy. These events have a low rate. However, long veto time would lead to the significant increase of the dead time and results in lower IBD statistics.

Because of the large Q-values ($Q_{^9Li} = 13.6$ MeV, $Q_{^8He} = 10.7$ MeV [69]), the prompt signal produced in the ^{9}Li or ^{8}He decays by electron energy losses spans the whole IBD prompt signal spectrum.

The estimation is based on the study of time distribution of IBD-like events after AD tagged muons where we can identify exponential dependence corresponding to the half-life of these isotopes. Fitting the distribution we can estimate how many ^{9}Li/^{8}He decay events will happen outside the vetoed time. Although the showering muons with reconstructed energy $E > 2.5$ GeV are likely to produce these isotopes, ^{9}Li and ^{8}He can also be created by muons which deposit lower energy. The probability of a reaction is lower but this is vastly compensated by muon rate. Muon sample for the estimation was divided into several bins as a function of muon deposit energy. For showering muons with energy $E > 2.5$ GeV every muon was included. For non-showering muons with $E < 2.5$ GeV only those with accompanied neutrons were included since it was assumed that production of cosmogenic isotopes is very likely to be accompanied by release of neutrons. Then the production rate was corrected for the efficiency of this cut.

This background has the largest uncertainty among all the sources.

5.8.4 α-n Background

α-n correlated background is dominated by the process ^{13}C(α,n)^{16}O. The alphas are coming from the natural radioactivity in the liquid scintillator while the ^{13}C is natural isotope of carbon presented in the organic liquid scintillator. Neutron from such a reaction can be released with quite a energy when the oxygen is produced in the ground state. In this case the prompt signal comes from recoiled proton from the neutron thermalization process. If the oxygen is produced in the excited state the neutron have rather small energy. However, O* de-excitation γ mimics a prompt signal. In both cases, neutron is eventually captured on gadolinium producing delayed signal. The ^{13}C(α,n)^{16}O background was estimated from the measurement of alpha decays and then the neutron yield was determined by Monte Carlo.

The alphas are produced in ^{238}U,^{232}Th, ^{227}Ac decay chains and in decays of ^{210}Po. For estimating the rate of alphas from decay chains we use correlated signals from decay cascade. We use following cascades for ^{238}U,^{232}Th, ^{227}Ac respectively:

$$\begin{array}{lll} {}^{214}Bi \rightarrow {}^{214}Po + \beta & {}^{214}Po \rightarrow {}^{210}\ Pb + \alpha & \tau_{1/2} = 164.3\,\mu\text{s} \\ {}^{212}Bi \rightarrow {}^{212}Po + \beta & {}^{212}Po \rightarrow {}^{208}\ Pb + \alpha & \tau_{1/2} = 0.299\,\mu\text{s} \\ {}^{219}Rn \rightarrow {}^{215}Po + \alpha & {}^{215}Po \rightarrow {}^{211}\ Pb + \alpha & \tau_{1/2} = 1.781\,\text{ms} \end{array} \quad (5.6)$$

We assume that the whole chains are in equilibrium so we are able to calculate the total alpha production for all alpha decays within the chain. The ^{210}Po is a product of decay chain of ^{222}Rn presented in the air. We estimate the alpha production from special runs with the threshold lowered 0.7 MeV → 0.3 MeV. This is done due to the strong quenching effect for alphas in the liquid scintillator when e.g. alpha from ^{210}Po decay with energy 5.3 MeV is reconstructed as only about ∼0.5 MeV event.

5.8.5 ^{241}Am-^{13}C Calibration Source Background

The low-intensity ^{241}Am-^{13}C neutron calibration sources located in ACUs are primarily used for weekly energy calibration of the detector. Meanwhile, they are stored in stainless steel box mounted in the top of AD. The neutrons emitted by the source can scatter inelastically on the nuclei of Cr, Fe, Mn and Ni before being captured on the nucleus on the stainless steal or in the GdLS overflown tank on the top of AD. Both processes, inelastic scattering and subsequent neutron capture, are emitting gammas which occasionally pass through the shield to the liquid scintillator and mimic IBD signal. The gammas from the neutron capture have an energy high enough to fall to the delayed signal energy window.

The estimation of the background is based on the MC simulation benchmarked by the measurement with high-intensity source. Then the Monte Carlo is normalized to the events from the data taken with the regular low-intensity source in the ACUs. The Monte Carlo normalization is the larges source of the 45% uncertainty for this background. The rate was found negligible compare to the IBD rate in the near halls, however significant in the Far Hall. In order to reduce the impact of this background, the ^{241}Am-^{13}C neutron sources were removed in summer 2012 from ACU-B and ACU-C in the Far Hall ADs, while ACU-A source was kept for the calibration purposes. That led to the factor of ∼3 reduction of this background in the Far Hall.

5.9 Data Set For the Analysis

The Daya Bay experiment started data taking in December 2011 with six ADs. There were two ADs in the Daya Bay Near Hall, one AD in the Ling Ao Near Hall and 3 ADs in the Far Hall. This configuration last till July 2012 and brought the first measurement of non-zero value of mixing angle θ_{13} [9]. We refer to this period as 6AD period with 217 days of data. In summer 2012, two additional ADs were installed and special calibration campaign was performed. After restart of data taking in October 2012, Daya Bay is running with full configuration of 8ADs.

The Daya Bay most recent analysis is based on the 217 days of 6AD period and 1013 days of 8AD period [36]. However, in this thesis we have tested the

Lorentz Invariance and search for effects of the Non-standard Interactions in the sub set of 217 days of 6AD data and 404 days of data with 8ADs collected from October 2012 till November 2013 [59]. The number of IBD candidates, which pass the selection cuts for these in total 621 days of the data as well as the background rates and multiplicity and muon veto efficiency are shown in Tab.5.7. The background rates for fast neutrons and ^{9}Li/^{8}He background are assumed to be same for ADs placed within the experimental hall.

In the table, we can identify several points, which are results of the 2012 summer shutdown. First we can notice shorter data acquisition (DAQ) live time for AD7 and AD8. Those are the two ADs, which were installed during the break to complete the original Daya Bay design. We can also notice the drop in the ^{241}Am-^{13}C background rates for ADs in Far Hall due to the removal of the two out of three neutron source from ACUs.

Regarding the backgrounds and their uncertainties, we can see that the largest absolute contribution comes from accidentals but with negligible uncertainty. The largest source of the uncertainty is introduced by decays of isotopes ^{9}Li and ^{8}He. There was an intensive analysis campaign within Daya Bay for the most recent publish result [36] which led to the improved method of ^{9}Li/^{8}He background estimation and uncertainty reduction.

	Daya Bay Near Hall		Ling Ao Near Hall		Far Hall			
	AD1	AD2	AD3	AD8	AD4	AD5	AD6	AD7
IBD candidates	304459	309354	287098	190046	40956	41203	40677	27419
DAQ live time(days)	565.436	565.436	568.03	378.407	562.451	562.451	562.451	372.685
ε_μ	0.8248	0.8218	0.8575	0.8577	0.9811	0.9811	0.9808	0.9811
ε_m	0.9744	0.9748	0.9758	0.9756	0.9756	0.9754	0.9751	0.9758
Accidentals(per day)	8.92 ± 0.09	8.94 ± 0.09	6.76 ± 0.07	6.86 ± 0.07	1.70 ± 0.02	1.59 ± 0.02	1.57 ± 0.02	1.26 ± 0.01
Fast neutron(per AD per day)	0.78 ± 0.12		0.54 ± 0.19		0.05 ± 0.01			
9Li/8He(per AD per day)	2.8 ± 1.5		1.7 ± 0.9		0.27 ± 0.14			
Am-C 6-AD(per day)	0.27 ± 0.12	0.25 ± 0.11	0.27 ± 0.12	-	0.22 ± 0.10	0.21 ± 0.10	0.21 ± 0.09	-
Am-C 8-AD(per day)	0.20 ± 0.09	0.21 ± 0.10	0.18 ± 0.08	0.22 ± 0.10	0.06 ± 0.03	0.04 ± 0.02	0.04 ± 0.02	0.07 ± 0.03
13C(a, n)16O(per day)	0.08 ± 0.04	0.07 ± 0.04	0.05 ± 0.03	0.07 ± 0.04	0.05 ± 0.03	0.05 ± 0.03	0.05 ± 0.03	0.05 ± 0.03
IBD rate(per day)	657.18 ± 1.94	670.14 ± 1.95	594.78 ± 1.46	590.81 ± 1.66	73.90 ± 0.41	74.49 ± 0.41	73.58 ± 0.40	75.15 0.49

Table 5.7: Summary of the signal and backgrounds for 621 days of Daya Bay data. Rates per day were corrected for the multiplicity and muon veto efficiency $\varepsilon_m \times \varepsilon_\mu$ [59].

6. Analysis Methods

Our goal is to obtain the oscillation parameters as well as the additional Lorentz Invariance violation (LIV) or Non-standard Interactions (NSIs) parameters from the Daya Bay data. For the analysis, we use the modified tool for relative near-far measurement developed by the team from Lawrence Berkeley National Laboratory. The basic idea is to compare the measurement in the Far Hall with the prediction based on the energy spectra measured in the near halls. There are several nice features about this approach. The major fact is that this is completely relative measurement, where all of the correlated uncertainties cancel out. The analysis is largely independent on the reactor antineutrino spectrum shape and absolute flux prediction, the major sources of the uncertainty for the previous experiments. In addition, all other correlated uncertainties cancel out and only relative uncertainties have an impact to the measurement.

The parameter fitting is done in the unique way using the covariance matrix approach. All the variations due to the statistical and systematical uncertainties are encapsulated into one covariance matrix, which automatically encounter for the correlation among them. All of these variations are modelled by toy Monte Carlo (toyMC), which is independent on the fitting code. Covariance matrix approach does not require any nuisance parameters therefore fitting is done only for the parameters of our interest, standard oscillation parameters plus additional new physics parameters based on our particular search.

The whole procedure of prediction and fitting is encapsulated in the code named LBNL Fitter, which was originally created for the neutrino oscillation analysis in the three-neutrino framework. We extended it to be able to fit additional parameters for our searches. Let us now present key features of the LBNL Fitter [70], [71].

6.1 The LBNL Fitter

In the previous sections, we already discussed the IBD selection and background estimation. The values to feed into our fitter are summarized in Tab.5.7. We use the values for the near halls for the prediction of the spectra in the Far Hall.

6.1.1 Prediction of the Far Hall Spectrum from the Near Hall Measurements

The simple scheme how do we predict Far Hall spectrum based on the near hall measurements is shown in Fig.6.1. The procedure starts with getting the near hall prompt energy spectra with subtracted background and corrected for the efficiencies based on the data. The prompt energy spectrum in each hall is divided into 37 energy bins.

Each energy bin in this spectrum is converted from the visible energy E_{vis} measured by the detector to the true energy of the physical event E_{true}. For this conversion we use E_{vis}-to-E_{true} matrix, which takes into account detector response, non-linearity of the scintillator etc. The matrix is modelled by toyMC. This conversion is introduced only temporary and it is undone in the final stage at the prediction process. Therefore in the first order, the use of the conversion matrix does not introduce any source of a systematic bias.

Next step is to divide the measured energy spectrum into the contributions from each single reactor. For each energy bin of the true energy spectrum for AD i we calculate the flux fraction $f_{ij}(E_{true})$, which express the fraction of the bin content originated from the reactor core j. The flux fraction is defined as:

$$f_{ij}(E_{true}) = \frac{\phi_{ij}(E_{true}) \times P_{ij}^{osc}(E_{true}) \times 1/L_{ij}^2}{\sum_k \phi_{ik}(E_{true}) \times P_{ik}^{osc}(E_{true}) \times 1/L_{ik}^2} \tag{6.1}$$

where P_{ij}^{osc} is the oscillation probability, L_{ij} is distance of the rector j and detector i based on the Tab.5.2 and $\phi_{ij}(E_{true})$ is the expected antineutrino flux in AD i produced by reactor core j. The flux is calculated as a sum of the fluxes from four main isotopes producing reactor antineutrinos ^{235}U, ^{238}U, ^{239}Pu, ^{241}Pu based on the thermal power of the reactor provided by the power plant company and corrected for the burn-up.

The flux fraction $f_{ij}(E_{true})$ is used to calculate number of events in each true energy bin in AD i originating from reactor core j simply as

$$N_{ij}(E_{true}) = f_{ij}(E_{true}) \times N_i^{IBD}(E_{true}) \tag{6.2}$$

where $N_i^{IBD}(E_{true})$ is the number of events in the true energy bin which was background subtracted and efficiency corrected.

We can use the information about contribution from a particular reactor to get the prediction by extrapolating the near hall measurement to the Far Hall. Since the flux in each Far Hall AD can be predicted by each AD in the near halls, we can introduce extrapolation factor $e_{kj,i}(E_{true})$ which is used to predict the contribution of reactor core j in the Far Hall AD k based on the near hall AD i. The factor is defined as:

$$e_{kj,i}(E_{true}) = \frac{\phi_{kj}(E_{true}) \times P_{kj}^{osc}(E_{true}) \times 1/L_{kj}^2}{\phi_{ij}(E_{true}) \times P_{ij}^{osc}(E_{true}) \times 1/L_{ij}^2} \tag{6.3}$$

The number of predicted events $F_{kj,i}(E_{true})$ for each energy bin in Far Hall AD j based on the observation in near hall AD i originating from reactor core j is

$$F_{kj,i}(E_{true}) = e_{kj,i}(E_{true}) \times N_{ij}(E_{true}) \tag{6.4}$$

The following step is to sum over the contributions from all cores in order to get the total predicted spectra:

$$F_{k,i}(E_{true}) = \sum_j F_{kj,i}(E_{true}) \tag{6.5}$$

This way we obtain the predicted Far Hall spectra as a function of E_{true}. The last step is to translate the spectra back to the energy visible by the detector E_{vis} using the E_{vis}-to-E_{true} conversion matrix. Such a quantity $F_{k,i}(E_{vis})$ can be then compared with the actual measurement of the Far Hall spectra.

We should note that the procedure leads to 9 values of prediction $F_{k,i}$ for the 6AD period where we had three ADs in the near halls (i=1,2,3) and three ADs in the Far Hall (k =1,2,3) and 16 values of prediction $F_{k,i}$ for period running with full configuration of 8 ADs.

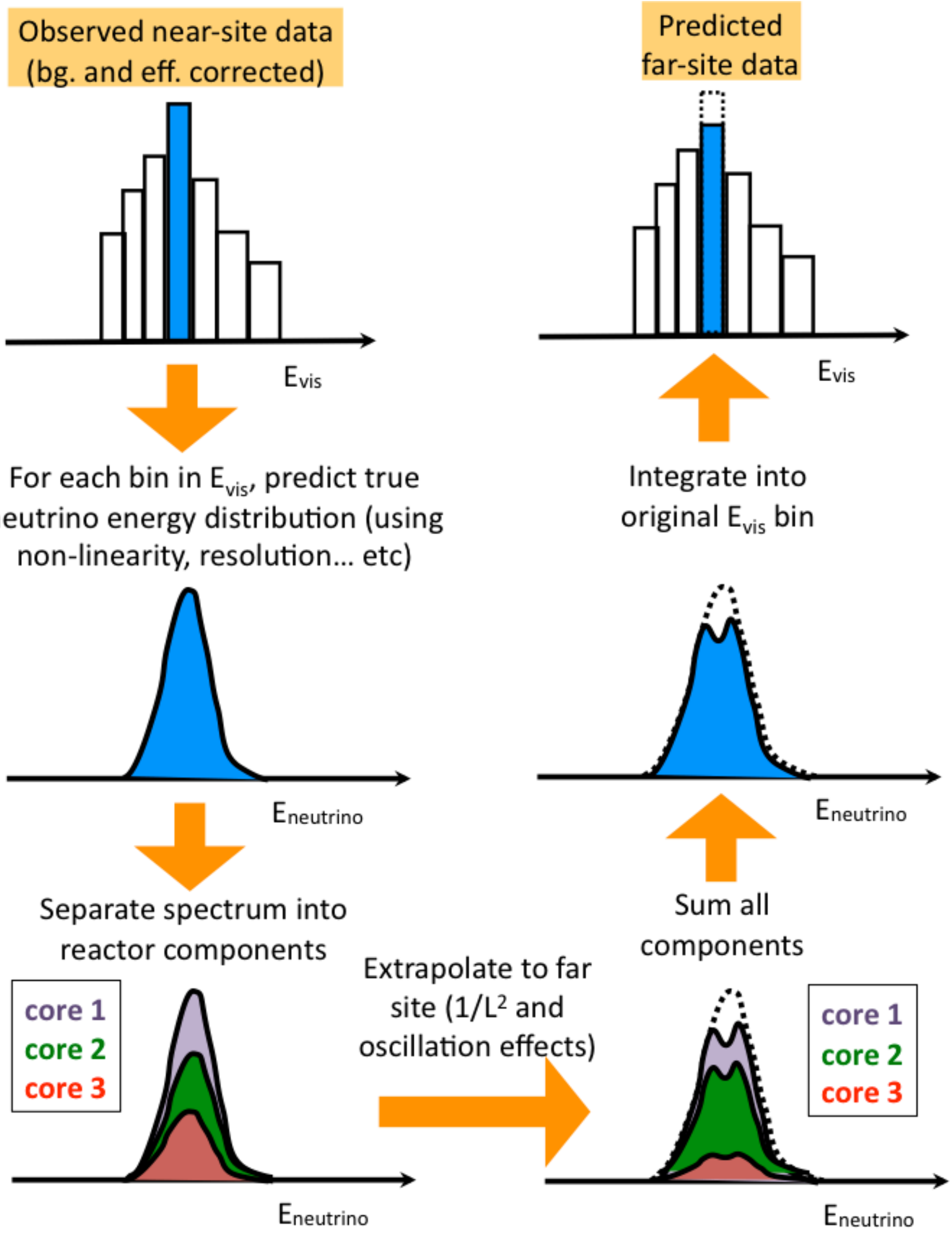

Figure 6.1: The scheme of steps leading from the near site measurement to the far site prediction [70]. For more details, see the text.

6.1.2 χ^2 Definition

As soon as we have the prediction for the Far Hall, we can compare it with the actual Daya Bay measurement. Note that the prediction is the function of the oscillation parameters θ_{13}, Δm^2_{ee} and additional LIV or NSIs parameters. The best-fit parameters are found by minimization of χ^2 which is defined as:

$$\chi^2 = \sum_{i,j,p,q}^{bins} \left[F^{obs}_{i,p} - F^{pred}_{i,p}(\theta_{13}, \Delta m^2_{ee}, ...)\right] V^{-1}_{ij,pq} \left[F^{obs}_{j,q} - F^{pred}_{j,q}(\theta_{13}, \Delta m^2_{ee}, ...)\right] \quad (6.6)$$

where $F^{obs}_{i,p}$ and $F^{pred}_{i,p}$ are the observed respectively predicted number of events after background subtraction in the i-th energy bin in the Far Hall ADs for the p-th period (6AD,8AD). Let us notice the $F^{pred}_{i,p}(\theta_{13}, \Delta m^2_{ee}, ...)$ is a function of the oscillation and additional new physics parameters however still based on near hall data. The V_{ij} is the covariance matrix, which contains all statistical and systematical uncertainties. This means that we do not have to use any nuisance parameters therefore χ^2 minimization is very simple and fast.

6.1.3 Covariance Matrix

The overall covariance matrix is composed of four parts:

$$V = V_{sys} + V_{bkg} + V_{stat} + V_{\Delta m^2} \tag{6.7}$$

where the V_{sys}, V_{bkg}, V_{stat} represent respectively the systematic uncertainty of the IBD signal, systematic uncertainty of the background and the statistical uncertainty. The additional $V_{\Delta m^2}$ represents the uncertainty related to the fixing of m^2_{ee} for some cases of our analysis, what is discussed in detail later in this chapter. The V_{sys}, V_{bkg}, $V_{\Delta m^2}$ are determined by toyMC. The V_{stat} is calculated analytically.

The values of V_{sys} elements depend on the oscillation parameters. We assume that their sizes are scaled with the size of the signal, which varies with oscillation parameters. We first calculate the covariance matrix V^{norm}_{sys}, which express the relative size of the systematic uncertainties. The V^{norm}_{sys} is calculated using nominal parameters based on the 1000 toyMC samples with systematical fluctuation as:

$$(V^{norm}_{sys})_{ij,pq} = \frac{1}{M} \sum^{toys} \frac{\left(F^{obs,toy}_{i,p} - F^{pred,toy}_{i,p}\right)\left(F^{obs,toy}_{j,q} - F^{pred,toy}_{j,q}\right)}{F^{pred,toy}_{i,p} \times F^{pred,toy}_{j,q}} \tag{6.8}$$

where $M = 1000$ is the number of toyMC samples. The nominal covariance matrix V^{norm}_{sys} is then rescaled by the prediction of actual oscillation and new physics parameters in order to obtain V_{sys} as

$$(V_{sys})_{ij,pq} = (V^{norm}_{sys})_{ij,pq} \times F^{pred}_{i,p}(\theta_{13}, \Delta m^2_{ee}, ...) \times F^{pred}_{j,q}(\theta_{13}, \Delta m^2_{ee}, ...) \tag{6.9}$$

The V_{sys} includes now the absolute size of the uncertainties. Although, the assumption about scaling does not exactly express the covariance matrix dependence on the oscillation parameters, the difference was found negligible. The above described procedure is repeated for all sources of IBD signal related systematical uncertainty and the overall covariance matrix can be written as:

$$V_{sys} = V_{reactor} + V_{abs\_en\_scale} + V_{rel\_en\_scale} + V_{nonlinearity} + V_{iav} + V_{resolution} + V_{efficiency} \tag{6.10}$$

where the matrices express respectively the uncertainty related to reactors, determination of relative and absolute energy scale, liquid scintillator non-linearity, effects of inner acrylic vessel, energy resolution and detection efficiency.

The construction of the V_{bkg} covariance matrix is similar to V_{sys} based on 1000 toyMC samples with the background fluctuation. Unlike the V_{sys}, it does not depend on the oscillation parameters therefore we can directly calculate it as:

$$(V_{bkg})_{ij,pq} = \frac{1}{M} \sum^{toys} \left(F^{obs,toy}_{i,p} - F^{pred,toy}_{i,p}\right)\left(F^{obs,toy}_{j,q} - F^{pred,toy}_{j,q}\right) \tag{6.11}$$

Similar to the IBD signal systematics covariance matrix, we repeat this procedure for all main sources of background resulting in overall V_{bkg} obtained as:

$$V_{bkg} = V_{Li9} + V_{fast\_n} + V_{accidentals} + V_{AmC} + V_{\alpha\_n} \tag{6.12}$$

where matrices represent the uncertainty of the cosmogenic isotope background, fast neutrino background, accidentals, ^{241}Am-^{13}C radioactive source background and background related to the alpha particle from natural radioactivity.

For part of the analysis presented later, we would like to constrain the value of Δm^2_{ee} based on the measurements of other experiments. The measurement comes with some uncertainty, which needs to be taken into account. This is done by introduction of covariance matrix $V_{\Delta m^2}$. In order to obtain it we generate 1000 toyMC samples with the Δm^2_{ee} fluctuations and calculate the covariance matrix elements as:

$$(V_{\Delta m^2})_{ij,pq} = \frac{1}{M} \sum^{toys} \left(F^{obs,toy}_{i,p} - F^{pred,toy}_{i,p} \right) \left(F^{obs,toy}_{j,q} - F^{pred,toy}_{j,q} \right) \tag{6.13}$$

We should remind that the covariance matrix $V_{\Delta m^2}$ is included only in the case when we do not fit Δm^2_{ee} and instead, we use the constrained value.

There are two components of the statistical uncertainty. There is a statistical uncertainty of the near halls data propagated to the prediction of the Far Hall data. There is also statistical uncertainty of Far Hall data itself. In the case of one detector in near hall and one detector in the Far Hall the uncertainties are calculated as:

$$\sigma_{near}(F^{pred}) = \tfrac{F^{pred}}{N^{obs}} \sqrt{N^{obs} + N^{bkg}} \tag{6.14}$$

$$\sigma_{far}(F^{pred}) = \sqrt{F^{pred} + F^{bkg}} \tag{6.15}$$

where N^{obs} and N^{bkg} is the number of observed IBD events without background and background itself for the ADs in the near halls. F^{bkg} is the number background events in the Far Hall while F^{pred} is the IBD event prediction based on the near halls measurement. The total statistical uncertainty is then:

$$\sigma(F^{pred}) = \sqrt{\sigma^2_{near}(F^{pred}) + \sigma^2_{far}(F^{pred})} \tag{6.16}$$

However, we have 9 respectively 16 prediction combinations for 6AD and 8AD periods, which are correlated. Let us explain the situation using an example assuming simpler configuration with 2 ADs in the near hall and 2 ADs in the Far Hall. In this case, we have 4 prediction combinations ($F^{pred}_{1,1}, F^{pred}_{2,1}, F^{pred}_{1,2}, F^{pred}_{2,2}$). If we take e.g. predictions $F^{pred}_{1,1}, F^{pred}_{2,1}$ they are correlated since prediction is based on the same AD1 in the near hall. In this case, we can write the covariance matrix for vector ($F^{pred}_{1,1}, F^{pred}_{2,1}$) as:

$$\begin{pmatrix} \sigma^2_{near}(F^{pred}_{1,1}) + \sigma^2_{far}(F^{pred}_{1,1}) & \sigma_{near}(F^{pred}_{1,1})\sigma_{near}(F^{pred}_{2,1}) \\ \sigma_{near}(F^{pred}_{1,1})\sigma_{near}(F^{pred}_{2,1}) & \sigma^2_{near}(F^{pred}_{2,1}) + \sigma^2_{far}(F^{pred}_{2,1}) \end{pmatrix} \tag{6.17}$$

Similar for vector ($F^{pred}_{1,1}, F^{pred}_{1,2}$), where the predictions are correlated because they are for same AD1 in the Far Hall, we get the covariance matrix as:

$$\begin{pmatrix} \sigma^2_{near}(F^{pred}_{1,1}) + \sigma^2_{far}(F^{pred}_{1,1}) & \sigma_{far}(F^{pred}_{1,1})\sigma_{far}(F^{pred}_{1,2}) \\ \sigma_{far}(F^{pred}_{1,1})\sigma_{far}(F^{pred}_{1,2}) & \sigma^2_{near}(F^{pred}_{1,2}) + \sigma^2_{far}(F^{pred}_{1,2}) \end{pmatrix} \tag{6.18}$$

Then the full covariance matrix for vector of 4 prediction combination $(F_{1,1}^{pred}, F_{2,1}^{pred}, F_{1,2}^{pred}, F_{2,2}^{pred})$ from our simpler configuration is:

$$\begin{pmatrix} \sigma_{near}^2(F_{1,1}^{pred}) + \sigma_{far}^2(F_{1,1}^{pred}) & \sigma_{far}(F_{1,1}^{pred})\sigma_{far}(F_{1,2}^{pred}) & \sigma_{near}(F_{1,1}^{pred})\sigma_{near}(F_{2,1}^{pred}) & 0 \\ \sigma_{far}(F_{1,1}^{pred})\sigma_{far}(F_{1,2}^{pred}) & \sigma_{near}^2(F_{1,2}^{pred}) + \sigma_{far}^2(F_{1,2}^{pred}) & 0 & \sigma_{near}(F_{1,2}^{pred})\sigma_{near}(F_{2,2}^{pred}) \\ \sigma_{near}(F_{1,1}^{pred})\sigma_{near}(F_{2,1}^{pred}) & 0 & \sigma_{near}^2(F_{2,1}^{pred}) + \sigma_{far}^2(F_{2,1}^{pred}) & \sigma_{far}(F_{2,1}^{pred})\sigma_{far}(F_{2,2}^{pred}) \\ 0 & \sigma_{near}(F_{1,2}^{pred})\sigma_{near}(F_{2,2}^{pred}) & \sigma_{far}(F_{2,1}^{pred})\sigma_{far}(F_{2,2}^{pred}) & \sigma_{near}^2(F_{2,2}^{pred}) + \sigma_{far}^2(F_{2,2}^{pred}) \end{pmatrix} \tag{6.19}$$

In order to calculate the covariance matrix V_{stat} for 9 or 16 prediction combinations each with 37 energy bins we just extend the procedure described above.

6.1.4 Correlations between Predictions

As we have discussed before we have 9 prediction combinations for the 6AD period and 16 prediction combinations for 8 AD period. However, these predictions are correlated. It means that the rank of the covariance matrix V is lower than the number of columns (or lines). Therefore we can not obtain the inverted covariance matrix V^{-1} needed in the Eq.(6.6) for the χ^2 calculation.

In order to resolve this issue we have to reduce the number of predictions. Therefore we use only two combinations of predictions:

- F_{DB}: Prediction of the sum of the Far Hall ADs based on the ADs in Daya Bay near hall
- F_{LA}: Prediction of the sum of the Far Hall ADs based on the ADs in Ling Ao near hall

The predictions are calculating simply be combining the predictions $F_{k,i}(E_{vis})$ explained in Sec.6.1.1. For the 6AD period we get:

$$F_{DB}^{6AD} = (F_{4,1} + F_{5,1} + F_{6,1} + F_{4,2} + F_{5,2} + F_{6,2})/2 \tag{6.20}$$

$$F_{LA}^{6AD} = F_{4,3} + F_{5,3} + F_{6,3} \tag{6.21}$$

while for the 8AD period we get

$$F_{DB}^{8AD} = (F_{4,1} + F_{5,1} + F_{6,1} + F_{7,1} + F_{4,2} + F_{5,2} + F_{6,2} + F_{7,2})/2 \tag{6.22}$$

$$F_{LA}^{8AD} = (F_{4,3} + F_{5,3} + F_{6,3} + F_{7,3} + F_{4,8} + F_{5,8} + F_{6,8} + F_{7,8})/2 \tag{6.23}$$

$$\tag{6.24}$$

This combination can be done without loosing any information in constraining the systematic uncertainty since the single uncertainties are either fully correlated among ADs in the same experimental hall or completely uncorrelated.

The final covariance matrix then has got dimension $2 \times 2 \times 37 = 148$ for 2 periods (6AD,8AD), 2 prediction combinations (F_{DB},F_{LA}) and 37 prompt energy spectrum bins. The covariance matrix coefficients are shown for the illustration in Fig.6.2.

6.2 Statistical Methods

In our searches we want to quantify how well are the measured data described by standard oscillations with three-neutrino flavours or if there is any room left

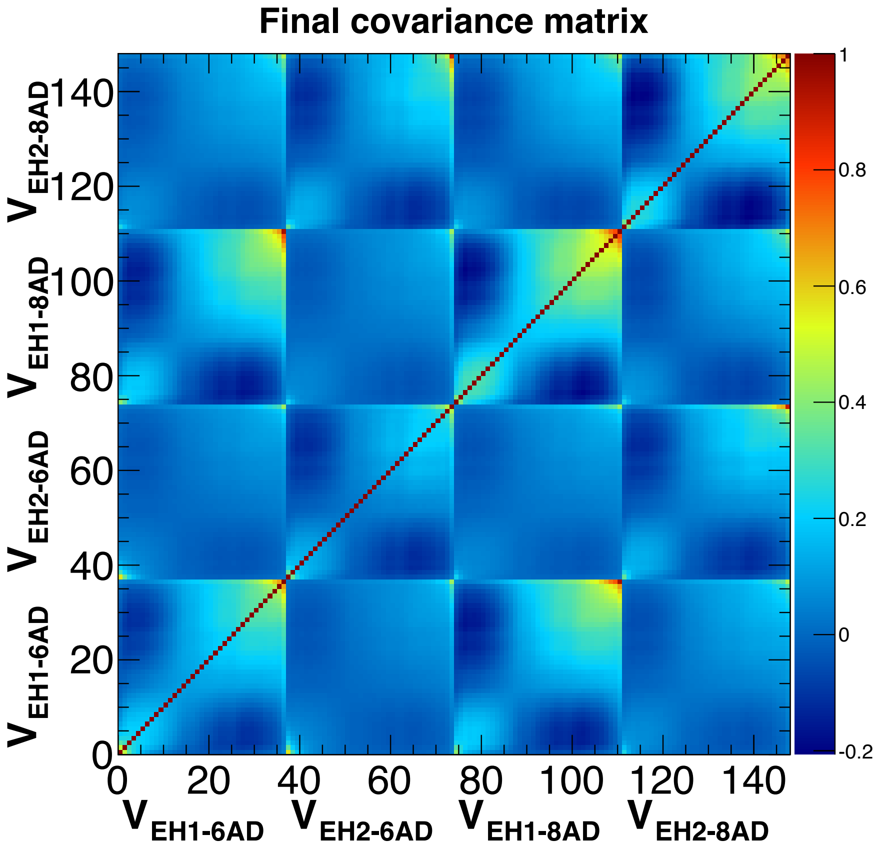

Figure 6.2: The final correlation matrix coefficients ($V_{ij}/\sqrt{V_{ii}V_{jj}}$), which include the statistical and systematical uncertainties as well as express the correlation between 2 periods of Daya Bay layout (6AD, 8AD), two prediction combinations based on the Daya Bay near hall (EH1) and Ling Ao near hall (EH2) and 37 energy bins of the prompt energy spectrum [71]. For the record, matrix in this figure does not include the $V_{\Delta m^2}$ contribution.

for new physics. Either way, we would like to set constraints on the new physics parameters.

In order to do that we use particular statistical methods described in this section, which is divided into three parts. First we mention p-value calculation used for quantification of the statistical significance of the effects of new physics. Then we discuss the Confidence Intervals (CI) method for the parameter estimation. This method is used in the search for NSIs. Unfortunately, we cannot use it in the search for LIV. As we will explain in detail later it is computationally demanding. Nevertheless, since we do not observe any significant deviation from standard oscillations in the search for LIV we can use alternative Gaussian $\mathrm{CL_S}$ method [72] described in the third part of this section to set exclusion limits on LIV parameters.

6.2.1 Statistical Significance of New Physics: p-value

At the beginning we want to calculate the significance or insignificance of the new physics with respect to the standard oscillations by calculating the p-value.

We compare here two hypotheses, H0 and H1:

- **Null hypothesis H0** is the scenario of standard oscillations with three neutrino flavours with the oscillation parameter set β_{SO}. That is $\sin^2 2\theta_{13}$ and eventually Δm^2_{ee}.
- **Alternative hypothesis H1** contains new physics with set of oscillation parameters β_{H0} and additional set of parameters β_{NP}. There can be either SME parameters for LIV case-by-case study or combined parameters X_i's used in the full formula eventually NSIs parameters.

We can define $\Delta\chi^2$ as:

$$\Delta\chi^2_p \equiv {\chi^2_{min}}^{H0} - {\chi^2_{min}}^{H1} = \min_{\beta_{SO}} \chi^2(\beta_{SO}, \beta_{NP} = 0) - \min_{\beta_{SO},\beta_{NP}} \chi^2(\beta_{SO}, \beta_{NP}) \quad (6.25)$$

where χ^2 defined in Eq.(6.6) is among others function of the oscillation new physics parameters parameters. The calculation is done using measured data. Using the $\Delta\chi^2_p$ we can calculate the p-value as

$$p = \int_{\Delta\chi^2_p}^{\infty} \chi^2_{DoF}(x)dx \quad (6.26)$$

where we assume that the parent distribution of $\Delta\chi^2_p$ is χ^2-distributed with appropriate number of degrees of freedom (DoF) equals to the number of parameters in set β_{NP}. The validity of this assumption is discussed in detail in the next section.

The p-value can be interpreted in terms of significance of the new physics signal. If the p-value is small our data are not likely to be interpreted with standard three-neutrino framework and such a low value could point to the possible existence of new physics. If the p-value is reasonably large, $p \gtrsim 0.1$, there is no significant deviation from the null hypothesis H0 and the possible existence of new physics cannot be distinguished from standard oscillations.

6.2.2 Parameter Estimation - Confidence Intervals

We would like to estimate the new physics parameters using Confidence Intervals method (CI).

In the most general case we estimate the value of all parameters in the model at once. We define $\Delta\chi^2$ defined as

$$\Delta\chi^2(\beta_{SO}, \beta_{NP}) \equiv \chi^2(\beta_{SO}, \beta_{NP}) - \chi^2_{BF} \quad (6.27)$$

which is the function of all standard β_{SO} and new physics β_{NP} parameters. The best-fit χ^2_{BF} is the minimal value of χ^2 in the parameters space which can be written as:

$$\chi^2_{BF} = \min_{\beta_{SO},\beta_{NP}} \chi^2(\beta_{SO}, \beta_{NP}) \quad (6.28)$$

The particular combination of parameters (β_{SO}, β_{NP}) is allowed by the data on the certain confidence level c if the $\Delta\chi^2(\beta_{SO}, \beta_{NP})$ is below critical level t_c defined by

$$P\left(\Delta\chi^2(X) \leq t_c\right) \geq c \quad (6.29)$$

The X is the random realization under the hypothesis that (β_{SO}, β_{NP}) are true parameters and $\Delta\chi^2(X)$ is corresponding parent distribution. Remember we think about measured data as the one of many realizations of the true model and thus $\Delta\chi^2(\beta_{SO}, \beta_{NP})$ is one of the realizations of the $\Delta\chi^2$ parent distribution. The calculation provides us the confidence intervals (CI), which include the parameter values compatible with the data.

If we want to estimate the subset of parameters $\beta \subset (\beta_{SO} \oplus \beta_{NP})$, we treat the complementary parameters as a nuisance parameters and minimize over them. Then the relevant $\Delta\chi^2$ is defined as

$$\Delta\chi^2(\beta) \equiv \min_{\beta_{SO},\beta_{NP}\text{ but not }\beta} \chi^2(\beta) - \chi^2_{BF} \tag{6.30}$$

The determination of the critical level t_c can be quite peculiar. Although, under certain relatively stringent conditions the Wilks' theorem [73] tells us that the $\Delta\chi^2$ parent distribution is χ^2-distributed with appropriate number of degrees of freedom. This allows us to calculate the critical values from known parent distribution. We can call this method Wilks' CI. For our searches, the conditions are valid for the whole NSIs search and for LIV only around standard three-neutrino hypothesis, not for the whole parameter space. The particular condition, which is not satisfied, is the need to have open neighborhood in the parameter space around the point of interest. It happens that the allowed region is close to boundary $\sin^2 2\theta_{13} \to 0$ where we of course enforce the condition $\sin^2 2\theta_{13} \geq 0$.

When the conditions for Wilks' theorem are not satisfied we can still use the CI, however, we have to get the $\Delta\chi^2$ parent distribution and relevant critical values t_c using Monte Carlo (MC) simulation. To get the critical value for one point in the parameter space we have to generate N fake experiments and fill the obtained values of $\Delta\chi^2$ to the histogram, which in the limit $N \to \infty$ approaches $\Delta\chi^2$ parent distribution. Having the distribution, we can calculate the corresponding critical values using Eq.(6.29). We can call this procedure MC CI. One of the MC CI examples is Feldman-Cousins method [74]. Although straightforward, it is computationally demanding and for some cases like our LIV search not even feasible. Therefore we have to find other way to constrain the LIV parameters.

6.2.3 Exclusion Limits for the Lorentz Invariance Violation - Gaussian $\mathrm{CL_S}$ Method

As we will see later, we have not found any significant deviation from the standard oscillations in three-neutrino framework in our search for LIV. Therefore, we can only set the exclusion limits for LIV parameters.

Since the MC CI is computationally demanding we can use alternative $\mathrm{CL_S}$ method to set exclusion limits [75], [76]. This method is commonly used not only in high-energy physics accelerator experiments but for example Daya Bay used this approach to set constraints on possible existence of light sterile neutrino [77], [78]. We should stress that the $\mathrm{CL_S}$ method is complementary to CI in settling exclusion limits however it does not provide the parameter estimation. As soon as new physics signal is observed we have to use CI to set the parameter limits.

The $\mathrm{CL_S}$ method [75] compares two hypotheses mentioned in Sec.6.2.1: null hypothesis H0, in our case the standard oscillations in three-neutrino framework and alternative hypothesis H1, in our case new physics scenario. It is based on the likelihood ratio

$$\mathrm{CL}_s = \frac{1-p_1}{1-p_0}. \tag{6.31}$$

where p_0 and p_1 are the p-values for null and alternative hypothesis respectively. Small values of $\mathrm{CL_S}$ favour H0 over H1 thus we can constrain H1. Usually we use 95% $\mathrm{CL_S}$ exclusion region for H1 which corresponds to the CL_s<0.05 [79].

In order to calculate the p_0 and p_1 we complementary, to the $\Delta\chi^2$ defined in Eq.(6.27), define ΔT as

$$\Delta T \equiv {\chi^2_{H0}}^{min} - {\chi^2_{H1}}^{min} \tag{6.32}$$

where H0 is a null hypothesis, in our case standard oscillations in three-neutrino framework, with

$${\chi^2_{H0}}^{min} = \min \chi^2(\beta_{SO}, \beta_{NP} = 0) \tag{6.33}$$

and H1 is an alternative hypothesis, in our case new physics scenario, with

$${\chi^2_{H1}}^{min} = \min \chi^2(\beta_{SO}, \beta_{NP}) \tag{6.34}$$

In both cases, we minimize over nuisance or unknown parameters. We specify in detail the forms of the ${\chi^2_{H0}}^{min}$ and ${\chi^2_{H1}}^{min}$ for the LIV search in the Sec.7.2.

For the $\mathrm{CL_S}$ method we get two parent distributions ΔT_{H0} and ΔT_{H1} which assume H0 or H1 respectively to be true. Using the $\Delta T(data)$ obtained from the measured data we can calculate the p_0 and p_1, and consequently $\mathrm{CL_S}$ value using Eq.(6.31). The sketch of this procedure is shown in Fig.6.3.

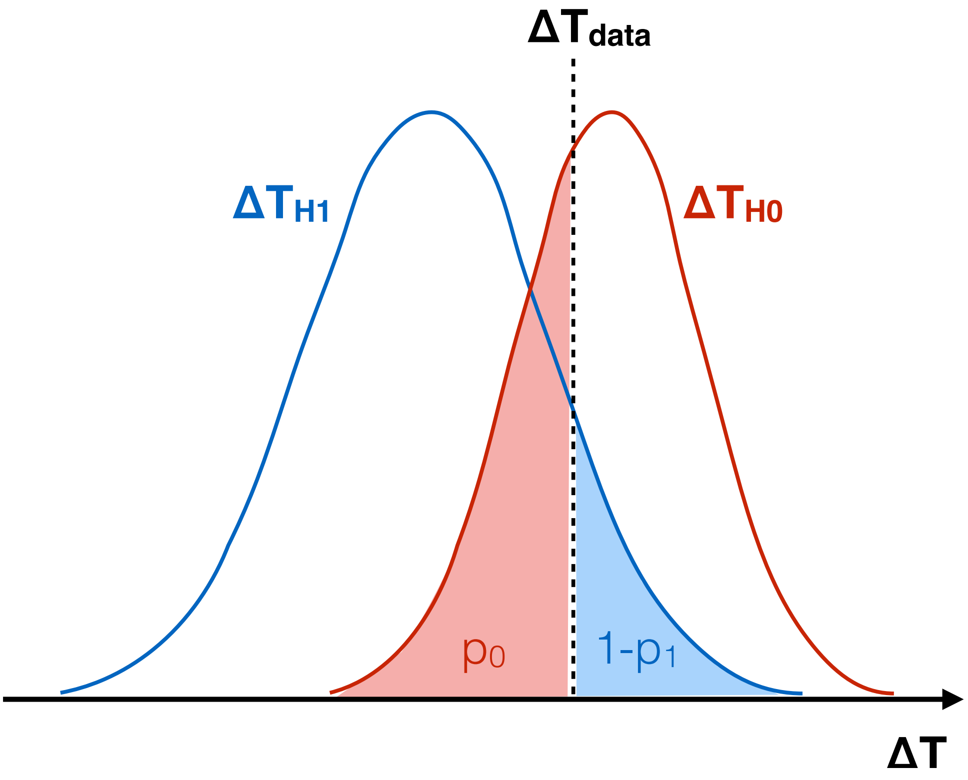

Figure 6.3: The sketch of the Gaussian $\mathrm{CL_S}$ method.

The parent distribution for ΔT in Eq.(6.32) can be approximated under moderate conditions by normal distribution [80], [72]. These conditions are much easier to satisfy than the conditions for Wilks' theorem. The conditions are [72]:

- The parameter space and nuisance parameter space are continuous and the likelihood function is smooth function, i.e. have continuous derivatives.
- Data size is large
- The best model of H0 hypothesis and the alternative hypothesis H1 are relatively close.

Since we approximate the ΔT's by normal distributions we refer to the method as the Gaussian $\mathrm{CL_S}$. In general, conditions for the assumption are valid for the LIV search in Daya Bay.

It was proven in [72] that the ΔT_H distribution under the hypothesis H can be approximated by normal distribution $N\left(\overline{\Delta T_H}, 2\sqrt{|\overline{\Delta T_H}|}\right)$ where:

$$\overline{\Delta T_H} = \langle \Delta T(x_H^{Asimov}) \rangle \tag{6.35}$$

is the mean value of ΔT_H distribution calculated using Asimov data set [80], i.e. Monte Carlo simulation of the experiment under true hypothesis H without any statistical or systematical fluctuations. Having the normal distribution the calculation of the p-values is done simply as:

$$\begin{aligned} p_0 &= 0.5 - 0.5 \times \mathrm{Erf}\left(\frac{\overline{\Delta T_{H0}} - \Delta T(data)}{\sqrt{8\overline{\Delta T_{H0}}}}\right) \\ p_1 &= 0.5 - 0.5 \times \mathrm{Erf}\left(\frac{\overline{\Delta T_{H1}} - \Delta T(data)}{\sqrt{8\overline{\Delta T_{H1}}}}\right), \end{aligned} \tag{6.36}$$

where Erf stands for the error function and $\Delta T(data)$ is the value based on measured data. The $\mathrm{CL_S}$ value can be then calculated as:

$$\mathrm{CL_S} = \frac{0.5 + 0.5 \times \mathrm{Erf}\left(\frac{\overline{\Delta T_{H0}} - \Delta T(data)}{\sqrt{8\overline{\Delta T_{H0}}}}\right)}{0.5 - 0.5 \times \mathrm{Erf}\left(\frac{\overline{\Delta T_{H1}} - \Delta T(data)}{\sqrt{8\overline{\Delta T_{H1}}}}\right)} \tag{6.37}$$

The Gaussian $\mathrm{CL_S}$ method is computationally simple, especially with comparison to MC CI. For each the point in the parameter space we have to produce only two toyMC sets: x_{H0}^{Asimov}, x_{H1}^{Asimov} and get three ΔT's: ΔT_{H0}, ΔT_{H1}, $\Delta T(data)$. In summary, the Gaussian $\mathrm{CL_S}$ method offers us alternative relatively quick procedure to set exclusion limits in the search for LIV.

7. Results

7.1 Neutrino Oscillations in Three-neutrino Framework

In the beginning of this chapter, we present the analysis of Daya Bay data in standard three-neutrino framework without any effects of new physics since it was the original purpose of the experiment. Moreover, the results are the starting point for our searches for LIV and NSIs. The obtained values of the oscillation parameters can be compared with those found in the cases of new physics.

In Daya Bay, there were developed several independent procedures how to get the oscillations parameters providing consistent result. The LBNL fitter is one of them. We will use modified LBNL fitter described in previous chapter for parameter estimation or setting exclusion limits. The analysis as well as the searches for physics BSM are based on 621 days of data collected from December 2011 till November 2013. We will also briefly mention the most recent result from Daya Bay based on in total 1230 days of data obtained by different statistical method.

7.1.1 Oscillation Probability Formula and Introduction of Δm^2_{ee}

The analysis of relative near-far measurement using prediction for Far Hall based on the measurement in the near halls was done assuming slightly different oscillation probability than the one shown in Eq.(5.2). The used probability is:

$$P(\bar{\nu}_e \to \bar{\nu}_e) = 1 - \sin^2 2\theta_{12} \sin^2 \frac{\Delta m^2_{21} L}{4E} - \sin^2 2\theta_{13} \sin^2 \frac{\Delta m^2_{ee} L}{4E} \tag{7.1}$$

where we introduced effective mass squared difference Δm^2_{ee} [59], which combines the effects of Δm^2_{31} and Δm^2_{32}. Let us first mention that this rather simplification is very well justified. In Fig.7.1, there is shown the difference between the oscillation probability in Eq.(5.2) with both Δm^2_{31}, Δm^2_{32} and the oscillation probability in Eq.(7.1) with single mass squared difference Δm^2_{ee} for typical reactor antineutrino energy $E_\nu = 3.5$ MeV as well as their ratio as a function of distance. The relative difference is lower than 0.1%, which is negligible. We can conclude that the oscillation probabilities are equivalent.

The use of Δm^2_{ee} has particular advantage. Its measurement is independent on the neutrino mass hierarchy unlike mass squared differences Δm^2_{31} and Δm^2_{32}.

The disadvantage of the parameter Δm^2_{ee} is that it is not fundamental parameter. Therefore, we would like to have the way how to convert this value to the actual mass squared differences Δm^2_{31} and Δm^2_{32}, which are connected by condition $|\Delta m^2_{31}| = |\Delta m^2_{32}| \pm |\Delta m^2_{21}|$ where "+" sign is for the normal and "-" sign is for inverted hierarchy. Using this relation in the probability in Eq.(5.2), we get:

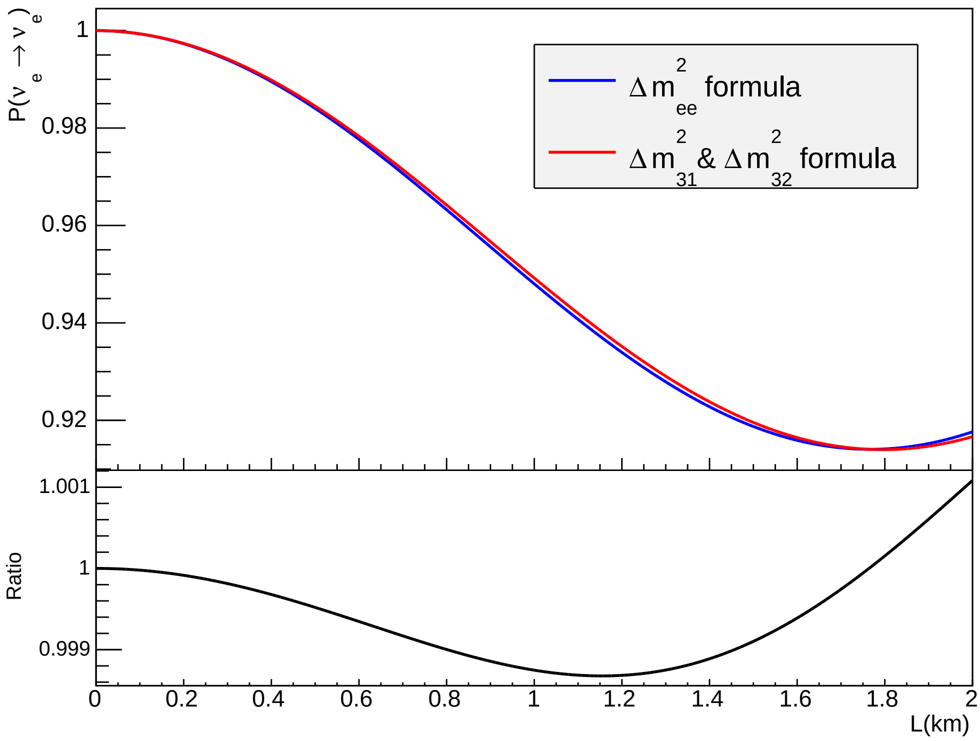

Figure 7.1: Upper panel: The oscillation probability formulae with both Δm^2_{31}, Δm^2_{32} in Eq.(5.2) and the oscillation probability with single mass squared difference Δm^2_{ee} in Eq.(7.1) as a function of distance for typical reactor antineutrino energy $E_\nu = 3.5$ MeV. Lower panel: The ratio of $P(\Delta m^2_{ee})/P(\Delta m^2_{31}, \Delta m^2_{32})$.

$$\begin{aligned} P(\bar{\nu}_e \to \bar{\nu}_e) = 1 - \sin^2 2\theta_{12} \sin^2 \frac{\Delta m^2_{21} L}{4E} \\ - \sin^2 2\theta_{13} \frac{1 - \sqrt{1 - \sin^2 2\theta_{12} \sin^2 \frac{\Delta m^2_{21} L}{4E}} \cos\left(\frac{\Delta m^2_{32} L}{2E} \pm \phi\right)}{2} \end{aligned} \tag{7.2}$$

where $\phi = \arctan \frac{\sin \frac{\Delta m^2_{21} L}{2E}}{\cos \frac{\Delta m^2_{21} L}{2E} + \tan^2 \theta_{12}}$. For typical reactor antineutrino energy and distances in Daya Bay experiment, it holds that $\sin^2 \frac{\Delta m^2_{21} L}{4E} << 1$ therefore we can write:

$$P(\bar{\nu}_e \to \bar{\nu}_e) \simeq 1 - \sin^2 2\theta_{12} \sin^2 \frac{\Delta m^2_{21} L}{4E} - \sin^2 2\theta_{13} \sin^2 \left(\frac{\Delta m^2_{32} L}{4E} \pm \frac{\phi}{2}\right) \tag{7.3}$$

If we compare Eq.(7.3) with Eq.(7.1) we get the relation between Δm^2_{32} and Δm^2_{ee} as

$$|\Delta m^2_{ee}| = |\Delta m^2_{32}| \pm \Delta m^2_\phi = |\Delta m^2_{31}| \mp (|\Delta m^2_{21}| - \Delta m^2_\phi) \tag{7.4}$$

where $\Delta m^2_\phi = \phi \frac{2E}{L}$.

Let us now calculate the value of Δm^2_ϕ. By definition, it is function of distance and energy. The Fig.7.2 shows the Δm^2_ϕ as a function of antineutrino energy for the distance L=1.8 km. We can see that it is almost constant with value $\Delta m^2_\phi \simeq 5.17 \times 10^{-5}$ eV^2. Finally, the conversion between Δm^2_{32} and Δm^2_{ee} is

$$|\Delta m^2_{ee}| = |\Delta m^2_{32}| \pm 5.17 \times 10^{-5} \text{ eV}^2 \tag{7.5}$$

where we remind that "+" sign is for the normal and "-" sign is for inverted hierarchy.

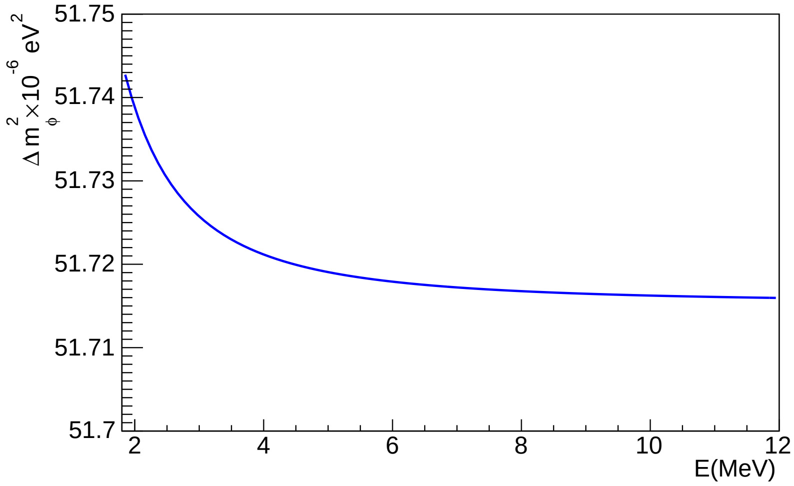

Figure 7.2: The Δm^2_ϕ as a function of energy for distance L=1.8 km. The parameter is almost constant with value $\Delta m^2_\phi \simeq 5.17 \times 10^{-5}$ eV^2.

For completeness, the values of other oscillation parameters used in the analysis are: $\sin^2 2\theta_{12} = 0.857 \pm 0.024$ [81], $\Delta m^2_{21} = (7.50 \pm 0.20) \times 10^{-5}$ eV^2 [81], $\sin^2 2\theta_{23} = 1$. Although the survival probability $P(\bar{\nu}_e \to \bar{\nu}_e)$ in three-neutrino framework does not depend on θ_{23}, such a dependence emerges if the effects of LIV are included.

7.1.2 Precise Measurement of $\sin^2 2\theta_{13}$ and Δm^2_{ee}

Let us now present the final results for the measurement of the standard oscillation parameters $\sin^2 2\theta_{13}$ and Δm^2_{ee} based on 621 days of data [59]. The best-fit values are

$$\sin^2 2\theta_{13} = 0.084 \pm 0.005 \tag{7.6}$$
$$|\Delta m^2_{ee}| = (2.42 \pm 0.11) \times 10^{-3} \text{ eV}^2 \tag{7.7}$$
$$\chi^2_{BF}/DoF = 134.6/146 \tag{7.8}$$

The value of χ^2_{BF} with the comparison to 146 degrees of freedom suggests that data are very well consistent with the standard three-neutrino oscillations. This of course reduces our hopes to find any signal of physics BSM. Nevertheless, Daya Bay can still provide useful limits on the parameters of new physics.

To demonstrate the superb power of the Daya Bay experiment in the measurement of oscillation parameters $\sin^2 2\theta_{13}$ and Δm^2_{ee} we present the most recent measurement based on the 1230 days of data [36]. The best-fit values of the parameters are:

$$\sin^2 2\theta_{13} = 0.0841 \pm 0.0027(\text{stat.}) \pm 0.0019(\text{syst.}) \tag{7.9}$$

$$|\Delta m^2_{ee}| = (2.50 \pm 0.06(\text{stat.}) \pm 0.06(\text{syst.})) \times 10^{-3}\ \text{eV}^2 \tag{7.10}$$

$$\chi^2_{BF}/DoF = 232.6/263 \tag{7.11}$$

We should first notice the number of degrees of freedom changed due to the use of different statistical approach developed independently on LBNL fitter within Daya Bay. Nevertheless, LBNL fitter using the same data provides consistent result. The precision of the parameters is spectacular having only ∼4% relative uncertainty for the mixing angle. In addition, the precision of $|\Delta m^2_{ee}|$ measurement is comparable to the precision of accelerator experiments measuring similar mass square difference [82], [83].

Such a precision motivates us to use the capabilities of Daya Bay and go beyond standard three-neutrino mixing. We have explored two possible scenarios for new physics, which is described in following sections.

7.2 Search for Isotropic Lorentz Invariance Violation

In this section, we present the results of our search for Lorentz Invariance Violation (LIV) using both case-by-case survival probabilities listed in Eqs.(3.21)-(3.26) and full formula in Eq.(3.32). For the entire search we use constrained value $\Delta m^2_{ee} = (2.48 \pm 0.07) \times 10^{-3}$ eV^2 which is the average value of $|\Delta m^2_{32}|$ for the normal and inverted hierarchy [84]. We fix the Δm^2_{ee} and include its uncertainty to the additional contribution $V_{\Delta m^2}$ to the overall covariance matrix. We consider no CP-violation in the mixing matrix ($\delta_{CP} = 0$).

On the contrary to the standard oscillation analysis performed in the three-neutrino framework the probabilities with LIV effects depend on the hierarchy. Especially, particular LIV terms change sign with the change of the hierarchy since they are odd functions of Δm^2_{31} and Δm^2_{32}. In the beginning, we will assume normal mass hierarchy and later add the discussion of the results assuming inverted mass hierarchy.

The presence of isotropic LIV can be observed in the oscillation pattern, which exhibit deviation from the standard oscillations. The illustration is shown in Fig.7.3 where we show the ratio of far data over weighted average of near data. The lines correspond to the prediction for the best fit for the standard oscillations as well as examples of the distortion by the presence of LIV. The particular combinations of LIV parameters provide oscillation pattern quite different from the measured signal and therefore can be excluded.

7.2.1 Significance of Lorentz Invariance Signal

We use the p-value to quantify the significance of the LIV signal. For the case-by-case formulae we ended up with three free parameters: $\sin^2 2\theta_{13}$ and appropriate combination of $(a_L)^T_{\alpha\beta}$ and $(c_L)^{TT}_{\alpha\beta}$. For each formula in Eqs. (3.21)-(3.26) we have find the best-fit values with global minimum $\chi^2_{\alpha\beta}/145$ DoF. We

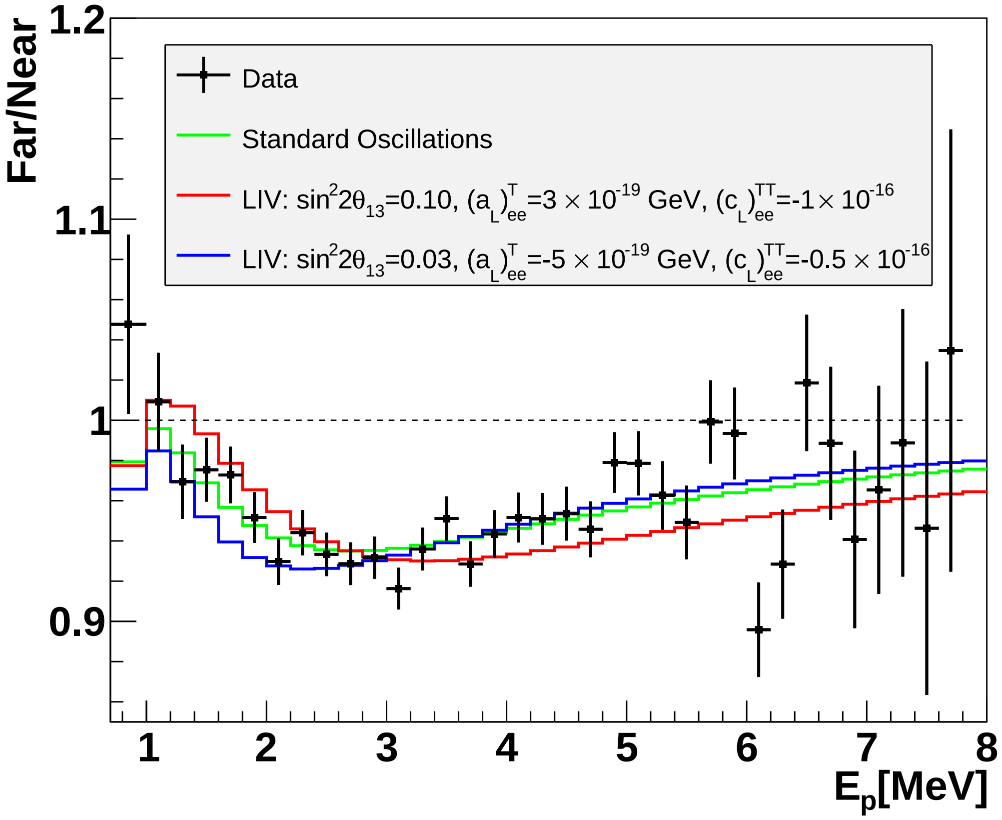

Figure 7.3: The ratio of far data over weighted average of near data. The black points represent the measured data with their uncertainty. The green line corresponds to the best fit of the standard oscillations with $\sin^2 2\theta_{13} = 0.084$ and LIV parameters being zero. There are two examples of the distortion by the LIV effect for the *ee* case for parameters $\sin^2 2\theta_{13} = 0.10$, $(a_L)^T_{ee}, (c_L)^{TT}_{ee} = 3 \times 10^{-19}$ GeV, $(c_L)^{TT}_{ee} = -1 \times 10^{-16}$ (red) and $\sin^2 2\theta_{13} = 0.03$, $(a_L)^T_{ee}, (c_L)^{TT}_{ee} = -5 \times 10^{-19}$ GeV, $(c_L)^{TT}_{ee} = -0.5 \times 10^{-16}$ (blue).

have also found the minimum $\chi^2_0 = 134.74/147$ DoF for the LIV conservation i.e. $(a_L)^T_{\alpha\beta} = (c_L)^{TT}_{\alpha\beta} = 0$, which is slightly higher than standard oscillation result ($\chi^2_{BF} = 134.6/146$ DoF) in Eq.(7.8) due to the different value of Δm^2_{ee}. We define $\Delta\chi^2_{\alpha\beta}$, which is the specific case of the general definition in Eq.(6.25), as:

$$\Delta\chi^2_{\alpha\beta} \equiv \chi^2_0 - \chi^2_{\alpha\beta} \tag{7.12}$$

and obtain p-value assuming that parent distribution $\Delta\chi^2_{\alpha\beta}$ is χ^2-distributed with 2 degrees of freedom (DoF). Those two DoF correspond to two LIV parameters. The results of this procedure for each flavour combination $\alpha\beta$ are shown in Tab.7.1. We have found relatively high p-values, which suggest that data for all cases are consistent with Lorentz Invariance conservation. That was already expected since Daya Bay data were found to be consistent with standard three-neutrino oscillations.

The p-values were obtained with the assumption that the parent $\Delta\chi^2_{\alpha\beta}$ in Eq.(7.12) is χ^2-distributed. The check of this assumption was performed for the

Case	Best-fit $\chi^2_{\alpha\beta}$	$\Delta\chi^2_{\alpha\beta}$	p-value
ee	133.326	1.41	0.494
$\mu\mu$	133.337	1.3	0.522
$\tau\tau$	133.323	1.413	0.493
$e\mu$	131.921	2.815	0.245
$e\tau$	131.931	2.805	0.246
$\mu\tau$	133.325	1.411	0.494

Table 7.1: The significance of LIV signal for case-by-case formulae in Eqs.(3.21)-(3.26). For each case we show best-fit $\chi^2_{\alpha\beta}$, $\Delta\chi^2_{\alpha\beta}$ and appropriate p-value assuming parent distribution of $\Delta\chi^2$ is χ^2-distributed. Note that we obtained $\chi^2_0 = 134.74$ for the case of Lorentz Invariance conservation.

ee case survival probability in Eq.(3.21). We have produced 1000 toyMCs with systematical and statistical fluctuations. The best-fit χ^2_{ee} as well as χ^2_0 for the Lorentz Invariance conservation case was found for each toyMC. The calculation of $\Delta\chi^2_{\alpha\beta}$ was done using Eq.(7.12) and expected $\Delta\chi^2_{ee}$ parent distribution was obtained. Then we fitted parent distribution with χ^2_2 distribution for 2 DoF. Nice agreement was observed, which supports our assumption about the χ^2 shape of the parent distribution. The results are shown in Fig.7.4.

In addition, we have used $\Delta{\chi^2_{ee}}^{data} = 1.41$ obtained from the data to determine the p-value this time based on distribution from 1000 toyMCs . The corresponding p-value is 0.491, which is consistent with the previous value 0.494 obtained using the assumption about the shape of the parent distribution, see Tab.7.1. Since the values are almost same we do not have any reason to doubt that $\Delta\chi^2$ parent distribution is not χ^2-distributed for other cases too.

Similar exercise can be done for the full formula in Eq.(3.32), which includes the effect of all relevant SME parameters working together. There are five free parameters: $\sin^2 2\theta_{13}$ and four LIV parameters X_1, X_2, X_3, X_4. The procedure to get the significance is same as for case-by-case. We have found the global minimum $\chi^2_{full} = 131.12/143$ DoF for the LIV case and $\chi^2_0 = 134.74/147$ DoF for the Lorentz Invariance conservation case. Corresponding $\Delta\chi^2 \equiv \chi^2_{full} - \chi^2_0 = 3.62$ results in p-value of 0.54 assuming that parent distribution of $\Delta\chi^2$ is χ^2-distributed with 4 DoF. We conclude that even for the full formula the data are consistent with Lorentz Invariance conservation.

7.2.2 Exclusion Limits for the Standard-Model Extension Parameters using Case-by-case Formulae

Without any significant signal of LIV, the Daya Bay experiment can proceed only to set limits on the LIV parameters. In order to do that we use Gaussian CL$_S$ method described in detail in Sec.6.2.3. This method compares two hypotheses. Hypothesis H1 is the case of LIV and the null hypothesis H0 is the case where Lorentz Invariance is conserved.

First, we present excluded region as a function of SME parameters $(a_L)^T_{\alpha\beta}$, $(c_L)^{TT}_{\alpha\beta}$ using case-by-case formulae in Eqs.(3.21)-(3.26). To obtain the exclusion contours we use grid of 61 × 61 points in the $(a_L)^T_{\alpha\beta}$-$(c_L)^{TT}_{\alpha\beta}$ plane. We used

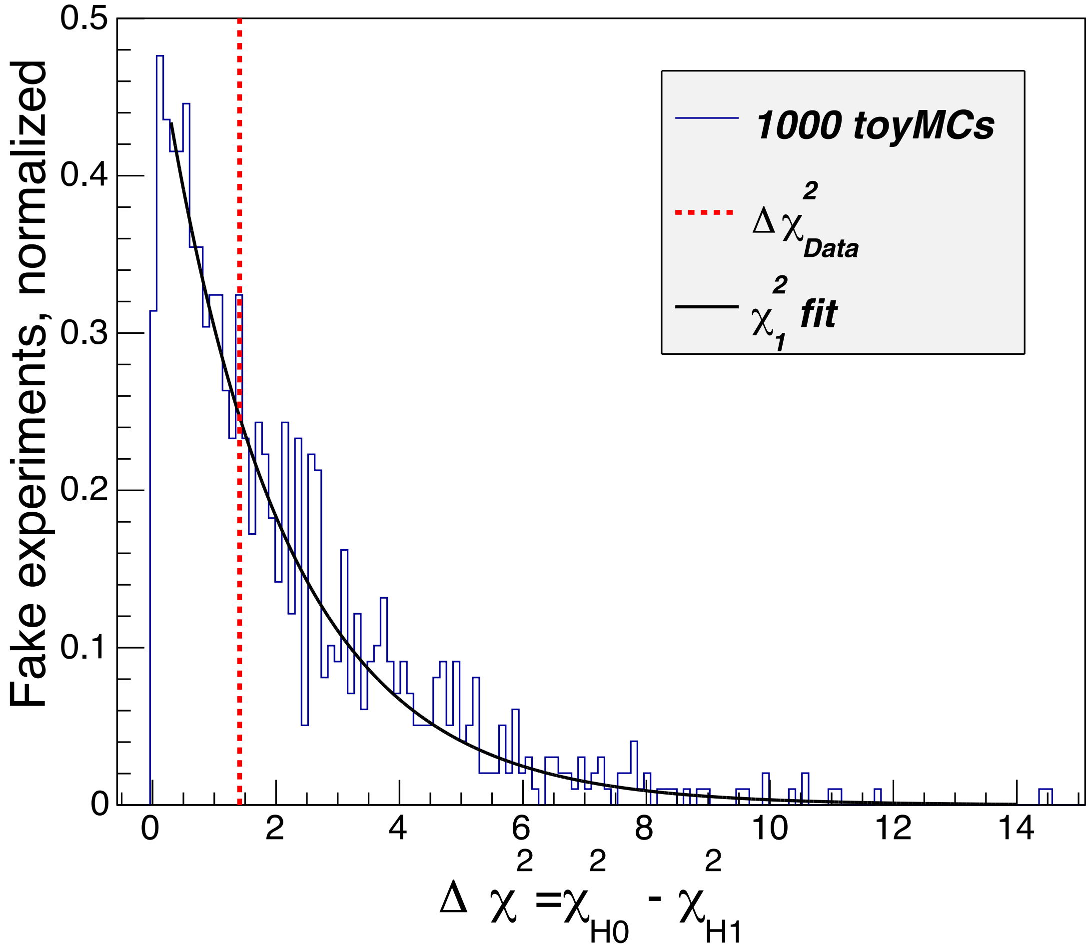

Figure 7.4: The $\Delta\chi^2_{ee}$ distribution obtained from 1000 toyMCs with statistical and systematical fluctuations for the case of Lorentz Invariance conservation. The vertical dashed line corresponds to $\Delta\chi^{2\ data}_{ee} = 1.41$ obtained from the data. The red curve represent the fit with the χ^2 distribution function with 2 DoF which match the distribution based on 1000 toyMCs.

optimized size of the grid for each case with boundaries listed in Tab.7.2. For each point we calculate the CL$_S$ value using the Gaussian CL$_S$ method. For the H1, the $(a_L)^T_{\alpha\beta}$, $(c_L)^{TT}_{\alpha\beta}$ values are set to the coordinates of the point of grid in $(a_L)^T_{\alpha\beta}$-$(c_L)^{TT}_{\alpha\beta}$ plane. The value of $\sin^2 2\theta_{13}$ is treated as unconstrained nuisance parameter thus determined for each point separately as the best fit to the measured data. For the H0, the values of SME parameters are obviously zero and the value of $\sin^2 2\theta_{13}$ is again determined by the best fit to the data. The value $\sin^2 2\theta^{H0}_{13} = 0.084$ is equal to the result of standard three-neutrino oscillation analysis, see Eq.(7.6). Although in general, it can be slightly different due to the value of Δm^2_{ee} used in the analysis which is slightly different from the best fit for standard oscillations in Eq.(7.7).

The obtained exclusion contours on 95% CL$_\text{S}$ level for each flavour combination are shown in Fig.7.5 and Fig.7.6.

For all cases the null hypothesis point, i.e. $(a_L)^T_{\alpha\beta} = (c_L)^{TT}_{\alpha\beta} = 0$ is within the allowed region. There are two reasons for that. First, this agrees with our previous observation since we have not found any significant deviation from Lorentz

Case	$(a_L)^T_{\alpha\beta}$ min	$(a_L)^T_{\alpha\beta}$ max	$(c_L)^{TT}_{\alpha\beta}$ min	$(c_L)^{TT}_{\alpha\beta}$ max
ee	-2×10^{-19} GeV	4×10^{-19} GeV	-4×10^{-16}	1×10^{-16}
$\mu\mu$	-4×10^{-19} GeV	4×10^{-19} GeV	-2×10^{-16}	4×10^{-16}
$\tau\tau$	-4×10^{-19} GeV	4×10^{-19} GeV	-2×10^{-16}	4×10^{-16}
	$\mathrm{Re}(a_L)^T_{\alpha\beta}$ min	$\mathrm{Re}(a_L)^T_{\alpha\beta}$ max	$\mathrm{Re}(c_L)^{TT}_{\alpha\beta}$ min	$\mathrm{Re}(c_L)^{TT}_{\alpha\beta}$ max
$e\mu$	-0.8×10^{-19} GeV	0.8×10^{-19} GeV	-0.06×10^{-16}	0.1×10^{-16}
$e\tau$	-0.8×10^{-19} GeV	0.8×10^{-19} GeV	-0.06×10^{-16}	0.1×10^{-16}
$\mu\tau$	-4×10^{-19} GeV	4×10^{-19} GeV	-2×10^{-16}	4×10^{-16}

Table 7.2: Minimum and maximum values of the 61 × 61 grid in $(a_L)^T_{\alpha\beta}$-$(c_L)^{TT}_{\alpha\beta}$ parameter space used in the scan to obtain $\mathrm{CL_S}$ exclusion contours.

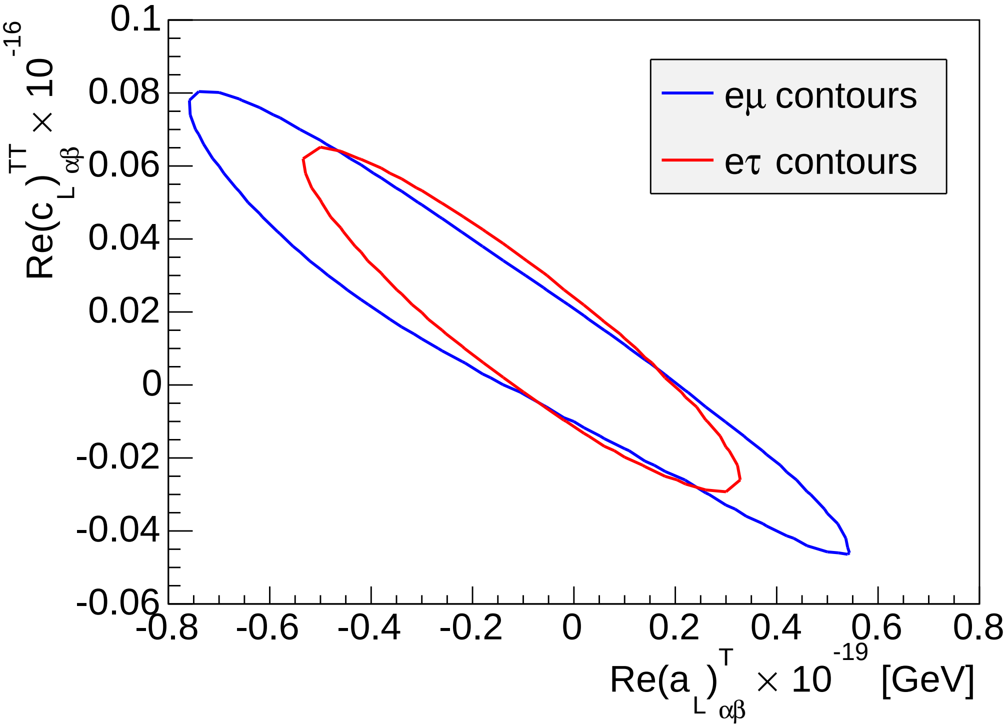

Figure 7.5: Exclusion contours at 95% $\mathrm{CL_S}$ level for parameters $\mathrm{Re}(a_L)^T_{\alpha\beta}$, $\mathrm{Re}(c_L)^{TT}_{\alpha\beta}$ for $e\mu$ (blue) and $e\tau$ (red) cases. The excluded region is outside closed contours.

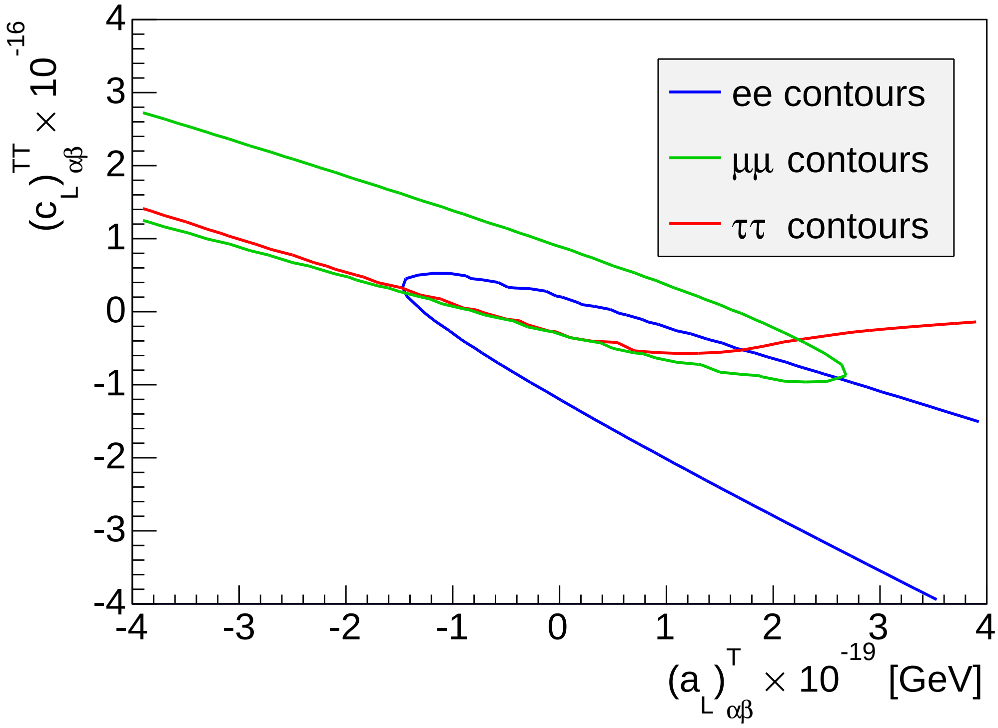

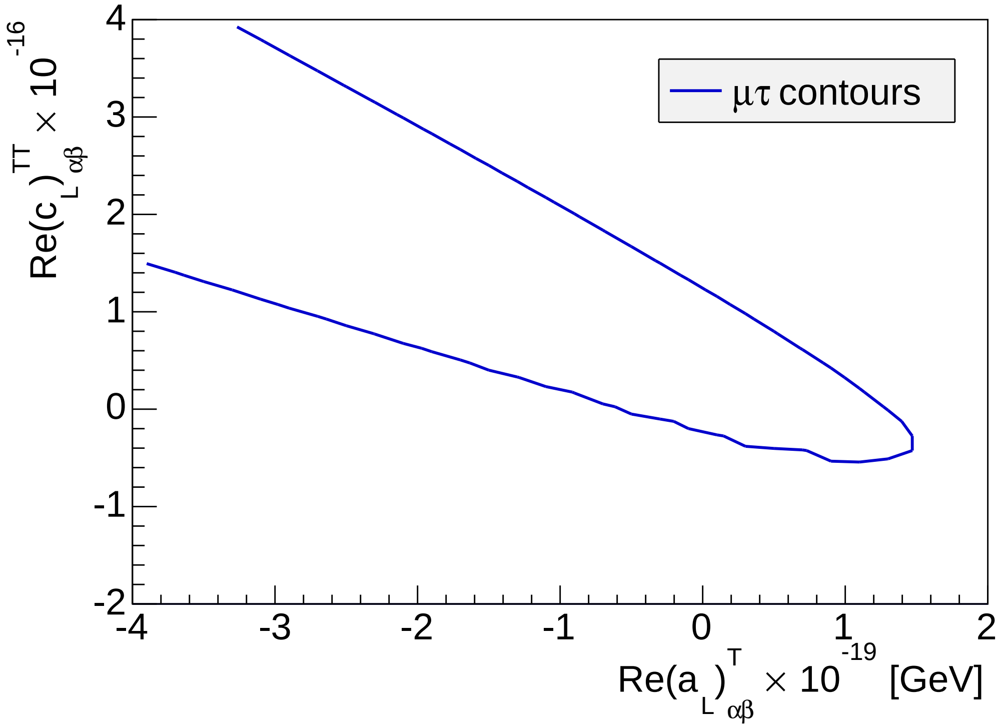

Figure 7.6: Top: Exclusion contours at 95% CL_S level for $(a_L)^T_{\alpha\beta}$, $(c_L)^{TT}_{\alpha\beta}$ for ee, $\mu\mu$ and $\tau\tau$ cases. The excluded region for ee (blue), $\mu\mu$ (green) cases are outside the u-shaped unclosed contours while for $\tau\tau$ (red) case the excluded region is below the line. Bottom: Exclusion contours at 95% CL_S level for $(a_L)^T_{\alpha\beta}$, $(c_L)^{TT}_{\alpha\beta}$ for $\mu\tau$ case. The excluded region is outside the u-shaped unclosed contours.

Invariance conservation in the p-value calculation. Second, the CL$_S$ method cannot intrinsically exclude the null hypothesis H0, as long as it is nested hypothesis like in our case.

Qualitatively, we can separate these results into two groups. For $e\mu$ and $e\tau$ cases we get closed contours. On the contrary, there are four cases, namely ee, $\mu\mu$, $\tau\tau$ and $\mu\tau$, for which the contours do not close. For ee, $\mu\mu$ and $\mu\tau$ we get long narrow strip however for $\tau\tau$ case we get widely open allowed region. Open contours prevent us to set double-sided exclusion limits using exact form of the case-by-case formulae with two free SME parameters.

7.2.3 Revision of the Validity of the Assumptions for the Perturbative Expansion

In our procedure of setting limits on LIV parameters we treat $\sin^2 2\theta_{13}$ as a nuisance parameter. We use the best-fit value $\sin^2 2\theta_{13}^{BF}$ for each combination of either $(a_L)^T_{\alpha\beta}$, $(c_L)^{TT}_{\alpha\beta}$ or X_i's. It eventually happen that we get $\sin^2 2\theta_{13}^{BF} \to 0$ for particular combination LIV parameters allowed by Gaussian CL$_\text{S}$. There is an illustration for ee case in Fig.7.7 where we plotted $\sin^2 2\theta_{13}^{BF}$ as a function of SME parameters $(a_L)^T_{ee}$, $(c_L)^{TT}_{ee}$ overlaid by the exclusion contours. The region $\sin^2 2\theta_{13}^{BF} \to 0$ overlaps with the region of open contours which is same for all other open contours cases $\mu\mu$, $\tau\tau$ and $\mu\tau$. As we will show in next paragraphs, this is the region where the survival probability formula assumptions are not valid and the contours in this region cannot be trusted.

We have derived survival probability formulae in Eqs.(3.21)-(3.26) for the case-by-case and in Eq.(3.32) for the full formula as an expansion to the first perturbative order of SME parameters. Such formulae are good approximation as long as assumption $P^{(0)}_{\bar{\nu}_e\to\bar{\nu}_e} >> P^{(1)}_{\bar{\nu}_e\to\bar{\nu}_e} >> P^{(2)}_{\bar{\nu}_e\to\bar{\nu}_e}...$ holds. If we look closely to $P^{(0)}_{\bar{\nu}_e\to\bar{\nu}_e}$ defined in Eq.(3.7) we can see that the short baseline oscillation terms vanish for limit $\sin^2 2\theta_{13}^{BF} \to 0$ and $P^{(0)}_{\bar{\nu}_e\to\bar{\nu}_e} \simeq 1$. Since we observe short baseline oscillations in Daya Bay, the effect must be almost entirely created by LIV terms. This can be done but then the first order probability term is $P^{(1)}_{\bar{\nu}_e\to\bar{\nu}_e} \sim 0.1$. This goes against our assumption for the perturbative expansion where we have assumed $P^{(0)}_{\bar{\nu}_e\to\bar{\nu}_e} >> P^{(1)}_{\bar{\nu}_e\to\bar{\nu}_e} >> P^{(2)}_{\bar{\nu}_e\to\bar{\nu}_e}...$ We conclude that probability formulae are valid when $\sin^2 2\theta_{13}^{BF} \gtrsim 0.02$. For the part of the LIV parameter space where the $\sin^2 2\theta_{13}^{BF} \lesssim 0.02$ the assumptions used in the derivation of the survival probability are not met and the exclusion limits on LIV parameters may not be correct.

The higher perturbative orders have to be included in the probability in these regions of LIV parameter space. In that case, we will lose the linearity in LIV parameters where the LIV part of the survival probability in Eq.(3.12) is simple sum of each flavour combination $\bar{\alpha}\bar{\beta}$. That is indeed very nice feature, which works as a motivation for case-by-case where the contribution of particular SME parameters is independent on the other. This is no longer true for higher orders where we get among others for example terms like $P^{(2)}_{\bar{\nu}_e\to\bar{\nu}_e} \sim (a_L)^T_{\alpha\alpha}(a_L)^T_{\beta\beta}$ where $\alpha \neq \beta$. These terms posses intrinsic interference between SME parameters and considering only part of the parameters non-zero can lead to qualitative change of the oscillation formulae.

In what follows, we will keep using the expansion of the survival probability to

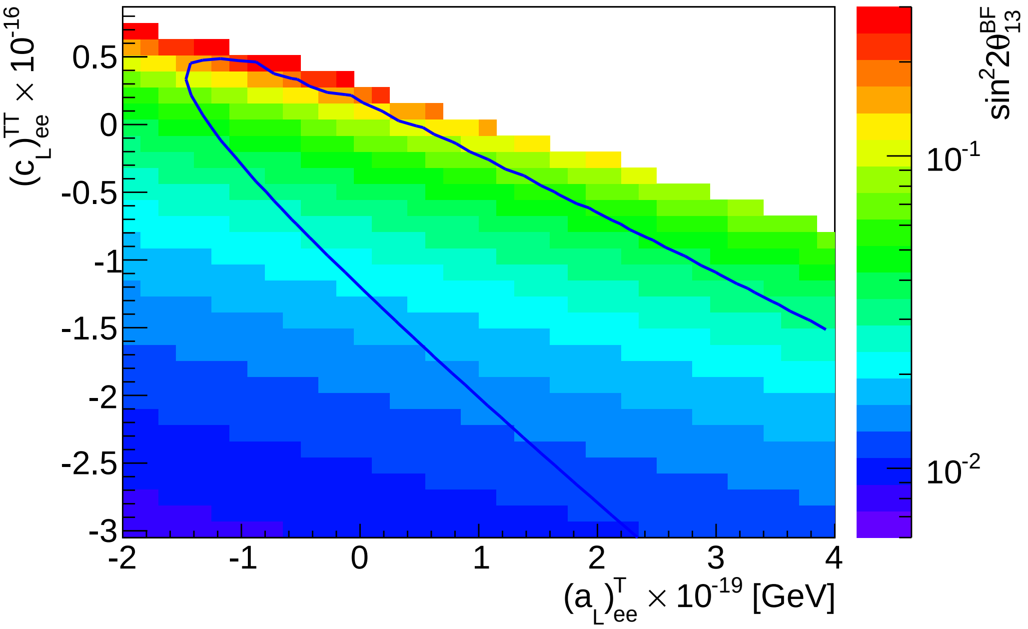

Figure 7.7: The $\sin^2 2\theta_{13}^{BF}$ as a function of SME parameters $(a_L)^T_{ee}$, $(c_L)^{TT}_{ee}$ for the ee case overlaid by the exclusion contours. The region for which $\sin^2 2\theta_{13}^{BF} \to 0$ overlaps with the region of open contours. The survival probability formula assumptions are broken here and the exclusion contours in this region cannot be trusted.

the first order in the LIV parameters. Nevertheless, we are aware of the limited validity of the survival probability thus we based our conclusion only on the regions where we can trust it.

7.2.4 Limits on the Standard-Model Extension Parameters using Case-by-case Formulae using Gaussian CL$_S$ Method

As we have shown in Sec.7.2.2, even only two SME parameters turned on in case-by-case formulae in Eqs.(3.21)-(3.26) do not allow us to set double sided limits on the LIV parameters. This can be done only for two out of six flavour combinations, namely $e\mu$ and $e\tau$. Those double-sided limits for case-by-case flavour combinations $e\mu$ and $e\tau$ with two non-zero SME parameters are shown in Tab.7.3. We compare the exclusion limits obtained by Daya Bay with previous measurement done by the Super-Kamiokande experiment (SK) [57]. SK considered only positive values of the SME parameters and therefore provided only upper limits. These limits are much more stringent than Daya Bay ones due to the longer baseline in SK. Nevertheless, in the current status, Daya Bay is the first experiment to provide lower limits on listed SME parameter.

Since we already turn on and off some SME parameters, in order to set double-sided exclusion limits we have decided to go even further and end up with having only one non-zero SME parameter at the time. This will result in the further re-

Coefficient	Previous lower limit	Previous upper limit	DB lower limit	DB upper limit
$\mathrm{Re}(a_L)^T_{e\mu}$	N/A	1.8×10^{-23} GeV [SK]	-7.59×10^{-20} GeV	5.44×10^{-20} GeV
$\mathrm{Re}(a_L)^T_{e\tau}$	N/A	4.1×10^{-23} GeV [SK]	-5.35×10^{-20} GeV	3.28×10^{-20} GeV
$\mathrm{Re}(c_L)^{TT}_{e\mu}$	N/A	8.0×10^{-27} [SK]	-4.65×10^{-18}	8.05×10^{-18}
$\mathrm{Re}(c_L)^{TT}_{e\tau}$	N/A	9.3×10^{-25} [SK]	-2.93×10^{-18}	6.50×10^{-18}

Table 7.3: Summary of upper and lower limits on 95% CL_S for SME parameters obtained by case-by-case formulae for flavour combinations $e\mu$ and $e\tau$ with two non-zero SME parameters $\mathrm{Re}(a_L)^T_{\alpha\beta}$, $\mathrm{Re}(c_L)^{TT}_{\alpha\beta}$. Normal neutrino mass hierarchy is assumed to be true. For comparison, we show previous limits obtained by the Super-Kamiokande experiment [57] (95% CL). The Super-Kamiokande experiment assumed only non-negative values of the parameters thus provided only upper limits.

duction of the case-by-case formulae shown in Eqs.(3.21)-(3.26) where we assume either $(a_L)^T_{\alpha\beta} = 0$, or $(c_L)^{TT}_{\alpha\beta} = 0$ when setting the limit for the complementary parameter. The limits for single parameter can be then illustratively viewed as a cross-section of the exclusion contours in Fig.7.5 and Fig.7.6 with the x-axis or y-axis respectively, although, they are determined from the CL_S profiles. The double-sided CL_S exclusion limits obtained by having only one non-zero SME parameter at the time are listed in Tab.7.4. Most of them are measured for the first time providing useful limits for the physics community as well as the benchmark for the future measurements.

7.2.5 Exclusion Limits for the X_i's using Full Formula Survival Probability

Although X_i's in the full formula survival probability in Eq.(3.32) are not exact SME coupling constants but their linear combinations, limits on effective parameters X_i's would constrain the overall effect of LIV. Similar to case-by-case, we use the Gaussian CL_S method to set the exclusion limits on X_i's. We have five free parameters: $\sin^2 2\theta_{13}$ and four LIV parameters X_1, X_2, X_3, X_4. We extract the exclusion limits for particular X_i from $\mathrm{CL_S}(X_i)$ profile, which is a function of this parameter. The profile is sampled by 50 points across the relevant interval of X_i values. On the contrary to case-by-case, we would like to stay as general as we could therefore we do not fix any of the other free parameters. The other LIV parameters as well as $\sin^2 2\theta_{13}$ are treated as unconstrained nuisance parameters therefore for each point we find and use their best-fit values based on the measured data. We can express that as:

$$CL_S(X_i) = CL_S(\sin^2 2\theta_{13}^{BF}(X_i), X_1^{BF}(X_i), ..., X_i, ..., X_4^{BF}(X_i)) \tag{7.13}$$

where the values for $\sin^2 2\theta_{13}^{BF}$ and $X_{j\neq i}^{BF}$ are obtained by χ^2 minimization on the measured data:

$$\chi^2_{min}(\sin^2 2\theta_{13}^{BF}, X_1^{BF}, ..., X_i, ..., X_4^{BF}) = \min_{\sin^2 2\theta_{13}, X_{j\neq i}^{BF}} \chi^2(\sin^2 2\theta_{13}, X_1, ..., X_i, ..., X_4) \tag{7.14}$$

We encounter however the same issue as in the case-by-case analysis. We eventually end up with the small values of $\sin^2 2\theta_{13}^{BF}$. For such values our as-

Coefficient	Previous lower limit	Previous upper limit	DB lower limit	DB upper limit
$(a_L)^T_{ee}$	N/A	N/A	-1.26×10^{-19} GeV	0.42×10^{-19} GeV
$(a_L)^T_{\mu\mu}$	N/A	N/A	-0.69×10^{-19} GeV	1.63×10^{-19} GeV
$(a_L)^T_{\tau\tau}$	N/A	N/A	-0.52×10^{-19} GeV	3.26×10^{-19} GeV
$\mathrm{Re}(a_L)^T_{e\mu}$	N/A	1.8×10^{-23} GeV [SK]	-1.40×10^{-20} GeV	2.06×10^{-20} GeV
$\mathrm{Re}(a_L)^T_{e\tau}$	N/A	4.1×10^{-23} GeV [SK]	-1.19×10^{-20} GeV	1.97×10^{-20} GeV
$\mathrm{Re}(a_L)^T_{\mu\tau}$	N/A	6.5×10^{-24} GeV [SK]	-0.42×10^{-19} GeV	1.27×10^{-19} GeV
$(c_L)^{TT}_{ee}$	N/A	N/A	-1.20×10^{-16}	0.16×10^{-16}
$(c_L)^{TT}_{\mu\mu}$	N/A	N/A	-0.27×10^{-16}	0.88×10^{-16}
$(c_L)^{TT}_{\tau\tau}$	N/A	N/A	-0.20×10^{-16}	N/A
$\mathrm{Re}(c_L)^{TT}_{e\mu}$	N/A	8.0×10^{-27} [SK]	-0.92×10^{-18}	2.01×10^{-18}
$\mathrm{Re}(c_L)^{TT}_{e\tau}$	N/A	9.3×10^{-25} [SK]	-1.08×10^{-18}	2.34×10^{-18}
$\mathrm{Re}(c_L)^{TT}_{\mu\tau}$	N/A	4.4×10^{-27} [SK]	-0.18×10^{-16}	1.21×10^{-16}

Table 7.4: Summary of upper and lower exclusion limits on 95% $\mathrm{CL_S}$ for SME parameters set by Daya Bay experiment (DB) obtained by using reduced case-by-case formulae when only one SME parameter is considered to be non-zero at the time. Normal neutrino mass hierarchy is assumed to be true. For comparison, we show previous limits the Super-Kamiokande experiment [57] (95% CL). Let us note that Super-Kamiokande assumed only non-negative values of the parameters thus provided only upper limits.

sumptions, which were used in the derivation of the survival probability, are not valid thus the probability formula cannot be trusted. Similar to the discussion in Sec.7.2.3, for the values of $\sin^2 2\theta_{13}^{BF} \lesssim 0.02$ the short baseline oscillations observed in Daya Bay are driven by the LIV term in the Eq.(3.32), which is in the contradiction with our assumption $P^{(0)}_{\bar{\nu}_e\to\bar{\nu}_e} >> P^{(1)}_{\bar{\nu}_e\to\bar{\nu}_e} >> P^{(2)}_{\bar{\nu}_e\to\bar{\nu}_e}...$ we have used in the derivation of the formula.

Moreover, for $\sin^2 2\theta_{13}^{BF} \lesssim 0.02$, it is no longer true that oscillation effects due to Δm^2_{21} in LIV part of the probability can be neglected. It turns out that terms in Eq.(3.27) proportional to $f(\Delta m^2_{32})$ or $f(\Delta m^2_{31})$ are suppressed at least by the factor of $\sin^2\theta_{13}$ while terms proportional to $f(\Delta m^2_{21})$ are not effected. Since terms proportional to $f(\Delta m^2_{32})$ or $f(\Delta m^2_{31})$ have to create the oscillation effect even being suppressed by small value of $\sin^2\theta_{13}$, the values of LIV parameters must be large. But such a large LIV parameters makes the contribution of small terms proportional to $f(\Delta m^2_{21})$ large enough that they are comparable in amplitude with $f(\Delta m^2_{32})$ terms. Therefore the full formula for which we assume $\Delta m^2_{21} \to 0$ in not correct for $\sin^2 2\theta_{13}^{BF} \lesssim 0.02$.

Let us now look on the exclusion limits for X_i's parameters. The $\mathrm{CL_S}$ profiles as well as the best-fit $\sin^2 2\theta_{13}^{BF}$ are shown in Fig.7.8. We can see that for each X_i we can set only upper, or lower exclusion limit. For the complementary one, we always end up with $\sin^2 2\theta_{13}^{BF} \lesssim 0.02$ which is the region where is our survival probability formula invalid.

From the $\mathrm{CL_S}$ profiles profiles shown in Fig.7.8 we obtained 95% $\mathrm{CL_S}$ exclusion limits for X_i's which are listed in Tab.7.5.

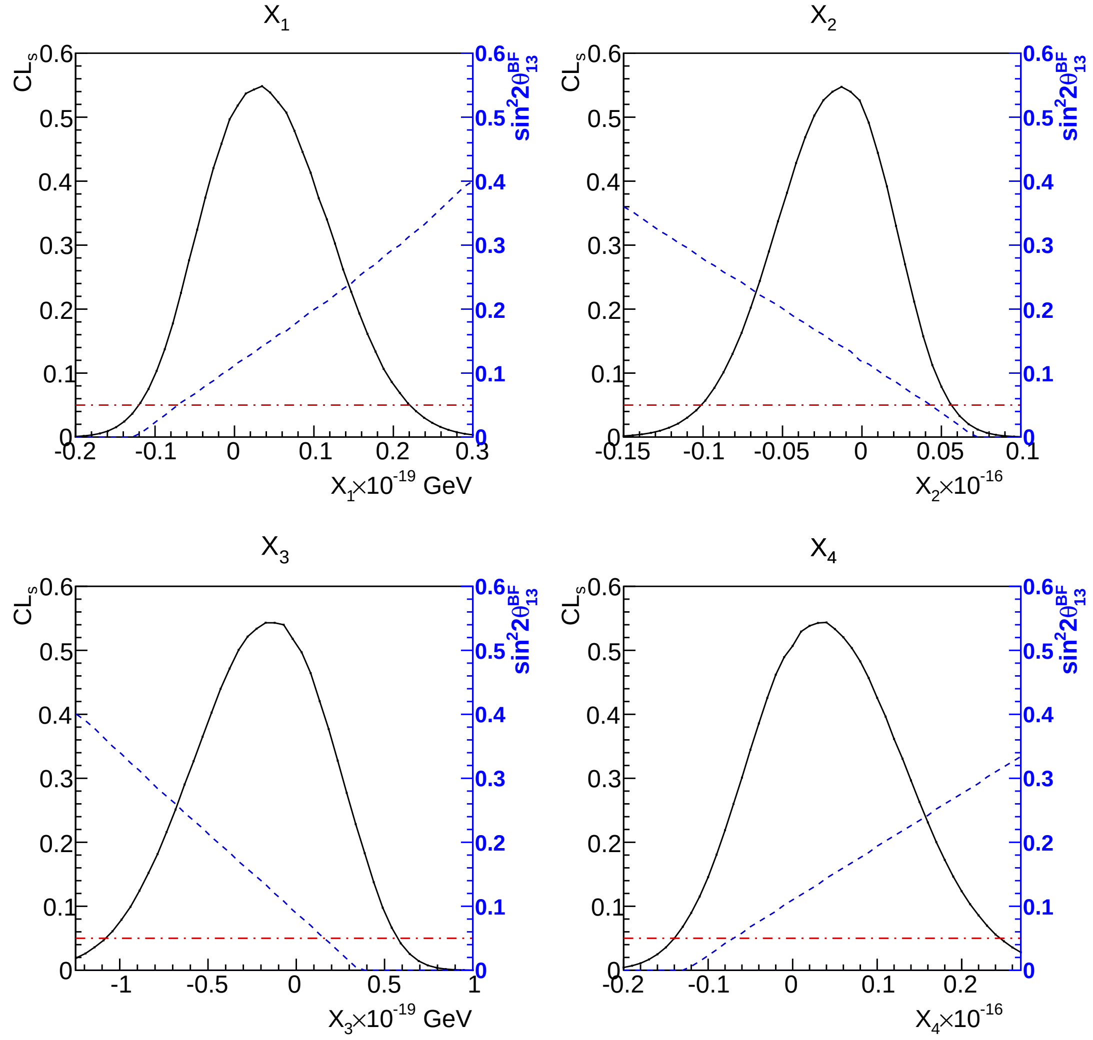

Figure 7.8: The $\mathrm{CL_S}$ profiles (solid black) as well as $\sin^2 2\theta_{13}^{BF}$ (dashed blue) for four LIV parameters X_i (i=1,2,3,4) from full formula in Eq.(3.32). The red dash-dotted line represents the 95% $\mathrm{CL_S}$ limit, i.e. $\mathrm{CL}_S = 0.05$. For each parameter X_i for either upper or lower limit we get $\sin^2 2\theta_{13}^{BF} \to 0$. That violates the assumptions we used in the probability derivation and these limits cannot be trusted.

	Normal Hierarchy		Inverted Hierarchy	
	Upper limit	Lower limit	Upper limit	Lower limit
X_1	N/A	0.221×10^{-19} GeV	-0.221 $\times 10^{-19}$ GeV	N/A
X_2	-0.101×10^{-16}	N/A	N/A	0.101×10^{-16}
X_3	-1.08×10^{-19} GeV	N/A	N/A	1.08×10^{-19} GeV
X_4	N/A	0.246×10^{-16}	-0.246×10^{-16}	N/A

Table 7.5: Summary of upper or lower exclusion limits on 95% CLs for LIV parameters X_i's for normal (NH) and inverted (IH) neutrino mass hierarchy. The limits for IH are opposite to the limits for NH. Only one limit is available at the time since the probability formula is not valid for the complementary.

7.2.6 Results in the Case of Inverted Hierarchy

The probabilities with LIV effect depend on the choice of the hierarchy. Up to now, we have assumed normal hierarchy to be true. In this section, we discuss the results for the inverted hierarchy.

We can use effective mass square difference Δm^2_{ee} in the case of LIV since it still holds that the Daya Bay experiment is not able to distinguish between mass squared differences Δm^2_{31} and Δm^2_{32}. Thus with the different hierarchy, we have to change $\Delta m^2_{ee} \to -\Delta m^2_{ee}$ in the oscillation probability formulae.

In case of full formula survival probability, the exclusion limits for inverted hierarchy can be directly derived from those obtained for the normal hierarchy. In the survival probability in Eq.(3.32), the term $P^{(0)}_{\bar{\nu}_e \to \bar{\nu}_e}$ corresponds to standard oscillation probability which is independent on the mass hierarchy. Although it contains the effective mass squared difference Δm^2_{ee} the exact dependence on $\sin^2 \frac{\Delta m^2_{ee} L}{4E}$ makes in independent on sign of Δm^2_{ee}. On the contrary, the term $P^{(1)}_{\bar{\nu}_e \to \bar{\nu}_e}$ contains two energy and distance dependancies $\sin \frac{\Delta m^2_{ee} L}{2E}$ and $\frac{\sin^2 \frac{\Delta m^2_{ee} L}{4E}}{\frac{\Delta m^2_{ee} L}{4E}}$. They are both odd functions of Δm^2_{ee}. The change of hierarchy assumption corresponds to $\Delta m^2_{ee} \to -\Delta m^2_{ee}$, which results in $P^{(1)}_{\bar{\nu}_e \to \bar{\nu}_e} \to -P^{(1)}_{\bar{\nu}_e \to \bar{\nu}_e}$. The same can be achieved by change $X_i \to -X_i$, which also results in $P^{(1)}_{\bar{\nu}_e \to \bar{\nu}_e} \to -P^{(1)}_{\bar{\nu}_e \to \bar{\nu}_e}$. At the end, exclusion limits for full formula effective parameters X_i's with inverted hierarchy to be true are simply numbers with opposite signs to those obtained with the assumption of the normal hierarchy, see Tab.7.5.

For the case-by-case oscillation probabilities listed in Eqs.(3.21)-(3.26), the situation is more complicated. In addition to the odd functions of Δm^2_{ee} which would lead to the opposite exclusion limits, the LIV term $P^{(1)}_{\bar{\nu}_e \to \bar{\nu}_e}$ contains terms with Δm^2_{21} which is independent on the mass hierarchy. The contribution of these terms is small but zero. The exclusion limits for the inverted hierarchy are expected to be close to the opposite values obtained for the normal hierarchy with small deviations due to the terms containing Δm^2_{21}. The illustration is shown in Fig.7.9 where we show the 95% $\mathrm{CL_S}$ exclusion contours for the *ee* case for two possible hierarchies. The contours agree pretty well taking into account opposite sign of the LIV parameters, note two set of the axes.

The deviation from exact opposite values is linked to the region with small values of $\sin^2 2\theta^{BF}_{13}$. Such small values enhance the effect of Δm^2_{21}-driven oscillations since they suppress the terms Δm^2_{ee}, see discussion in Sec.7.2.3.

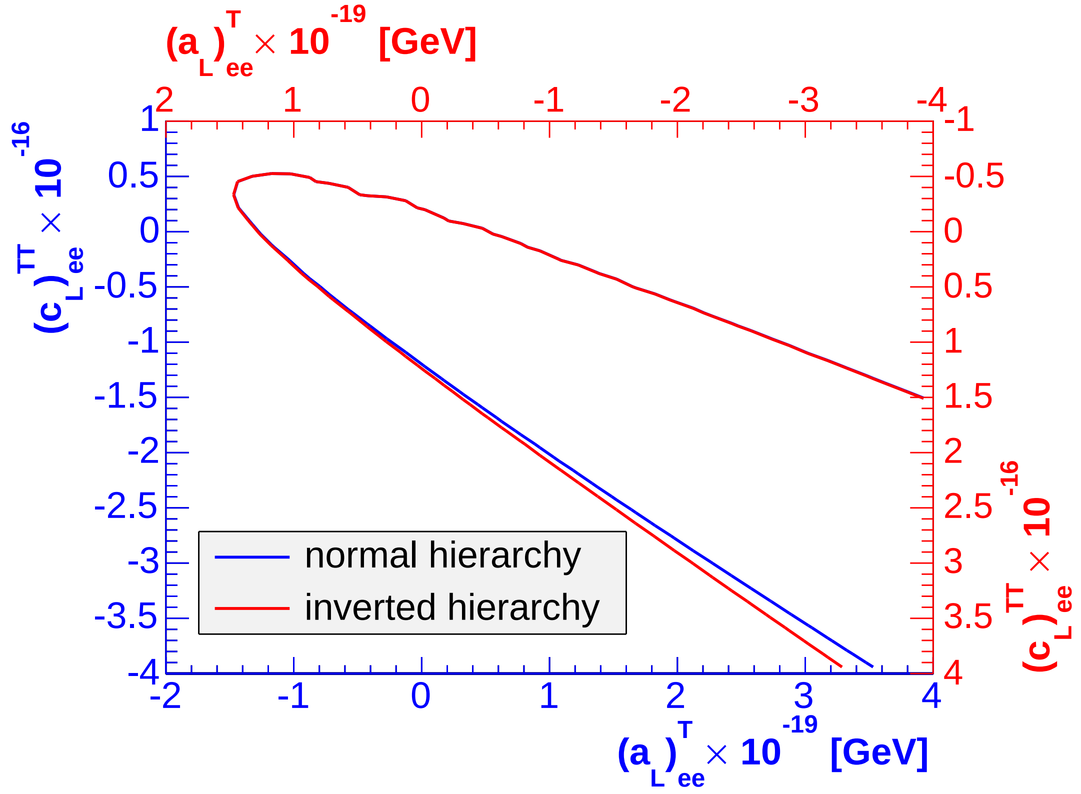

Figure 7.9: Comparison of 95% CL_S exclusion contours for normal (blue) and inverted (red) hierarchy for *ee* case. The contours are almost similar taking the opposite values of LIV parameters for inverted hierarchy. The small difference linked to the low values of $\sin^2 2\theta_{13}^{BF}$ can be observed.

In conclusion, the exclusion limits for inverted hierarchy for most of the cases have just the opposite sign with respect to the limits for normal hierarchy (or they are very similar). The only exception is $\mu\mu$ case for inverted hierarchy which exhibits the behaviour of $\tau\tau$ case for the normal hierarchy and we can set only upper limit on $(c_L)^{TT}_{\mu\mu}$. On the contrary, $\tau\tau$ case for the inverted hierarchy behaves normally. The 95% CL_S exclusion limits for inverted hierarchy are presented in Tab.7.6. We conclude that for both hierarchies the limits obtained by case-by-case analysis are in the same ballpark with only slight variations.

7.3 Search for Non-standard Interactions

In this section, we present second investigated scenario of physics BSM, which is the presence of Non-standard Interactions (NSIs). The NSIs in the source or the detector would modify the survival probability. To describe such an effect we use the oscillation probability in Eq.(4.35) where we additionally introduce the effective mass squared splitting Δm^2_{ee} discussed before. Then we get formula:

$$\begin{aligned} P^{DB}_{\bar{\nu}_e\to\bar{\nu}_e} &= (a+b)^2 - \sin^2 2\theta_{12} a^2 \sin^2 \frac{\Delta m^2_{21} L}{4E} \\ &\quad - 4ab \sin^2\left(\frac{\Delta m^2_{ee} L}{4E} - \frac{\Delta\phi}{2}\right) \end{aligned} \tag{7.15}$$

Coefficient	Previous lower limit	Previous upper limit	DB lower limit	DB upper limit
$(a_L)^T_{ee}$	N/A	N/A	-0.42×10^{-19} GeV	1.27×10^{-19} GeV
$(a_L)^T_{\mu\mu}$	N/A	N/A	-6.42×10^{-19} GeV	1.02×10^{-19} GeV
$(a_L)^T_{\tau\tau}$	N/A	N/A	-1.65×10^{-19} GeV	0.69×10^{-19} GeV
$\mathrm{Re}(a_L)^T_{e\mu}$	N/A	1.8×10^{-23} GeV [SK]	-1.96×10^{-20} GeV	1.19×10^{-20} GeV
$\mathrm{Re}(a_L)^T_{e\tau}$	N/A	4.1×10^{-23} GeV [SK]	-2.06×10^{-20} GeV	1.38×10^{-20} GeV
$\mathrm{Re}(a_L)^T_{\mu\tau}$	N/A	6.5×10^{-24} GeV [SK]	-1.27×10^{-19} GeV	0.42×10^{-19} GeV
$(c_L)^{TT}_{ee}$	N/A	N/A	-0.16×10^{-16}	1.23×10^{-16}
$(c_L)^{TT}_{\mu\mu}$	N/A	N/A	N/A	0.39×10^{-16}
$(c_L)^{TT}_{\tau\tau}$	N/A	N/A	-0.90×10^{-16}	0.27×10^{-16}
$\mathrm{Re}(c_L)^{TT}_{e\mu}$	N/A	8.0×10^{-27} [SK]	-2.34×10^{-18}	1.08×10^{-18}
$\mathrm{Re}(c_L)^{TT}_{e\tau}$	N/A	9.3×10^{-25} [SK]	-2.00×10^{-18}	0.92×10^{-18}
$\mathrm{Re}(c_L)^{TT}_{\mu\tau}$	N/A	4.4×10^{-27} [SK]	-1.21×10^{-16}	0.18×10^{-16}

Table 7.6: Summary of upper and lower exclusion limits on 95% $\mathrm{CL_S}$ for SME parameters set by Daya Bay experiment (DB) obtained by using reduced case-by-case formulae when only one SME parameter is considered to be non-zero at the time. This time, inverted neutrino mass hierarchy is assumed to be true. For comparison, we show previous limits the Super-Kamiokande experiment [57] (95% CL). Again, let us note that Super-Kamiokande assumed only non-negative values of the parameters thus provided only upper limits.

with four free parameters: Δm^2_{ee}, a, b and $\Delta\phi$. Unlike for the LIV analysis, we in general do not constrain Δm^2_{ee} and treat it as a free parameter, although we eventually use constraints as well. What is similar is the dependence on the mass hierarchy. If we look to the oscillation probability in Eq.(7.15), the Δm^2_{ee} changes the sign assuming the other hierarchy while $\Delta\phi$ is hierarchy independent. First, we assume normal mass hierarchy to be true and discuss the results for the inverted hierarchy later.

7.3.1 Parameters to Constrain

Our oscillation analysis is performed using a relative near-far measurement. As we have discussed before in Sec.5.1, this brings many advantages in the reduction of systematic uncertainties. However, it prevents us to set limits on all parameters in Eq.(7.15), i.e. a, b, m^2_{ee} and $\Delta\phi$. Let us now explain why it is so and which parameters can be constrained.

For better illustration, we start with the approximate probability formula, similar to Eq.(7.15), derived in two-neutrino framework. The probability takes form of:

$$P^{2\nu}_{\bar{\nu}_e \to \bar{\nu}_e} = (a+b)^2 - 4ab \sin^2\left(\frac{\Delta m^2 L}{4E} - \frac{\Delta\phi}{2}\right) \tag{7.16}$$

where Δm^2 is the only mass squared difference present in two neutrino framework.

The parameters a and b are defined as:

$$\begin{aligned} a &= \frac{A^s A^d}{\sqrt{({A^s}^2 + {B^s}^2)({A^d}^2 + {B^d}^2))}} \\ b &= \frac{B^s B^d}{\sqrt{({A^s}^2 + {B^s}^2)({A^d}^2 + {B^d}^2))}} \end{aligned} \tag{7.17}$$

where $A^{s/d}$ and $B^{s/d}$ are elements of in general non-unitary mixing matrix:

$$M_{2\nu} = \begin{pmatrix} A & B \\ C & D \end{pmatrix} \tag{7.18}$$

For the relative near-far measurement of the shape of the energy spectrum

- We can constrain Δm^2 due to its relevance to the energy-dependent oscillation frequency.
- We can constrain the common phase shift $\Delta\phi$ as a energy-independent oscillation frequency.
- We can constrain parameter combination $4ab$ since it is the amplitude of the disappearance effect (for explanation, in standard oscillations this term takes form of $\sin^2 2\theta$).
- We cannot constrain the absolute term $(a+b)^2$ since we perform relative measurement

This leaves us with only one constraint for two parameters a and b. Therefore, we cannot set limits on those. In the end, we can set limits only on the standard parameter Δm^2 and NSI parameter $\Delta\phi$.

Let us note that change of the absolute term is effectively equivalent to the change in the absolute antineutrino flux. The near-far measurement is not sensitive to the absolute flux since only relative difference between near and far measurements matters, which we have already discussed in Sec.5.1.

The situation does not change much for survival probability in three-neutrino framework, see Eq.(7.15). Again, we can set constraints on Δm^2_{ee}, $\Delta\phi$ and oscillation amplitude $4ab$. In addition, we could get a constraint on the medium baseline oscillation amplitude $\sin^2 2\theta_{12} a^2$ standing in front of the term $\sin^2 \frac{\Delta m^2_{21} L}{4E}$. That would provide us constraint on parameter a which could be then used to constrain also parameter b. However, Daya Bay measurement is only very little sensitive to the medium baseline oscillations. The standard oscillation effect due to the term containing Δm^2_{21} in the Daya Bay Far Hall for typical reactor antineutrino energy $E_{\bar{\nu}}$=3.5 MeV is less than 0.2%. This is already very small and any deviation due to the presence of NSIs expressed by a^2 is beyond Daya Bay resolution.

Hence we conclude that relative near-far measurement can provide constraints only on NSI parameter $\Delta\phi$ together with mass squared splitting Δm^2_{ee}.

7.3.2 Limits on $\Delta\phi$ with Unconstrained Δm^2_{ee}

In order to set limits on parameters $\Delta\phi$ and Δm^2_{ee} we have performed Wilks' CI analysis, see Sec.6.2.2. We assumed that $\Delta\chi^2$ parent distribution in χ^2-distributed. The parameters a and b are treated as a nuisance parameters and we minimize over them. The relevant $\Delta\chi^2$ function is according to Eq.(6.30):

$$\Delta\chi^2(\Delta m^2_{ee}, \Delta\phi) = \min_{a,b} \chi^2(a, b, \Delta m^2_{ee}, \Delta\phi) - \chi^2_{BF} \tag{7.19}$$

with 2 DoF.

Fig.7.10 shows the best-fit point $\Delta m^2_{ee} = 3.25 \times 10^{-3}$ eV^2 and $\Delta\phi = 0.9$ and 95% confidence level contours for Δm^2_{ee} and $\Delta\phi$. We can observe correlation between these two parameters. This is expected since Δm^2_{ee} and $\Delta\phi$ are connected by the term $\left(\frac{\Delta m^2 L}{4E} - \frac{\Delta\phi}{2}\right)$ in Eq.(7.15) which express the effective overall oscillation frequency.

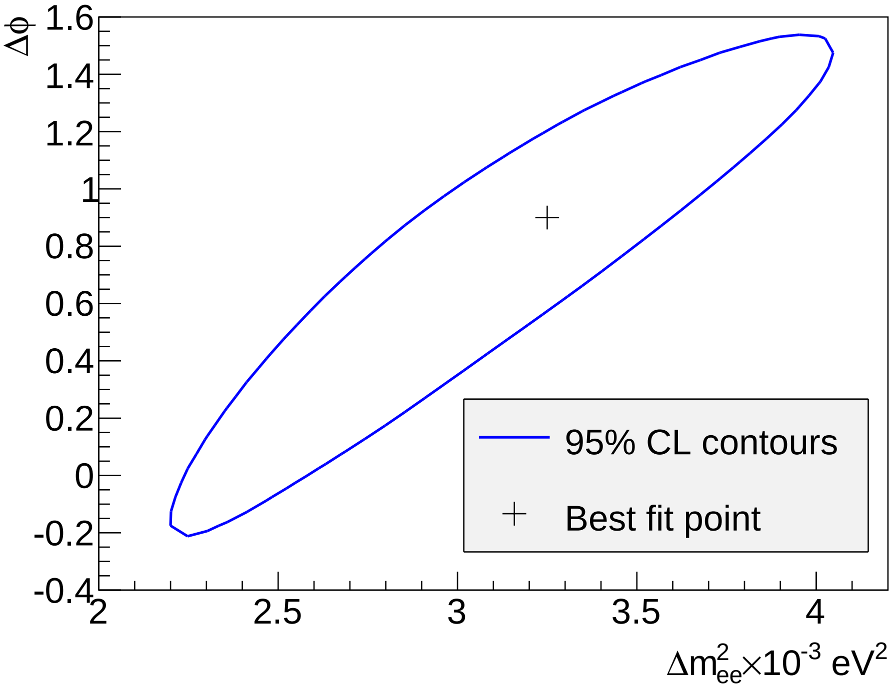

Figure 7.10: The 95% confidence level contours for Δm^2_{ee} and $\Delta\phi$ and the best-fit point $\Delta m^2_{ee} = 3.25 \times 10^{-3}$ eV^2 and $\Delta\phi = 0.9$.

We as well get limits on single parameters Δm^2_{ee} and $\Delta\phi$ using $\Delta\chi^2_{\Delta m^2}$ and $\Delta\chi^2_{\Delta\phi}$ defined as:

$$\begin{aligned} \Delta\chi^2_{\Delta m^2}(\Delta m^2_{ee}) &= \min_{a,b,\Delta\phi} \chi^2(a, b, \Delta m^2_{ee}, \Delta\phi) - \chi^2_{BF} \\ \Delta\chi^2_{\Delta\phi}(\Delta\phi) &= \min_{a,b,\Delta m^2_{ee}} \chi^2(a, b, \Delta m^2_{ee}, \Delta\phi) - \chi^2_{BF} \end{aligned} \tag{7.20}$$

which both have 1 DoF. The $\Delta\chi^2_{\Delta m^2}$ and $\Delta\chi^2_{\Delta\phi}$ profiles are shown in Fig.7.11. The interval of possible values of parameter Δm^2_{ee} is now broaden with respect

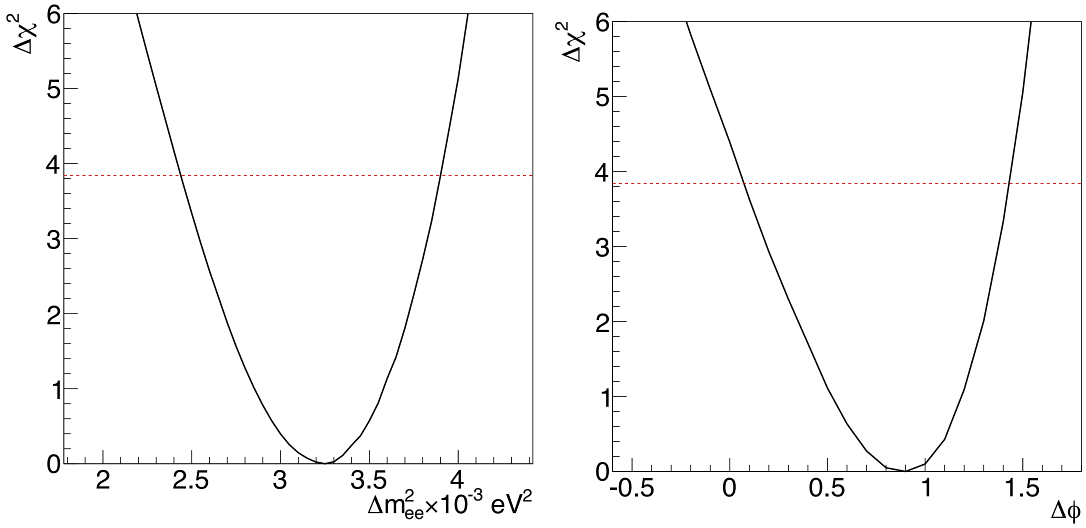

Figure 7.11: Left: The $\Delta\chi^2_{\Delta m^2}(\Delta m^2_{ee})$ profile with the indication of 95% CL limit (red dashed line). Right: The $\Delta\chi^2_{\Delta\phi}(\Delta\phi)$ profile with the indication of 95% CL limit (red dashed line).

to the case without NSIs due to large correlation with $\Delta\phi$. The value of effective mass squared difference is in the case of NSIs $\Delta m^2_{ee} = (3.25^{+0.33}_{-0.40}) \times 10^{-3}$ eV^2 at 68.3% CL. That is significantly higher then the result of the standard oscillations $|\Delta m^2_{ee}| = 2.42 \times 10^{-3}$ eV^2 from Eq.(7.7). The shift in Δm^2_{ee} is compensated by the non-zero value of NSIs phase with best-fit value $\Delta\phi_{BF} = 0.9$. We obtained wide interval of values for $\Delta\phi$ parameter around this central value., see Tab.7.7. For the standard oscillations expressed by $\Delta\phi = 0$ we got $\Delta\chi^2_{\Delta\phi}(0) = 4.39$. That can be translated as the more than 2σ deviation from the standard oscillations without NSIs. The $\Delta\chi^2$ value corresponds to the p-value of 0.036.

The value of the effective mass squared difference $|\Delta m^2_{ee}| = 2.42 \times 10^{-3}$ eV^2 obtained in Daya Bay assuming standard oscillations without NSIs agrees with the measurements performed by other experiments. The comparison of their results with Daya Bay is shown in Fig.7.12 for fundamental parameter $|\Delta m^2_{32}|$. The values are compatible with each other suggesting that above presented shifted value of Δm^2_{ee} in case of NSIs is more result of strong correlation with $\Delta\phi$ less than presence of NSIs.

7.3.3 Limits on $\Delta\phi$ with constrained Δm^2_{ee}

Since the value of mass squared difference Δm^2_{ee} was confirmed by other experiments we have to constrain it based on these measurements. We will do it the same way as in the search for LIV presented in Sec.7.2. We fix the value of mass squared difference on $\Delta m^2_{ee} = (2.48 \pm 0.07) \times 10^{-3}$ eV^2 and include the effects of its uncertainty in the additional contribution to the covariance matrix $V_{\Delta m^2}$.

Then we can again use CI to set limits on $\Delta\phi$ while Δm^2_{ee} is fixed and a and b are treated as unconstrained nuisance parameters. The appropriate $\Delta\chi^2_{\Delta m^2 fix}$ function is according to Eq.(6.30):

$$\Delta\chi^2_{\Delta m^2 fix}(\Delta\phi) = \min_{a,b} \chi^2(a, b, \Delta m^2_{ee} = (2.48 \pm 0.07) \times 10^{-3} \text{ eV}^2, \Delta\phi) - \chi^2_{BF} \quad (7.21)$$

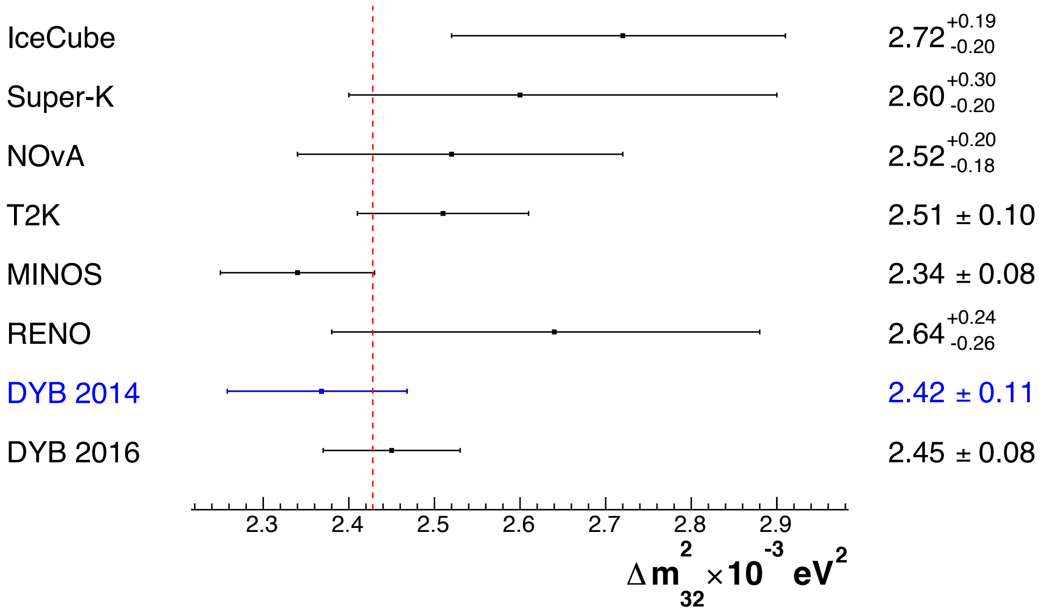

Figure 7.12: The comparison of the measurements of $|\Delta m^2_{32}|$ performed by various experiments. All results assume normal mass hierarchy. There are results determined from reactor $\bar{\nu}_e$ disappearance done by Daya Bay and RENO [85]. We show most recent Daya Bay results from year 2016 [36] as well as result for the data set used in this analysis from published in 2014 [59] (blue point) from Eq.(7.7) which was recalculated to the value of $|\Delta m^2_{32}|$. We show the results of MINOS [82], T2K [83] and NOvA [86] experiments obtained by the measurement of accelerator ν_μ disappearance. We include also results from Super-Kamiokande [87] and IceCube [88] experiments based on the atmospheric ν_μ disappearance. The red dashed line indicates the value $|\Delta m^2_{32}| = 2.43 \times 10^{-3}$ eV^2 which is the value of eventually fixed parameter Δm^2_{ee}.

with 1 DoF where

$$\chi^2_{BF} = \min_{a,b,\Delta\phi} \chi^2(a, b, \Delta m^2_{ee} = (2.48 \pm 0.07) \times 10^{-3} \text{ eV}^2, \Delta\phi) \tag{7.22}$$

The $\Delta\chi^2_{\Delta m^2 fix}$ profile as a function of $\Delta\phi$ is shown in Fig.7.13. The best-fit value is $\Delta\phi_{BF} = 0.135$. The $\Delta\phi = 0$ point corresponds to $\Delta\chi^2(0) = 0.744$ with corresponding p-value 0.39. The independent knowledge of Δm^2_{ee} radically changes the limits on NSIs parameter $\Delta\phi$. This time, we do not observe any significant deviation from standard oscillations with three-neutrino flavours.

As we have discussed before, we can constrain the combination of parameters $4ab$, however, we are not able with the relative near-far measurement constrain the single parameters a and b. Nevertheless, it does not have any effect on the final $\Delta\phi$ limits. In order to demonstrate that we fix either a or b to certain value

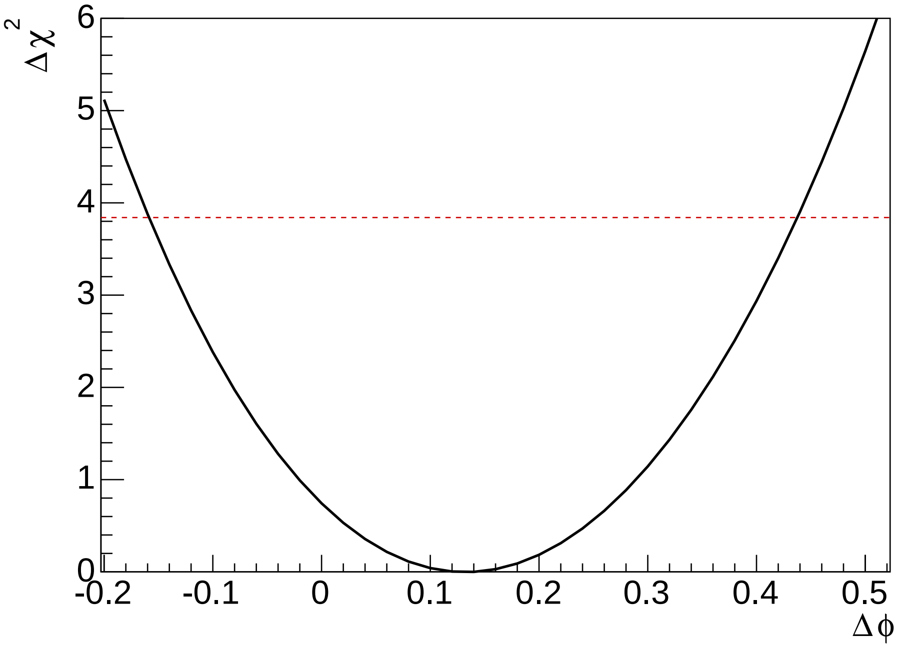

Figure 7.13: The $\Delta\chi^2_{\Delta m^2 fix}$ profile as a function of $\Delta\phi$. The red dashed line indicates the 95% CL limit.

and perform CI analysis based on one of

$$\begin{aligned}\Delta\chi^2_a(\Delta\phi) &= \min_a \chi^2(a_{fix}, b, \Delta m^2_{ee} = (2.48 \pm 0.07) \times 10^{-3}\ \mathrm{eV}^2, \Delta\phi) - \chi^2_{BFa}\\ \Delta\chi^2_b(\Delta\phi) &= \min_b \chi^2(a, b_{fix}, \Delta m^2_{ee} = (2.48 \pm 0.07) \times 10^{-3}\ \mathrm{eV}^2, \Delta\phi) - \chi^2_{BFb}\end{aligned} \tag{7.23}$$

where

$$\begin{aligned}\chi^2_{BFa} &= \min_{b,\Delta\phi} \chi^2(a_{fix}, b, \Delta m^2_{ee} = (2.48 \pm 0.07) \times 10^{-3}\ \mathrm{eV}^2, \Delta\phi)\\ \chi^2_{BFb} &= \min_{a,\Delta\phi} \chi^2(a, b_{fix}, \Delta m^2_{ee} = (2.48 \pm 0.07) \times 10^{-3}\ \mathrm{eV}^2, \Delta\phi)\end{aligned} \tag{7.24}$$

The results are shown in Fig.7.14. We can see that $\Delta\chi^2$ profiles are independent on the chosen values of either a or b. Our limits for $\Delta\phi$ are therefore generally valid.

We illustrated the independence of $\Delta\phi$ limits on parameters a and b for analysis with constrained value of effective mass square difference Δm^2_{ee}, nevertheless, this independence is qualitatively the same also in the case of unconstrained Δm^2_{ee}.

7.3.4 Results for Inverted Mass Hierarchy

The NSIs probability dependence in Eq.(7.15) on neutrino mass hierarchy is hidden in the argument $\left(\frac{\Delta m^2_{ee} L}{4E} - \frac{\Delta\phi}{2}\right)$. With the change of the hierarchy from normal to inverted we get

$$\left(\frac{\Delta m^2_{ee} L}{4E} - \frac{\Delta\phi}{2}\right) \rightarrow \left(-\frac{\Delta m^2_{ee} L}{4E} - \frac{\Delta\phi}{2}\right) \tag{7.25}$$

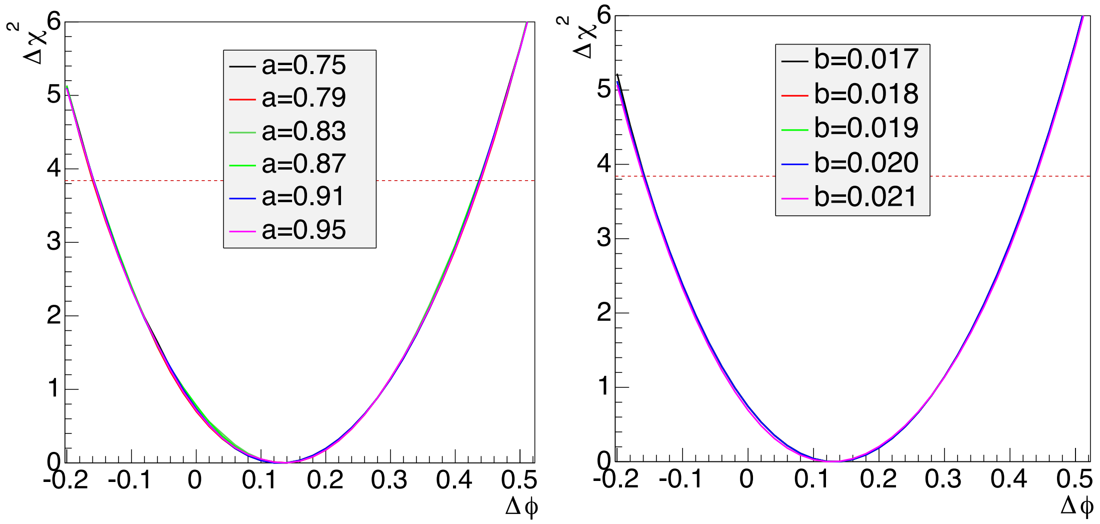

Figure 7.14: Left: The $\Delta\chi^2_a$ profiles as a function of $\Delta\phi$ for different values of parameter a. Right: The $\Delta\chi^2_b$ profiles as a function of $\Delta\phi$ for different values of parameter b. In both cases, the resulting limits for $\Delta\phi$ are basically independent on the choice of a or b and the curves for different choices of those parameters lie on the top of each other.

which is for the survival probability in Eq.(7.15) equivalent to the change:

$$\left(\frac{\Delta m^2_{ee}L}{4E} - \frac{\Delta\phi}{2}\right) \rightarrow \left(\frac{\Delta m^2_{ee}L}{4E} + \frac{\Delta\phi}{2}\right) \tag{7.26}$$

Therefore limits on $\Delta\phi$ for the normal mass hierarchy are same as the limits on $-\Delta\phi$ for inverted mass hierarchy.

7.3.5 Summary of Limits on Non-standard Interactions Parameter $\Delta\phi$

The summary of the allowed values of NSIs parameter $\Delta\phi$ using relative near-far measurement is shown in Tab.7.7. The table shows the 95% CL limits as well as the best-fit values. The limits are divided in to two categories based on whether we use Δm^2_{ee} constraints from other experiments or just pure Daya Bay data with unconstrained effective mass squared difference. Furthermore, in each category we present results assuming normal and inverted mass hierarchy. We should note that values for the inverted hierarchy are simply the opposite values for the normal hierarchy due to the structure of the survival probability in Eq.(7.15).

We must note that comparison with previous limits on common approach parameters [60] described in Sec.4.1 is quite hard. Due to the different approach in the introduction of NSIs we end up with different sets of parameters, which is not trivial to match to each other. Especially for the common approach, there are always several parameters while in our own phenomenological description we end up at maximum with four free parameters. Therefore matching the limits require further assumptions on common approach parameters. In conclusion we consider our limits complementary to the previously obtained limits [60].

		$\Delta\phi$		
		Lower limit (95%CL)	Best fit	Upper limit (95%CL)
Δm^2_{ee} unconstrained	NH	0.07	0.91	1.43
	IH	-1.43	-0.91	-0.07
Δm^2_{ee} constrained	NH	-0.159	0.135	0.438
	IH	-0.438	-0.135	0.159

Table 7.7: The summary of the allowed values as well as the best fit for NSIs parameter $\Delta\phi$. The lower and upper limit corresponds to 95% CL. The result depends on the option whether we used Δm^2_{ee} constraints or keep the mass squared difference free. For each option we present results assuming normal hierarchy (NH), or inverted hierarchy (IH) to be true, however, the values are just opposite for the other hierarchy. Note that the unconstrained mass squared difference value is far from the standard three-neutrino oscillations result.

7.3.6 Discussion about Constrained Absolute Antineutrino Flux

In order to set limits on all NSIs parameters in Eq.(7.15) including a and b we have to use absolute antineutrino flux constraints since only then we can limit the absolute term in the oscillation probability. There are various models [89], [90], [91], [92], [93], [94], which can provide the prediction based on the nuclear reactor power, fuel composition, burn-up etc.

The measurements of absolute antineutrino flux in the short baselines were done in the past. It turned out that the measurements are consistently lower than the model predictions. This gave rise to the phenomenon called “Reactor Anomaly” which was observed in many experiments including Daya Bay [95], [96]. The Fig.7.15 shows the previous measurements corrected for the three-neutrino oscillations and normalized to the prediction of Huber+Mueller model [89], [90]. The anomaly is observed already at distances of the order of $\mathcal{O}(10\text{ m})$.

The “Reactor Anomaly” is often consider to be an effect of the oscillations with new so-called sterile neutrino added to the standard three-neutrino framework, nevertheless, NSIs can serve as an equally good explanation. Both scenarios can eventually end up in the measured flux being lower than the prediction.

The common remedy to the anomaly suggests the existence of fourth neutrino mass state with mass squared difference at least $\Delta m^2 \approx \mathcal{O}(1\text{ eV})$ which together with the standard three mass states can create forth flavour state. This state is called sterile since it does not participate in the weak interaction. Such a mass squared difference results in the very rapid oscillations with the oscillation length lower than 10 m. Small oscillation length is hard to observe since the source and detector has similar dimension and thus the oscillations effectively average out resulting in the deficit in the measurement over prediction.

Nevertheless, NSIs can serve as an alternative explanation as well since they can cause the deficit in the flux measurement. This effect is linked to the absolute term in the probability in Eq.(7.15). The non-unitarity of mixing matrix or different NSIs effect in the source and detector results in absolute term lower than one which is effectively observed as absolute antineutrino flux lower than

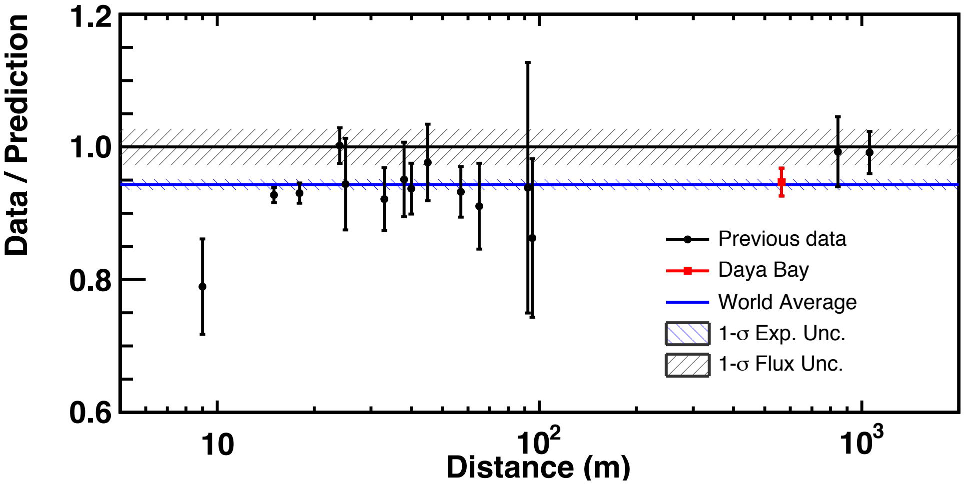

Figure 7.15: The measured of reactor antineutrino flux as a function of distance corrected for the three flavour oscillations and normalized to the theoretical prediction of Huber+Mueller model [89], [90]. Blue line corresponds to global average with marked 1σ uncertainty. Black line is the model prediction with 2.4% uncertainty. The red point is the Daya Bay measurement from the two near halls with wighted distance of 573 m [96].

prediction.

In order to set the constraints on NSIs parameters responsible for the effect compatible with "Reactor Anomaly" we would have to use constraints on flux predictions. Unfortunately, the LBNL fitter we used for analysis cannot easily accommodate flux constraints, because prediction for the Far Hall measurement is based on the near halls measurement. However, other tools exist within Daya Bay, which were developed along with LBNL fitter to study the effect of neutrino oscillations. Some of them are more suitable for the analysis with constrained flux [36]. These tools have based its prediction for all halls on the expected flux from the rectors obtained by the models. That provides ideal instrument to include flux constraints into the fitting procedure. We can expect that their use would point to the existence of NSIs due to the existence of "Reactor Anomaly". However, we should not rush into the conclusion that there are NSIs. First, we have to keep in mind that there are other explanations like existence of sterile neutrinos. Second, the solution might be even simpler.

The conservative explanation for the anomaly questions the accuracy of the predictions. Used models might not be sufficient in their description of the neutrino flux. This fact is backed up by recent measurement of the shape of the reactor antineutrino energy spectrum, which exhibits the excess over predicted shape in the energy region from 5 MeV to 7 MeV seen by several experiments including Daya Bay [95], [96]. Observation of the spectral distortion points to the model limitations, which, after revision, might lead to the disappearance of the anomaly. However, we have to note that observed bump in the measured spectrum itself cannot serve as an explanation for the "Reactor Anomaly".

Future measurements will determine the ultimate answer. Either it will be the search for sterile neutrino oscillations, improved measurement of inputs for the models for the flux prediction or search for new particles and their interactions resulting in NSIs effects.

8. Conclusions

Two scenarios of new physics in reactor electron antineutrino oscillations in short baselines in the Daya Bay experiment were investigated. We have tested the fundamental symmetry of Lorentz Invariance by the search for its violation (LIV) using the perturbative Standard-Model Extension (SME) and we have searched for the effects of Non-standard interactions (NSIs) using LBNL fitter, tool for relative near-far analysis developed by the team from Lawrence Berkeley National Laboratory. I have implemented the effects of LIV and NSI into the LBNL fitter for the analysis of the new physics parameters.

In the test of the Lorentz Invariance we have limited our study to the so-called Isotropic Lorentz Invariance violation where the effects are independent on the direction of antineutrino propagation. Such an effect would be observed in the oscillated energy spectrum in the far detector as a modification from the prediction of standard neutrino oscillations in three-neutrino framework.

We have investigated the significance of LIV signal and since we have not observed any significant deviation we used Gaussian $\mathrm{CL_S}$ to set exclusion limits on the SME parameters using case-by-case approach where only one or two Lorentz Invariance violation parameters are non-zero. Some of these limits are reported for the first time while we were not able to improve those already reported by the Super-Kamiokande experiment.

Complementary, we have investigated the effect of LIV with all possible SME parameters to be non-zero. In order to do that I have derived, based on mild assumptions, the survival probability formula containing such LIV effects for the Daya Bay experiment. This formula contains effective LIV parameters, which are linear combination of actual SME parameters. Again, we have not observed any significant deviation from Lorentz Invariance conservation therefore we set particular exclusion limits on full formula effective parameters.

I have performed parallel independent analysis of the LIV effects along with my Daya Bay colleague Nicolás Viaux.

Second, we searched for the effects of Non-standard interactions. Such interactions are highly suppressed or even forbidden in Standard Model, however, they can be result of more general theory for which Standard model is low energy limit. We consider Non-standard interactions only in the process of production and detection of neutrinos since their presence during the propagation is negligible for typical reactor antineutrino energies and distances at Daya Bay.

I have previously take part on the investigation of the potential of the Daya Bay experiment to constrain the NSIs parameters [64]. After joining the Daya Bay, I became the leading analyzer of the NSIs effect within the collaboration.

For this study, I have developed original phenomenological approach to introduce the effects of NSIs to the survival probability measured in Daya Bay. I consider this approach to be more suitable than the one commonly used, however, it makes hard to directly compare previous limits obtained with commonly used approach.

Wilks' Confidence Intervals method was used for the oscillation and NSIs parameter estimations. We have demonstrated that relative near-far measurement performed by Daya Bay can set constrains only to particular set of the parameters, i.e. standard parameter Δm^2_{ee} and pure NSIs parameter $\Delta\phi$. We have performed two analyses.

For the first one we kept both of these parameters unconstrained. We have found that there is a strong correlation between them, moreover, there is a more than 2σ deviation in $\Delta\phi$ from the standard oscillation prediction with the best fit value for Δm^2_{ee} quite off from the measurement of Daya Bay and other experiments analyzed in three-neutrino framework.

Since the values of Δm^2_{32} are consistent among each other we have decided in our second analysis to constrain Δm^2_{ee} using the measurements of various neutrino experiments. In this case, we have not observed any significant deviation from standard oscillations. We consider deviation in the first analysis to be more of statistical fluctuation than real signal of Non-standard Interactions.

We conclude that no evidence of NSIs was found in the Daya Bay data. We have set limits on NSIs parameter $\Delta\phi$. Its value is consistent with zero, i.e. data can be successfully interpreted with standard three-neutrino oscillations.

Bibliography

[1] C. L. Cowan, F. Reines, F. B. Harrison, H. W. Kruse, and A. D. McGuire. Detection of the free neutrino: a confirmation. *Science*, 124(3212):103–104, 1956.

[2] Bruce T. Cleveland, Timothy Daily, Jr. Raymond Davis, James R. Distel, Kenneth Lande, C. K. Lee, Paul S. Wildenhain, and Jack Ullman. Measurement of the solar electron neutrino flux with the homestake chlorine detector. *The Astrophysical Journal*, 496(1):505, 1998.

[3] Douglas Clowe, Marusa Bradac, Anthony H. Gonzalez, Maxim Markevitch, Scott W. Randall, Christine Jones, and Dennis Zaritsky. A direct empirical proof of the existence of dark matter. *Astrophys. J.*, 648:L109–L113, 2006.

[4] B. Pontecorvo. Mesonium and anti-mesonium. *Sov. Phys. JETP*, 6:429, 1957. [Zh. Eksp. Teor. Fiz.33,549(1957)].

[5] Ziro Maki, Masami Nakagawa, and Shoichi Sakata. Remarks on the unified model of elementary particles. *Progress of Theoretical Physics*, 28(5):870–880, 1962.

[6] Y. et al. Fukuda. Evidence for oscillation of atmospheric neutrinos. *Phys. Rev. Lett.*, 81:1562–1567, Aug 1998.

[7] Q. R. et al. Ahmad. Measurement of the rate of $\nu_e + d \to p + p + e^-$ interactions produced by ^8b solar neutrinos at the sudbury neutrino observatory. *Phys. Rev. Lett.*, 87:071301, Jul 2001.

[8] Nobel Media AB 2014. Web. 14 Jun 2016. Nobelprize.org. The 2015 nobel prize in physics - press release. www.nobelprize.org/nobel_prizes/physics/laureates/2015/press.html.

[9] F. P. An et al. Observation of electron-antineutrino disappearance at Daya Bay. *Phys. Rev. Lett.*, 108:171803, 2012.

[10] J. K. Ahn, S. Chebotaryov, J. H. Choi, S. Choi, W. Choi, Y. Choi, H. I. Jang, J. S. Jang, E. J. Jeon, I. S. Jeong, K. K. Joo, B. R. Kim, B. C. Kim, H. S. Kim, J. Y. Kim, S. B. Kim, S. H. Kim, S. Y. Kim, W. Kim, Y. D. Kim, J. Lee, J. K. Lee, I. T. Lim, K. J. Ma, M. Y. Pac, I. G. Park, J. S. Park, K. S. Park, J. W. Shin, K. Siyeon, B. S. Yang, I. S. Yeo, S. H. Yi, and I. Yu. Observation of reactor electron antineutrinos disappearance in the reno experiment. *Phys. Rev. Lett.*, 108:191802, May 2012.

[11] K. et al. Abe. Observation of electron neutrino appearance in a muon neutrino beam. *Phys. Rev. Lett.*, 112:061802, Feb 2014.

[12] Masaki Ishitsuka on behalf of Double CHOOZ collaboration. New results of double chooz, the 51st rencontres de moriond ew 2016. indico.in2p3.fr/event/12279/.

[13] L. Mikaelyan and V. Sinev. Searches for sterile neutrinos at reactor. *Phys. Atom. Nucl.*, 62:2008–2012, 1999. [Yad. Fiz.62,2177(1999)].

[14] E. Fermi. Versuch einer theorie der β-strahlen. i. *Zeitschrift für Physik*, 88(3):161–177, 1934.

[15] H. Bethe and R. Peierls. The 'neutrino'. *Nature*, 133:532, 1934.

[16] G. Danby, J-M. Gaillard, K. Goulianos, L. M. Lederman, N. Mistry, M. Schwartz, and J. Steinberger. Observation of high-energy neutrino reactions and the existence of two kinds of neutrinos. *Phys. Rev. Lett.*, 9:36–44, Jul 1962.

[17] K. Kodama et al. Observation of tau neutrino interactions. *Physics Letters B*, 504(3):218 – 224, 2001.

[18] S. Schael et al. Precision electroweak measurements on the Z resonance. *Phys. Rept.*, 427:257–454, 2006.

[19] John N. Bahcall. Solar neutrinos. i. theoretical. *Phys. Rev. Lett.*, 12:300–302, Mar 1964.

[20] S. P. Mikheyev and A. Yu. Smirnov. Resonant amplification of ν oscillations in matter and solar-neutrino spectroscopy. *Il Nuovo Cimento C*, 9(1):17–26, 1986.

[21] L. Wolfenstein. Neutrino oscillations in matter. *Phys. Rev. D*, 17:2369–2374, May 1978.

[22] J. N. et al. Abdurashitov. Measurement of the solar neutrino capture rate with gallium metal. iii. results for the 2002˘2007 data-taking period. *Phys. Rev. C*, 80:015807, Jul 2009.

[23] W. Hampel et al. {GALLEX} solar neutrino observations: results for {GALLEX} {IV}. *Physics Letters B*, 447(1-2):127 – 133, 1999.

[24] Y. Ashie et al. Evidence for an oscillatory signature in atmospheric neutrino oscillation. *Phys. Rev. Lett.*, 93:101801, 2004.

[25] K. et al. Abe. Precise measurement of the neutrino mixing parameter θ_{23} from muon neutrino disappearance in an off-axis beam. *Phys. Rev. Lett.*, 112:181801, May 2014.

[26] Hirohisa Tanaka on behalf of T2K collaboration. Status, recent results and plans for T2K, NEUTRINO2016. http://neutrino2016.iopconfs.org/programme.

[27] Patricia Vahle on behalf of NOvA collaboration. New results from NOvA, NEUTRINO2016. http://neutrino2016.iopconfs.org/programme.

[28] M. Fukugita and T. Yanagida. Barygenesis without grand unification. *Physics Letters B*, 174(1):45 – 47, 1986.

[29] M. Apollonio et al. Search for neutrino oscillations on a long baseline at the CHOOZ nuclear power station. *Eur. Phys. J.*, C27:331–374, 2003.

[30] B. Achkar et al. Comparison of anti-neutrino reactor spectrum models with the bugey 3 measurements. *Physics Letters B*, 374(1):243 – 248, 1996.

[31] Zelimir Djurcic et al. JUNO Conceptual Design Report. 2015.

[32] R. Acciarri et al. Long-Baseline Neutrino Facility (LBNF) and Deep Underground Neutrino Experiment (DUNE). 2015.

[33] K. Abe et al. Letter of Intent: The Hyper-Kamiokande Experiment — Detector Design and Physics Potential —. 2011.

[34] K. et al. Abe. Indication of electron neutrino appearance from an accelerator-produced off-axis muon neutrino beam. *Phys. Rev. Lett.*, 107:041801, Jul 2011.

[35] Y. Abe et al. Indication for the disappearance of reactor electron antineutrinos in the Double Chooz experiment. *Phys. Rev. Lett.*, 108:131801, 2012.

[36] Daya Bay collaboration. Measurement of electron antineutrino oscillation based on 1230 days of operation of the daya bay experiment. *to be on arxiv soon*, 2016.

[37] M. C. Gonzalez-Garcia, Michele Maltoni, Jordi Salvado, and Thomas Schwetz. Global fit to three neutrino mixing: critical look at present precision. *JHEP*, 12:123, 2012.

[38] Fengpeng An et al. Neutrino Physics with JUNO. *J. Phys.*, G43(3):030401, 2016.

[39] J. Angrik et al. KATRIN design report 2004. 2005.

[40] V. Alan Kostelecký and Stuart Samuel. Spontaneous breaking of lorentz symmetry in string theory. *Phys. Rev. D*, 39:683–685, Jan 1989.

[41] Don Colladay and V. Alan Kostelecký. CPT violation and the standard model. *Phys. Rev. D*, 55:6760–6774, Jun 1997.

[42] D. Colladay and V. Alan Kostelecký. Lorentz-violating extension of the standard model. *Phys. Rev. D*, 58:116002, Oct 1998.

[43] V. Alan Kostelecký. Gravity, lorentz violation, and the standard model. *Phys. Rev. D*, 69:105009, May 2004.

[44] V. Alan Kostelecký and Neil Russell. Data tables for lorentz and *cpt* violation. *Rev. Mod. Phys.*, 83:11–31, Mar 2011.

[45] V. Alan Kostelecký and Matthew Mewes. Lorentz and *CPT* violation in neutrinos. *Phys. Rev. D*, 69:016005, Jan 2004.

[46] Jorge S. Diaz. Neutrinos as probes of Lorentz invariance. *Adv. High Energy Phys.*, 2014:962410, 2014.

[47] Y. et al. Abe. First test of lorentz violation with a reactor-based antineutrino experiment. *Phys. Rev. D*, 86:112009, Dec 2012.

[48] J. S. Díaz, T. Katori, J. Spitz, and J. M. Conrad. Search for neutrino-antineutrino oscillations with a reactor experiment. *Phys. Lett.*, B727:412–416, 2013.

[49] R. et al. Abbasi. Search for a lorentz-violating sidereal signal with atmospheric neutrinos in icecube. *Phys. Rev. D*, 82:112003, Dec 2010.

[50] L. B. Auerbach et al. Tests of Lorentz violation in anti-nu(mu) —¿ anti-nu(e) oscillations. *Phys. Rev.*, D72:076004, 2005.

[51] A. A. Aguilar-Arevalo et al. Test of Lorentz and CPT violation with Short Baseline Neutrino Oscillation Excesses. *Phys. Lett.*, B718:1303–1308, 2013.

[52] Teppei Katori. Tests of Lorentz and CPT violation with MiniBooNE neutrino oscillation excesses. *Mod. Phys. Lett.*, A27:1230024, 2012.

[53] P. et al. Adamson. Testing lorentz invariance and cpt conservation with numi neutrinos in the minos near detector. *Phys. Rev. Lett.*, 101:151601, Oct 2008.

[54] P. et al. Adamson. Search for lorentz invariance and *cpt* violation with the minos far detector. *Phys. Rev. Lett.*, 105:151601, Oct 2010.

[55] P. et al. Adamson. Search for lorentz invariance and *cpt* violation with muon antineutrinos in the minos near detector. *Phys. Rev. D*, 85:031101, Feb 2012.

[56] B. Rebel and S. Mufson. The Search for Neutrino-Antineutrino Mixing Resulting from Lorentz Invariance Violation using neutrino interactions in MINOS. *Astropart. Phys.*, 48:78–81, 2013.

[57] K. et al.. Abe. Test of lorentz invariance with atmospheric neutrinos. *Phys. Rev. D*, 91:052003, Mar 2015.

[58] Jorge S. Diaz, V. Alan Kostelecky, and Matthew Mewes. Perturbative Lorentz and CPT violation for neutrino and antineutrino oscillations. *Phys. Rev.*, D80:076007, 2009.

[59] F. P. An et al. New Measurement of Antineutrino Oscillation with the Full Detector Configuration at Daya Bay. *Phys. Rev. Lett.*, 115(11):111802, 2015.

[60] Carla Biggio, Mattias Blennow, and Enrique Fernandez-Martinez. General bounds on non-standard neutrino interactions. *JHEP*, 08:090, 2009.

[61] Patrick Huber, T. Schwetz, and J. W. F. Valle. Confusing nonstandard neutrino interactions with oscillations at a neutrino factory. *Phys. Rev.*, D66:013006, 2002.

[62] Joachim Kopp, Manfred Lindner, Toshihiko Ota, and Joe Sato. Non-standard neutrino interactions in reactor and superbeam experiments. *Phys. Rev.*, D77:013007, 2008.

[63] Tommy Ohlsson and He Zhang. Non-Standard Interaction Effects at Reactor Neutrino Experiments. *Phys. Lett.*, B671:99–104, 2009.

[64] Rupert Leitner, Michal Malinsky, Bedrich Roskovec, and He Zhang. Non-standard antineutrino interactions at Daya Bay. *JHEP*, 12:001, 2011.

[65] Feng Peng An et al. Improved Measurement of the Reactor Antineutrino Flux and Spectrum at Daya Bay. 2016.

[66] International Atomic Energy Agency. Neutron thermal cross sections. https://www-nds.iaea.org/relnsd/NdsEnsdf/neutroncs.html.

[67] F. P. An et al. The Detector System of The Daya Bay Reactor Neutrino Experiment. *Nucl. Instrum. Meth.*, A811:133–161, 2016.

[68] F. P. An et al. The muon system of the Daya Bay Reactor antineutrino experiment. *Nucl. Instrum. Meth.*, A773:8–20, 2015.

[69] BNL National Nuclear Data Center. Chart of nuclides. http://www.nndc.bnl.gov/.

[70] J. Pedro Ochoa Yasuhiro Nakajima and Patrick Tsang. A measurement of $\sin^2(2\theta_{13})$ and δm^2 at daya bay using rate and shape information. Daya Bay collaboration internal note.

[71] Patrick Tsang Yasuhiro Nakajima, J. Pedro Ochoa and Henoch Wong. Lbnl oscillation analysis on p14a technote. Daya Bay collaboration internal note.

[72] X. Qian, A. Tan, J. J. Ling, Y. Nakajima, and C. Zhang. The Gaussian CL_s method for searches of new physics. *Nucl. Instrum. Meth.*, A827:63–78, 2016.

[73] S. S. Wilks. The large-sample distribution of the likelihood ratio for testing composite hypotheses. *Ann. Math. Statist.*, 9(1):60–62, 03 1938.

[74] Gary J. Feldman and Robert D. Cousins. A Unified approach to the classical statistical analysis of small signals. *Phys. Rev.*, D57:3873–3889, 1998.

[75] A L Read. Modified frequentist analysis of search results (the CL_s method). (CERN-OPEN-2000-205), 2000.

[76] A L Read. Presentation of search results: the cl s technique. *Journal of Physics G: Nuclear and Particle Physics*, 28(10):2693, 2002.

[77] F. P. An et al. Search for a Light Sterile Neutrino at Daya Bay. *Phys. Rev. Lett.*, 113:141802, 2014.

[78] Feng Peng An et al. Improved Search for a Light Sterile Neutrino with the Full Configuration of the Daya Bay Experiment. 2016.

[79] Louis Lyons. Open statistical issues in particle physics. *Ann. Appl. Stat.*, 2(3):887–915, 09 2008.

[80] Glen Cowan, Kyle Cranmer, Eilam Gross, and Ofer Vitells. Asymptotic formulae for likelihood-based tests of new physics. *Eur. Phys. J.*, C71:1554, 2011. [Erratum: Eur. Phys. J.C73,2501(2013)].

[81] J. et al. Beringer. Review of particle physics*. *Phys. Rev. D*, 86:010001, Jul 2012.

[82] P. Adamson et al. Combined analysis of ν_μ disappearance and $\nu_\mu \to \nu_e$ appearance in MINOS using accelerator and atmospheric neutrinos. *Phys. Rev. Lett.*, 112:191801, 2014.

[83] K. Abe et al. Measurements of neutrino oscillation in appearance and disappearance channels by the T2K experiment with 6.6×10^{20} protons on target. *Phys. Rev.*, D91(7):072010, 2015.

[84] K.A. Olive and Particle Data Group. Review of particle physics. *Chinese Physics C*, 38(9):090001, 2014.

[85] J. H. Choi et al. Observation of Energy and Baseline Dependent Reactor Antineutrino Disappearance in the RENO Experiment. *Phys. Rev. Lett.*, 116(21):211801, 2016.

[86] P. Adamson et al. First measurement of electron neutrino appearance in NOvA. *Phys. Rev. Lett.*, 116(15):151806, 2016.

[87] Roger Wendell. Atmospheric Results from Super-Kamiokande. *AIP Conf. Proc.*, 1666:100001, 2015.

[88] M. G. Aartsen et al. Determining neutrino oscillation parameters from atmospheric muon neutrino disappearance with three years of IceCube DeepCore data. *Phys. Rev.*, D91(7):072004, 2015.

[89] Patrick Huber. Determination of antineutrino spectra from nuclear reactors. *Phys. Rev. C*, 84:024617, Aug 2011.

[90] Th. A. Mueller, D. Lhuillier, M. Fallot, A. Letourneau, S. Cormon, M. Fechner, L. Giot, T. Lasserre, J. Martino, G. Mention, A. Porta, and F. Yermia. Improved predictions of reactor antineutrino spectra. *Phys. Rev. C*, 83:054615, May 2011.

[91] P. Vogel, G. K. Schenter, F. M. Mann, and R. E. Schenter. Reactor antineutrino spectra and their application to antineutrino-induced reactions. ii. *Phys. Rev. C*, 24:1543–1553, Oct 1981.

[92] K. Schreckenbach, G. Colvin, W. Gelletly, and F. Von Feilitzsch. Determination of the antineutrino spectrum from 235u thermal neutron fission products up to 9.5 mev. *Physics Letters B*, 160(4):325 – 330, 1985.

[93] A.A. Hahn, K. Schreckenbach, W. Gelletly, F. von Feilitzsch, G. Colvin, and B. Krusche. Antineutrino spectra from 241pu and 239pu thermal neutron fission products. *Physics Letters B*, 218(3):365 – 368, 1989.

[94] F. von Feilitzsch, A.A. Hahn, and K. Schreckenbach. Experimental beta-spectra from 239pu and 235u thermal neutron fission products and their correlated antineutrino spectra. *Physics Letters B*, 118(1):162 – 166, 1982.

[95] Feng Peng An et al. Measurement of the Reactor Antineutrino Flux and Spectrum at Daya Bay. *Phys. Rev. Lett.*, 116(6):061801, 2016.

[96] Feng Peng An et al. Improved Measurement of the Reactor Antineutrino Flux and Spectrum at Daya Bay. 2016.

List of Figures

2.1 Illustration of the normal and inverted mass hierarchies. 20

3.1 Antineutrino survival probability with respect to antineutrino energy for different cases. 31

5.1 Oscillation probability $P(\bar{\nu}_e \to \bar{\nu}_e)$ as a function of distance for typical reactor antineutrino energy $E_\nu = 3.5$ MeV. 44
5.2 Layout of the Daya Bay experiment. 45
5.3 Inverse beta decay cross-section, nuclear reactor antineutrino energy spectrum in arbitrary units and resulting detected unoscillated antineutrino energy spectrum in arbitrary units. 48
5.4 The section of the Antineutrino Detectors. 49
5.5 The scheme of Daya Bay muon tagging system, near hall as an example. 51
5.6 (Upper panel) The basic section through one RPC detector layer [68]. There are two bakelite plates separated with the layer filled with ionizable gas. The uniform space is ensured by spacers. There are graphite electrodes and copper read-out strips separated by plastic film. (Lower panel) The RPC readout pattern showing for illustration four of eight readout strips [68]. There is a zoom to the single readout strip showing its additional structure. The readout contacts are marked. The separation between readout strips is 0.25 cm. The folds of a single readout strip are 6.25 cm wide and separated by again 0.25 cm. 53
5.7 The distribution of prompt and delayed signal energy within time window $(1, 200)$ μs after multiplicity cut and muon veto. 55

6.1 The scheme of steps leading from the near site measurement to the far site prediction. 65
6.2 The final correlation matrix coefficients $(V_{ij}/\sqrt{V_{ii}V_{jj}})$. 69
6.3 The sketch of the Gaussian CL$_\mathrm{S}$ method. 72

7.1 Upper panel: The oscillation probability formulae with both Δm^2_{31}, Δm^2_{32} in Eq.(5.2) and the oscillation probability with single mass squared difference Δm^2_{ee} in Eq.(7.1) as a function of distance for typical reactor antineutrino energy $E_\nu = 3.5$ MeV. Lower panel: The ratio of $P(\Delta m^2_{ee})/P(\Delta m^2_{31}, \Delta m^2_{32})$. 76
7.2 The Δm^2_ϕ as a function of energy for distance L=1.8 km. The parameter is almost constant with value $\Delta m^2_\phi \simeq 5.17 \times 10^{-5}$ eV^2. 77
7.3 The ratio of far data over weighted average of near data 79
7.4 The $\Delta\chi^2_{ee}$ distribution obtained from 1000 toyMCs with statistical and systematical fluctuations for the case of Lorentz Invariance conservation 81
7.5 Exclusion contours at 95% CL$_\mathrm{S}$ level for parameters $\mathrm{Re}(a_L)^T_{\alpha\beta}$, $\mathrm{Re}(c_L)^{TT}_{\alpha\beta}$ for $e\mu$ (blue) and $e\tau$ (red) cases. The excluded region is outside closed contours. 82

7.6 Top: Exclusion contours at 95% $\mathrm{CL_S}$ level for $(a_L)^T_{\alpha\beta}$, $(c_L)^{TT}_{\alpha\beta}$ for ee, $\mu\mu$ and $\tau\tau$ cases. The excluded region for ee (blue), $\mu\mu$ (green) cases are outside the u-shaped unclosed contours while for $\tau\tau$ (red) case the excluded region is below the line. Bottom: Exclusion contours at 95% $\mathrm{CL_S}$ level for $(a_L)^T_{\alpha\beta}$, $(c_L)^{TT}_{\alpha\beta}$ for $\mu\tau$ case. The excluded region is outside the u-shaped unclosed contours. 83

7.7 The $\sin^2 2\theta^{BF}_{13}$ as a function of SME parameters $(a_L)^T_{ee}$, $(c_L)^{TT}_{ee}$ for the ee case overlaid by the exclusion contours 85

7.8 The $\mathrm{CL_S}$ profiles (solid black) as well as $\sin^2 2\theta^{BF}_{13}$ (dashed blue) for four LIV parameters X_i (i=1,2,3,4) from full formula in Eq.(3.32). 88

7.9 Comparison of 95% $\mathrm{CL_S}$ exclusion contours for normal and inverted hierarchy for ee case. 90

7.10 The 95% confidence level contours for Δm^2_{ee} and $\Delta\phi$ and the best-fit point $\Delta m^2_{ee} = 3.25 \times 10^{-3}$ eV^2 and $\Delta\phi = 0.9$. 93

7.11 Left: The $\Delta\chi^2_{\Delta m^2}(\Delta m^2_{ee})$ profile with the indication of 95% CL limit (red dashed line). Right: The $\Delta\chi^2_{\Delta\phi}(\Delta\phi)$ profile with the indication of 95% CL limit (red dashed line). 94

7.12 The comparison of the measurements of $|\Delta m^2_{32}|$ performed by various experiments. 95

7.13 The $\Delta\chi^2_{\Delta m^2 fix}$ profile as a function of $\Delta\phi$. 96

7.14 Left: The $\Delta\chi^2_a$ profiles as a function of $\Delta\phi$ for different values of parameter a. Right: The $\Delta\chi^2_b$ profiles as a function of $\Delta\phi$ for different values of parameter b. In both cases, the resulting limits for $\Delta\phi$ are basically independent on the choice of a or b and the curves for different choices of those parameters lie on the top of each other. 97

7.15 The measured of reactor antineutrino flux as a function of distance corrected for the three flavour oscillations and normalized to the theoretical prediction of Huber+Mueller model [89], [90]. 99

List of Tables

2.1 Global best fit of neutrino flavour oscillation parameters. 20
2.2 Parameters which can JUNO improve and their expected relative uncertainty after 6 years of running. 21

5.1 Overburden of three Daya Bay underground experimental halls in meters and in meters of water equivalent [36]. 45
5.2 Distances in meters between reactor cores. 46
5.3 List od sources mounted in each Automated Calibration Unit and corresponding released energy. 50
5.4 The number of 8" PMTs instrumented in IWS and OWS in the three experimental halls. 52
5.5 Inverse Beta Decay Candidate Selection Cuts (Selection A in [36]). 54
5.6 Efficiencies for the IBD selection with neutron capture on gadolinium and their correlated and uncorrelated uncertainties among ADs. 56
5.7 Summary of the signal and backgrounds for 621 days of Daya Bay data. 61

7.1 The significance of LIV signal for case-by-case formulae 80
7.2 Minimum and maximum values of the 61×61 grid in $(a_L)^T_{\alpha\beta}$-$(c_L)^{TT}_{\alpha\beta}$ parameter space used in the scan to obtain $\mathrm{CL_S}$ exclusion contours. 82
7.3 Summary of upper and lower limits on 95% CL_S for SME parameters obtained by case-by-case formulae for flavour combinations $e\mu$ and $e\tau$ with two non-zero SME parameters $\mathrm{Re}(a_L)^T_{\alpha\beta}$, $\mathrm{Re}(c_L)^{TT}_{\alpha\beta}$. Normal neutrino mass hierarchy is assumed to be true. 86
7.4 Summary of upper and lower exclusion limits on 95% $\mathrm{CL_S}$ for SME parameters obtained by using reduced case-by-case formulae when only one SME parameter is considered to be non-zero at the time. Normal neutrino mass hierarchy is assumed to be true. 87
7.5 Summary of upper or lower exclusion limits on 95% CLs for LIV parameters X_i's assuming normal neutrino mass hierarchy. 89
7.6 Summary of upper and lower exclusion limits on 95% $\mathrm{CL_S}$ for SME parameters obtained by using reduced case-by-case formulae when only one SME parameter is considered to be non-zero at the time. This time, inverted neutrino mass hierarchy is assumed to be true. 91
7.7 The summary of the allowed values as well as the best fit for NSIs parameter $\Delta\phi$. 98

List of Abbreviations

ACU Automated Calibration Unit

AD Antineutrino Detector

BF Best Fit

BR Branching Ratio

BSM Beyond Standard Model

CERN European Organization for Nuclear Research

CI Confidence Intervals

CP Charge Parity

CPT Charge Parity Time

DAQ Data Aquisition

DoF Degrees of Freedom

DONUT Direct Observation of the NU Tau

DUNE Deep Underground Neutrino Experiment

GdLS Gadolinium-dopped Liquid Scintillator

IAV Inner Acrylic Vessel

IBD Inverse Beta Decay

IH Inverted Hierarchy

IWS Inner Water System

KamLAND Kamioka Liquid Scintillator Antineutrino Detector

J-PARC Japan Proton Accelerator Research Complex

JUNO Jiangmen Underground Neutrino Observatory

KATRIN Karlsruhe Tritium Neutrino Experiment

LAB Linear AlkylBenzen

LBNL Lawrence Berkeley National Laboratory

LED Light-emitting Diod

LEP Large Electron-Positron collider

LIV Lorentz Invariance Violation

LS Liquid Scintillator

LSND Liquid Scintillator Neutrino Detector

MC Monte Carlo

MiniBooNE Mini Booster Neutrino Experiment

MINOS Main Injector Neutrino Oscillation Search

N/A Not Available

NH Normal Hierarchy

NHIT Number of Hits

NOvA NuMI Off-Axis ?e Appearance

NSIs Non-standard Interactions

NuMI Neutrinos at Main Injector

OAV Outer Acrylic Vessel

OWS Outer Water System

PE Photoelectron

PMT Photomultiplier Tube

RENO Reactor Experiment for Neutrino Oscillations

RPC Resistive Plate Chamber

SAGE Soviet American Gallium Experiment

SK Super-Kamiokande Experiment

SM Standard Model

SME Standard-Model Extension

SNO Sudbury Neutrino Observatory

T2K Tokai to SK Long-Baseline Oscillation Experiment

toyMC Toy Monte Carlo

UV Ultraviolet